

4-2015

Analysis of a Hybrid Rocket Burn Using Generalized Compressible Flow

Naveen Sri Uddanti

Follow this and additional works at: <https://commons.erau.edu/edt>



Part of the [Aerospace Engineering Commons](#)

Scholarly Commons Citation

Uddanti, Naveen Sri, "Analysis of a Hybrid Rocket Burn Using Generalized Compressible Flow" (2015).
Dissertations and Theses. 285.

<https://commons.erau.edu/edt/285>

This Thesis - Open Access is brought to you for free and open access by Scholarly Commons. It has been accepted for inclusion in Dissertations and Theses by an authorized administrator of Scholarly Commons. For more information, please contact commons@erau.edu.

ANALYSIS OF A HYBRID ROCKET BURN USING GENERALIZED
COMPRESSIBLE FLOW

by

Naveen Sri Uddanti

A Thesis Submitted to the College of Engineering, Department of
Aerospace Engineering in Partial Fulfillment of the Requirements
for the Degree of Master of Science

Embry-Riddle Aeronautical University
Daytona Beach, Florida
April 2015

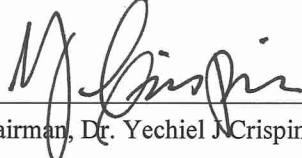
ANALYSIS OF A HYBRID ROCKET BURN USING
GENERALIZED COMPRESSIBLE FLOW


by

Naveen Sri Uddanti


A Thesis prepared under the direction of the candidate's committee chairman, Dr. Yechiel J Crispin, Department of Aerospace Engineering, and has been approved by the members of the thesis committee. It was submitted to the School of Graduate Studies and Research and was accepted in partial fulfillment of the requirements for the degree of Master of Science in Aerospace Engineering.


THESIS COMMITTEE



Chairman, Dr. Yechiel J Crispin

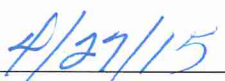

Member, Dr. Lakshman Narayanaswami



Member, Dr. Mahmut Reyhanoglu



Department Chair, Dr. Anastasios Lyrintzis
or Graduate Program Coordinator, Dr. Yi Zhao


Date


Dean of College of Engineering, Dr. Maj Mirmirani


Date


Associate VP for Academics, Dr. Robert Oxley


Date

Acknowledgements

I would like to express my deepest gratitude to my advisor, Dr. Yechiel J. Crispin, for his excellent guidance, patience and providing me with an excellent atmosphere for doing research. I place on record, my sincere thank you to Dr. Lakshman Narayanaswami, Professor of Combustion and Hypersonic Aerospace Propulsive flows, in the Department of Aerospace Engineering. I am extremely thankful and indebted to him for sharing expertise, sincere and valuable guidance extended to me. I am also grateful to Dr. Mahmut Reyhanoglu, Professor of Engineering Physics, in the Department of Physical Science for the continuous encouragement, assistance and suggestions throughout my research. To all my friends and family for helping me survive all the stress from this year and not letting me give up. I take this opportunity to express gratitude to all the department faculty members for their help and support. I also thank my parents for the unceasing encouragement, support and attention. I place on record, my sense of gratitude to one and all, who directly or indirectly, have lent their hand in this venture.

Abstract

Researcher: Naveen Sri Uddanti

Title: Analysis of a Hybrid Rocket Burn using Generalized Compressible Flow

Institution: Embry-Riddle Aeronautical University

Degree: Master of Science in Aerospace Engineering

Year: 2015

The analysis of square ports in a hybrid rocket is simple when compared to other complicated port geometries such as a wagon wheel configuration. In the present work, fuel grains with several ports in a hybrid rocket engine are analyzed by transforming the ports into equivalent square ports. As an example, the internal ballistics of a hybrid rocket with circular ports is analyzed by transforming it to an equivalent solid grain with square ports having the same amount of solid fuel and burn time. The results obtained are similar to that of circular port but with a slight decrease in oxidizer to fuel (O/F) ratio and decrease in web thickness. The volumetric efficiencies for different number of square ports are determined assuming a constant mass of solid fuel. The variation of the flow properties along the axial length of the port are calculated using a generalized one-dimensional compressible flow analysis. The combined effects of wall mass injection and heat addition are taken into account.

Table of contents

Acknowledgements	iii
Abstract.....	iv
Nomenclature	vii
List of Figures.....	xi
List of Tables	xii
Chapter I.....	1
Introduction.....	1
Characteristics of a Hybrid Rocket.....	5
Advantages of the Hybrid Rocket	5
Disadvantages of the Hybrid Rocket.....	8
Early Investigations	9
Background and Relevance of the Present Work	11
Chapter II	13
Hybrid-Motor Ballistics for Circular Ports.....	13
Introduction.....	13
The Regression Equation in Non-Dimensional Form.....	17
Numerical Results	22
Results & Discussion for single circular port solid grain	23
Validation of Results.....	25
Results & Discussion for four circular ports solid grain	31
Chapter III.....	37
Hybrid-Motor Ballistics for Square ports	37
Introduction.....	37

Volumetric Efficiency for square ports.....	37
Single Square Port	37
Four Square Ports.....	39
Nine Square Ports	40
Sixteen Square Ports.....	42
The Regression Equation in Non-Dimensional Form	44
Numerical Results	48
Results & Discussion for a Single Square Port.....	48
Results & Discussion for Four square ports.....	54
Results for Volumetric Efficiency of the Square ports.....	59
Chapter IV	60
Variation of the Flow Properties along the Axial Direction.....	60
Introduction.....	60
Modeling of Generalized One-Dimensional Flow	60
Working Equations and Tables of Influence Coefficients.....	66
Numerical Setup for $D = 0.152$ m	72
Results & Discussion for $D = 0.152$ m	73
Numerical Setup for $D = 0.215$ m	78
Results & Discussion for $D = 0.215$ m	79
Numerical Setup for $D = 0.291$ m	84
Results & Discussion for $D = 0.291$ m	85
Conclusions.....	91
Future work.....	93
References.....	94

Nomenclature

a	= Regression rate constant
A_p	= Cross section area per port
A_{p0}	= Initial cross sectional area per port
A_{sf}	= Surface area of the solid fuel
A_t	= Throat area of the grain
b	= Initial side of the square port
B	= Side of the total fuel grain
c	= Sound velocity
C	= Circumference of the port
C^*	= Characteristic velocity
C_p	= Specific heat at constant pressure
D_0	= Initial Diameter of the circular port
D	= Diameter of the circular port
f	= Coefficient of friction
F	= Thrust produced
G	= Total propellant mass flux rate ($\text{kg}/\text{m}^2.\text{s}$)
G_f	= Fuel mass flux rate ($\text{kg}/\text{m}^2.\text{s}$)

G_{f0} = Initial fuel mass flux rate ($\text{kg}/\text{m}^2.\text{s}$)

G_o = Oxidizer mass flux rate per port ($\text{kg}/\text{m}^2.\text{s}$)

G_{o0} = Initial oxidizer mass flux rate per port ($\text{kg}/\text{m}^2.\text{s}$)

g_0 = Gravitational acceleration

H = Energy term

h_{gt} = Enthalpy of the injected gas at temperature T

h_g = Enthalpy of the injected gas at temperature T_g

I_{sp} = Specific impulse

L_p = Port length

M = Mac number

\dot{m}_{prop} = Total propellant mass flow rate

\dot{m}_o = Oxidizer mass flow rate

\dot{m}_f = Fuel mass flow rate

m_f = Mass of the solid fuel

m = Regression rate constant

MW = Molecular weight

n = Regression rate constant

N = Number of ports

OF = Oxidizer to fuel ratio (mass ratio)

$(OF)_0$ = Initial oxidizer to fuel ratio

P = Pressure of the flow

P_p = Port perimeter

P_{p0} = Initial port perimeter per port

P_c = Chamber pressure

P_{c0} = Initial chamber pressure

Q = Heat addition due to conduction or radiation

q = Integration factor

R = Gas constant

\dot{r} = Solid fuel regression rate (m/s or cm/s)

\dot{r}_0 = Initial solid fuel regression rate (m/s or cm/s)

T = Temperature of the flow

T_f = Flame temperature

V = Velocity of the flow

V_g = Velocity of the injected gas

V_{sf} = Volume of the solid fuel

V_e = Exit velocity

w = Web thickness at time t

w_f = Final web thickness

W_x = External work delivered

x = Axial distance along the port, measured from the port entrance (m)

β = Slenderness ratio

δ = Arbitrary constant

ε = Expansion ratio

ρ = Density of the flow

ρ_f = Solid fuel density (kg/m^3)

τ = Characteristic time

γ = Isentropic Parameter

List of Figures

Figure 1.1. Schematic of Hybrid Rocket

Figure 2.1. Schematic of cross-section of solid fuel grain

Figure 3.1. Schematic of cross-section of square solid fuel grain with single port

Figure 3.2. Schematic of cross-section of square solid fuel grain with four ports

Figure 3.3. Schematic of cross-section of square solid fuel grain with nine ports

Figure 3.4. Schematic of cross-section of square solid fuel grain with sixteen ports

Figure 4.1. Schematic of the combustion hybrid chamber

List of Tables

<i>Table. 2.1.</i>	Reference Values for the results from Altman for a single circular port
<i>Table. 2.2.</i>	Results obtained by the proposed procedure for a single circular port
<i>Table 2.3.</i>	Results obtained by the proposed procedure for 4 circular ports
<i>Table 3.1.</i>	Results obtained by the proposed procedure for a single square port
<i>Table 3.2.</i>	Results obtained by the proposed procedure for four square ports
<i>Table 4.1.</i>	Reference Values for the results from Altman at $D = 0.152$ m
<i>Table 4.2.</i>	Reference values for the results from Altman at $D = 0.215$ m
<i>Table 4.3.</i>	Reference Values for the results from Altman at $D = 0.291$ m

Chapter I

Introduction

A hybrid rocket stores propellant in two different states namely liquid and solid. Any propulsion system that is not entirely homogeneous can be known as hybrid, but the classical hybrid rocket is usually defined as motor using a solid fuel and a liquid oxidizer as shown in the Fig.1. However, it is possible to use reverse hybrids where the oxidizer is solid and the fuel is liquid. Unless we specify otherwise, our discussion in this report assumes the classical hybrid with a solid fuel grain. Because of this separation of oxidizer and fuel into two different states, combustion differs from that of either the solid or liquid rocket. In the case of solid propellant, a small element of volume in the combustor contains an essentially uniform mixture of oxidizer and fuel. However, the hybrid burns as a macroscopic diffusion flame [Altman, 1995], in which the oxidizer-to-fuel ratio (O/F) varies down the length of the fuel port.

The earliest work on hybrid rockets was conducted in the late 1930s at I. G. Farben in Germany and at the California Rocket Society in the United States [George, 1996]. In 1937, with O. Lutz and W. Noeggerath, he tested a 10-kN hybrid using coal and gaseous nitrous oxide [Humble, 1995]. In the early 1940s, the California Pacific Rocket Society conducted a more successful effort, which employed Lox and several fuels such as wood, wax, and finally rubber [Venugopal, 2011]. Of these combinations, the Lox-rubber combination was the most successful: a rocket using these propellants was flown in June 1951 to an altitude of about 9 km [Altman, 1995]. They found an accurate concept of the fundamentals of hybrid burning as evidenced by the following statement: “The chamber pressure of a solid-liquid rocket engine is proportional to the oxidizer flow

and not the internal surface area exposed to the flame. Thus, there is no danger of explosions due to cracks and fissures in the charge as with solid propellant rockets.”

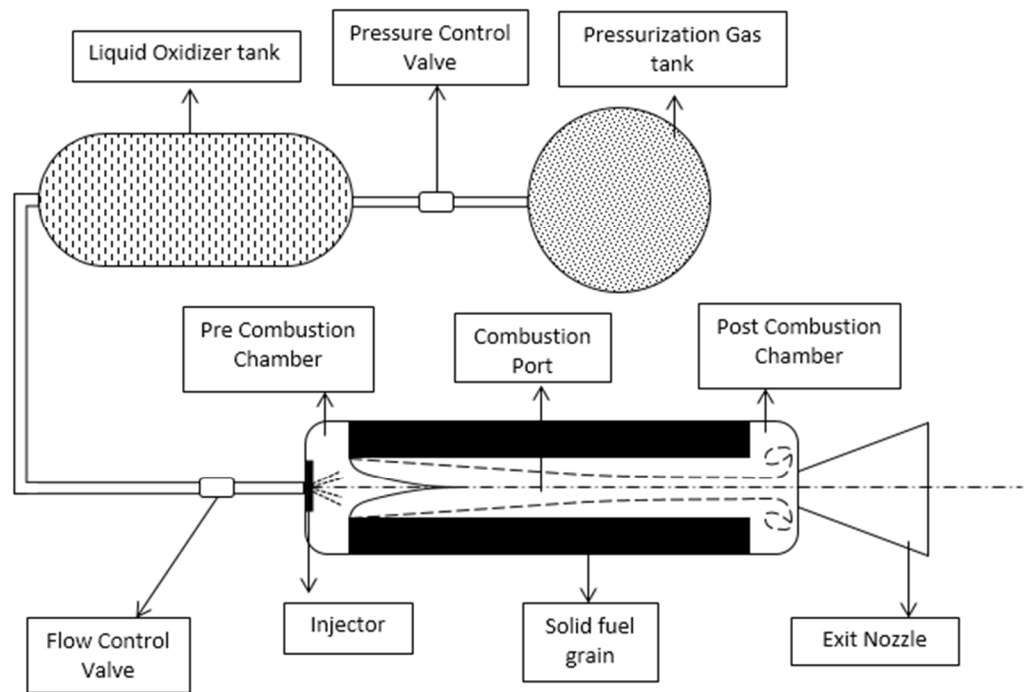


Figure 1.1. Schematic of Hybrid Rocket: This figure shows many of the components typically found in a hybrid rocket system

In 1952, William Avery and coworkers at the Applied Physics Laboratory of John Hopkins University conducted burning tests with a reverse hybrid rocket propellant system [Ordahl, 1964]. The propellants tested were benzene and jet propellant (JP) fuel, with potassium perchlorate, ammonium nitrate and ammonium perchlorate as oxidizers. They concentrated on JP ammonium nitrate because it represented perhaps the lowest cost propellants available, which was the primary motivation for the investigation. Unfortunately, this propellant combination was difficult to burn. The major problems

encountered in their work were rough burning and rather poor performance. Note that the liquid-to-solid ratio (F/O) of this propellant combination is in the range of 0.035, which is about 200 times smaller than that used by Moore and Berman.

Other versions of the reverse hybrid were studied by both Thiokol and United Technology Center (UTC) in the mid 1960's using hydrazine based liquid fuels and such solid oxidizers as ammonium perchlorate, hydrazinium di-perchlorate, and nitronium perchlorate [Altman, 2007]. These solid charges were pressed usually with a non-reactive fluorocarbon as a binder. Efforts were abandoned because of poor combustion behavior and insufficient performance improvement to justify the difficulties experienced in compressing the charges. The classical hybrid motor combustion model, developed by Marxman and Wooldridge [Marxman, 1963] and Gilbert and Marxman [Gilbert, 1963] in the early 1960s, is based on turbulent boundary layer transport mechanisms with a diffusion limited combustion process. The regression of the solid surface is sustained by the thermal energy feedback from the flame, resulting in a purely convective model. Those studies led to the generation of a family of regression rate laws in the form $\dot{r} = f(x)G_{Ox}^n$ with an exponent of about $n \approx 0.8$

A few years later, in the early 1970s, Price and Smoot [Price, 1965] began to theorize the possibility of a dependence between the solid fuel regression rate and the operating conditions of the chamber. Their analysis, resulting from intensive experimental studies, showed that the exponent, for the oxidizer mass flux G_{Ox} varied not only depending on the value of the same mass flow, but also with changes in the total chamber pressure [Humble, 1995]. Although their early studies showed an enhancement

of the regression rate with increasing pressure, the authors failed to find a satisfactory explanation for the results.

It was only after the 1990s that the inquiry of dependence on the operating conditions was resumed. Two research groups at the university of Delaware and Pennsylvania State University have separately conducted some important analysis. The first one led by Arisawa and Brill, studied in detail the pyrolysis of hydroxyl-terminated poly butadiene [Arisawa, 1996]. The products resulting from the fuel sublimation were analyzed in different conditions of pressure and heating rate of the polymer. The study shows that, below a certain temperature, the pyrolysis process is governed by decomposition of the solid matrix, whereas above it the evolution of the gas mixture is controlled by the rate of desorption of gaseous species.

One of the most significant hybrid development efforts in industry in the recent past is the development of propulsion system for Spaceship One, an X-prize entry built by Scaled Composites Inc16 [Macklin, 2003]. On June 21, 2004 Spaceship One successfully reached a suborbital altitude of 100 km using a nitrous oxide-fed HTPB-based hybrid rocket motor. The Tier one was the first privately developed reusable vehicle able to perform a manned suborbital flight over 100 km. The first stage of the Tier one is a twin turbojet carrier launch aircraft called the White Knight, which is able to bring the second stage to 15 km altitude. The second stage, the spaceship one, is a reusable three place manned space plane, powered by a N_2O /HTPB hybrid rocket engine. This HRE has a burning time of about 80 seconds and it is able to produce an average thrust of 75 KN with a vacuum specific impulse of about 250 s. The Tier One was retired

after winning the X-prize, but it remains proof that HREs may be the key propulsion system of the emerging space market.

Characteristics of a Hybrid Rocket

The hybrid rocket is formed by combining many of the advantages of both liquid and solid rockets. The controllability of a solid rocket and safety of a liquid rocket are merged together to create a hybrid rocket. It has flexibility regarding the type of fuel and the management and development costs are moderate because there is no huge investment in special facilities or personnel safeguards. Although hybrid rocket combustion and propulsion characteristics have been investigated for more than six decades, practical motor development and maturation has not been as actively pursued as that of liquid and solid rocket engines. The hybrid rocket is known to provide several distinct advantages over both solid propellant and liquid propellant motors. Throttling, simplicity, safety, low cost, propellant versatility, grain robustness, environmental friendliness, low temperature sensitivity, performance and handling are among the hybrid's most attractive features.

Advantages of the Hybrid Rocket

A hybrid rocket has several advantages over its solid and liquid counter parts. These hybrid rocket features are briefly summarized below.

Throttling: The most important advantage of hybrid rocket motors over the solid rockets is their ability to change thrust over a wider range. The engine can be throttled by simply modulating the oxidizer mass flow rate, whereas liquid rockets require two flow rates synchronized while being modulated. This throttling feature is useful for a broad range of

applications including sounding rocket, tactical missile, and launch vehicle propulsion and space engines.

Simplicity: The reliability and simplicity can be obtained over liquid rocket engines because feeding system hardware is reduced as only the oxidizer is liquid and therefore, can be less complex with higher reliability.

Safety: Hybrid rocket engines are inherently safe due to the use of a solid fuel grain which is classically inert. Since the fuel and oxidizer are separated by distance and phase, hybrids have almost no explosion hazard and very few failure modes. The hybrid fuels have a TNT equivalence of zero.

Low cost: Lower system cost results from greatly reduced failure modes, which permit the use of commercial-grade, instead of ingredients. The system can tolerate larger design margins, resulting in a lower fabrication cost. Because the fuel does not explode, storage and handling requirements are simpler. Low recurring costs are foreseen because of high levels of safety and minimal failure modes.

Propellant versatility: The hybrid's liquid oxidizer provides a higher energy level than any of the conventional solid oxidizers. But the hybrid's solid fuel permits the simple addition of many other ingredients, such as energetic metals, whereas a liquid system requires slurry mixtures.

Grain robustness: unlike solid rockets, fuel grain cracks are not catastrophic because burning occurs only in the port when it encounters the oxidizer flow. It has been conclusively verified that burning does not take place within cracks or between the grain and the combustion chamber wall of a hybrid motor.

Environmental friendliness: Compared to solid rocket motors, oxidizers are chlorine free. Compared to liquid rocket engines, storable propellants are available, which do not have noxious features such as mono methyl hydrazine and nitrogen tetroxide. The large range of available propellant ingredients permits the selection of many combinations which do not produce hydrochloric acid, aluminum oxide, or other undesirable chemicals in the exhaust.

Low temperature sensitivity: Because the temperature effect on burn rate is negligible (as in liquids), we need not apply a margin to the thrust chamber weight to account for the variation of maximum expected operating pressure (MEOP) with ambient temperature.

Performance: Hybrid rocket engines may deliver a higher specific impulse than solid rocket motors. Due to the high-density solid they also may have higher density specific impulse than liquid rocket engines. This latter benefit may be wasted by sliver or low grain volumetric efficiency.

Handling: We can shut down and restart the system. This feature is an important safety consideration because it allows for an abort procedure. In considering very large engines these can be subjected to harsh handling.

Apart from the above mentioned advantages, regenerative nozzle cooling and liquid injection thrust vector control are the other added advantages over pure solids. Another advantage of hybrid rocket over an all solid rockets is the very high mechanical properties of the solid fuel grain. The binder content of the propellant grain for solid system is usually kept to the lowest practical level whereas the binder level in hybrid

fuels is high, leading to much better mechanical properties. However, hybrid combustion studies are complicated by the interaction between the solid fuel regression rate and the aerodynamics of the chemically reacting boundary layer flow through the fuel grain.

Disadvantages of the Hybrid Rocket

Classical hybrids suffer from many deficiencies: starting from low regression rate, low bulk density, combustion efficiency, O/F shift, fuel residuals and slow transient/response to throttling.

Low regression rate: A small fuel web means that most combustion chambers over 30 cm in diameter require multiple ports. The regression rate of conventional binders such as HTPB (Hydroxyl Terminated Poly Butadiene) is typically an order of magnitude lower than solid propellants and hence a large fuel surface area is needed to produce the required thrust level. However, this characteristic may be an advantage for long duration applications such as target drones, hovering vehicles and gas generators.

Low bulk density: The volumetric fuel loading density in the combustion chamber is low because we must inject the total oxidizer at the head end and allow for a mixing volume aft of the grain. This results in a lower mass fraction than in liquids or solids, so the hybrid exhibits a larger envelope for a given mission.

Combustion efficiency: Part of the fuel under the flame at the grain port exit may not mix with any oxidizer and thus exit the nozzle before releasing chemical energy. The nature of the large diffusion flame results in a lower degree of mixing and hence lower impulse efficiency. This loss is usually 1-2% more than in liquids or solids.

O/F shift: The cross-sectional area increase of the port during burning causes an O/F shift with burning time, which can lower theoretical performance. But proper design minimizes this loss.

Fuel residuals: Conventional hybrids with multiple ports cannot be burned to completion because portions of the fuel web between the ports would dislodge from the host grain and potentially block the nozzle. Therefore, a few percent of the fuel must be left intact at the end of the mission. These so called fuel slivers subtract from the overall propulsion system mass fraction.

Slow transient/response to throttling: Due to the thermal lag in the solid fuel, ignition and response to throttling is slow in comparison to liquid rocket engines. Also, the chamber volume may be larger than in liquid rockets with large tail-off volume.

Apart from the innate reluctance of introducing a new system, certain disadvantages led to non-operationalizing the hybrids in big way. They have lower density specific impulse and thus a larger system volume than solids and leave large slivers. Another serious problem that cropped up during the development phase of hybrid rocket motors was the pressure oscillations that can appear under certain conditions. Although these are not unstable, these have reached in some cases double the motor operating pressure.

Early Investigations

Early investigations into hybrid solid fuel regression rate behavior were conducted by Bartel and Rannie [Bartel, 1946], Emmons [Emmons, 1953], Majdalani [Majdalani, 2007]. Bartel and Rannie considered the one-dimensional axial flow of air

through a tube of carbon. The turbulent airstream entered the tube of diameter D with assumed known inlet velocity, density, pressure and total temperature. Bartel and Rannie theorized that the diffusion of oxygen to the fuel surface controlled the fuel regression process [Bartel, 1946].

Emmons also obtained a solution for the boundary layer combustion of a gaseous oxidizer flowing over a fuel surface, although he did not necessarily have in mind hybrid rocket propulsion as an application of the problem [Emmons, 1953]. Emmons assumed a laminar flame zone of finite thickness in the boundary layer and then transformed the energy, momentum and species equations into Blasius-type equations by assuming unity Prandtl, Lewis and Schmidt numbers.

Majdalani considered non-reactive outer flow, prompted by the weak reactions that accompany diffusion flames [Majdalani, 2007]. The basic flow was assumed to be steady, inviscid, incompressible, rotational, axi-symmetric and non-swirling. The incompressible mean flow approximations were presented for axisymmetric and planar representations of a hybrid rocket chamber. Several quasi-viscous solutions were obtained that attempt to observe, the principal surface requirements including the orthonormal injection condition on both headwall and sidewall for the hybrid model. Their behavior was illustrated for the cases of small and large headwall injection in solid and hybrid rocket chambers. The analysis was further extended to account not only for uniform but also variable inlet patterns that can be potentially used to mimic more realistic systems. In the hybrid configuration, their models were seen to properly capture the fundamental stream tube motion.

Background and Relevance of the Present Work

The combustion process in the hybrid rocket is distinctly different from that in the liquid or solid motor. Designing Hybrid Rocket Propulsion Systems (HRPS) depends on the unique nature of hybrid combustion or internal ballistics. The solid fuel vaporizes, mixes with the liquid oxidizer and enters the port for combustion. Thus, the solid fuel burn rate is a function of oxidizer flow rate. By utilizing these studies any fuel grain can be easily transformed to a simple geometry and the internal ballistics for the fuel grain can be obtained by maintaining the volume of the fuel constant, thereby avoiding complicated analysis procedure.

In this thesis, we consider the regression rate equation and conduct analysis for different port geometries, i.e. circular port and square port and deduce the burn and flow properties for those port geometries. In the next two chapters, the change in flow properties along axial length is neglected. In the final chapter, the variations of the flow properties along the axial length are studied.

Initially a single circular port is considered and the internal ballistics of the combustion process is obtained following a non-dimensionalization procedure. This process yields a first order ODE (Ordinary Differential Equation) supplemented by a non-linear algebraic equation which is then solved to obtain the results and they are a good match with the reference values. Next the fuel grain is transformed into a four port geometry by considering the same mass of fuel and the same web thickness. By using a multiple port configuration for the same amount of fuel, the length of the fuel grain can be reduced and the internal ballistics for this model can be analyzed. The four port circular configuration is considered because it can be compared with four port square

configuration and the arrangement of four circular ports in a circular chamber is easy. The results obtained in both the cases are compared.

Later the single circular port is transformed into an equivalent single square port and the analysis is carried out on the square port followed by the comparison of the results. The reason behind choosing the square port is there was a minimum research conducted on the square port and geometrically square port is easy to analyze when compared to other complicated geometries like a wagon wheel configuration. This analysis procedure is extended up to sixteen square port configuration and the optimum value for the number of ports is reached for the same amount of mass based on the volumetric efficiency graph. The final chapter deals with the variation of flow properties along the axial length with head wall injection assuming compressible flow.

Chapter II

Hybrid-Motor Ballistics for Circular Ports

Introduction

This chapter deals with the internal ballistics of a single and four circular port grain configuration. Initially the analysis of a single circular port is carried out and then this fuel grain is transformed into a four port configuration by keeping the mass constant. The results are compared for both the cases. We start the analysis discussion with internal ballistics by considering the hybrid rocket regression equation [Altman, 1995]

$$\dot{r} = aG^n x^m \quad (2.1)$$

where \dot{r} is the fuel regression rate (m/s), G is total propellant (oxidizer and fuel) mass flux rate ($\text{kg}/\text{m}^2.\text{s}$), x is distance down the port (m), a , n , m are regression rate constants, characteristic of the propellants.

From this equation we can see that regression rate varies with mass flux and also varies along the length of the port. Notice that the mass flux is the total flux including both the oxidizer injected and the fuel that has vaporized from the surface of the fuel wall, thus causing G to increase continuously down the port.

The mass flux rate is defined as the mass flow rate per unit cross-sectional area. As the fuel burns, the port cross-section area A_p increases and the mass flux rates G_f, G_o and G vary not only as a function of time t , but also as a function of the axial distance x . The propellant mass flux rate G [Altman, 1995] is given by

$$G = G_f(t, x) + G_o(t, x) \quad (2.2)$$

where G_f is the fuel mass flux rate and G_o is the liquid oxidizer mass flux rate. The solid fuel regression rate \dot{r} [Altman, 1995] depends on the propellant mass flux rate and the axial distance x from the port entrance.

$$\dot{r}(t, x) = \frac{dr(t, x)}{dt} = ax^m G^n = ax^m [G_f + G_o]^n \quad (2.3)$$

The fuel mass flux rate $G_f(t, x)$ can be obtained by integrating the amount of fuel released from the solid fuel grain, along the axis x of the port. The contact area between the solid fuel and the mixture of reacting gases in a port, between station x and $x+dx$ is given by $P_p(t, x)dx$, where $P_p(t, x)dx$ is the port perimeter at station x and time t .

The mass flow rate of fuel \dot{dm}_f generated in a single port between station x and $x+dx$ is

$$\dot{dm}_f = \rho_f \dot{r}(t, x) P_p(t, x) dx \quad (2.4)$$

where $P_p dx$ is the contact area between the liquid oxidizer and the solid fuel

The fuel flux rate in the grain between station x and $x+dx$ is given by

$$dG_f(t, x) = \dot{dm}_f / A_p \quad (2.5)$$

we define A_p as port cross-section area. The fuel mass flux rate generated between the entrance to the port $x = 0$ and station x is given by

$$G_f(t, x) = \int_0^x \frac{\dot{dm}_f}{A_p(t, \xi)} = \int_0^x \frac{\rho_f \dot{r}(t, \xi) P_p(t, \xi) d\xi}{A_p(t, \xi)} \quad (2.6)$$

where we have used ξ instead of x , as the integration coordinate. We define port cross-section area A_p and port perimeter P_p of a circle are given by

$$A_p(t) = \frac{\pi(D_0 + 2w(t))^2}{4} \quad (2.7)$$

$$P_p(t) = \pi(D_0 + 2w(t)) \quad (2.8)$$

where D_0 is the initial diameter of the circular port at time t and $w_f - w(t)$ is web thickness at any time t .

The ratio of initial perimeter to area appearing in equation (2.6) is given by

$$\frac{A_p(t)}{P_p(t)} = \frac{\frac{\pi(D_0 + 2w(t))^2}{4}}{\pi(D_0 + 2w(t))} = \frac{(D_0 + 2w(t))}{4} \quad (2.9)$$

Substituting (2.9) in equation (2.6), we have

$$G_f(t, x) = \int_0^x \frac{dm_f}{A_p(t, \xi)} = \int_0^x \frac{\rho_f \dot{r}(t, \xi) P_p(t, \xi) d\xi}{A_p(t, \xi)} = 4\rho_f \int_0^x \frac{\dot{r}(t, \xi) d\xi}{(D_0 + 2w(t))} \quad (2.10)$$

which is defined as fuel flux rate for the circular port

In order to obtain an accurate solution we have to take into account the regression rate variations along the axis of the port, i.e., the ξ or x coordinate. As we assume a simpler model, let us consider average values along the port axis. In this way, we eliminate the dependence on the coordinate x . In this case, the fuel flux rate can be approximated by the following expression

$$G_f(t, x) = 4\rho_f \frac{\dot{r}(t)}{D(t)} \int_0^{L_p} d\xi = \frac{4\rho_f L_p \dot{r}(t)}{(D_0 + 2w(t))} \quad (2.11)$$

where L_p is the port length. The regression rate can be approximated by substituting L_p^m instead of x^m is given by

$$\dot{r}(t, x) = \frac{dr(t, x)}{dt} = \frac{dw(t)}{dt} = aL_p^m [G_f(t) + G_o(t)]^n \quad (2.12)$$

we need an equation for the evolution of the port cross-section geometry. This can be obtained by taking the time derivative of thickness of web w at time t , which is a first order ordinary differential equation (ODE), which states that the rate of increase of the port diameter depends on the total mass flux rate (fuel flux rate plus oxidizer flux rate) in

the port. Before we can integrate this ODE with an initial condition for the web thickness, we need to develop expressions for the mass flux rates $G_f(t), G_o(t)$ appearing on the right hand side of the equation. We have already seen that the mass flux rate of the fuel is given by equation (2.11). Substituting the expression for the regression rate $\dot{r}(t)$ from equation (2.12) in equation (2.11) we have

$$G_f(t) = \frac{1}{(D_0 + 2w(t))} 4\rho_f a L_p^{m+1} [G_f(t) + G_o(t)]^n \quad (2.13)$$

In hybrid rockets, the total oxidizer mass flow rate \dot{m}_o is kept constant. We consider the oxidizer mass flow rate \dot{m}_o as a parameter which depends on the size of the rocket. Therefore, the oxidizer mass flux rate is given by

$$G_o(t) = \frac{\dot{m}_o}{N A_p} = \frac{4\dot{m}_o}{N\pi(D_0 + 2w(t))^2} \quad (2.14)$$

where N is number of ports in the solid fuel grain and $\frac{\dot{m}_o}{N}$ is the oxidizer mass flow rate per port. Substituting $G_o(t)$ value in equation (2.12) & (2.13), we get

$$\frac{dw}{dt} = a L_p^m [G_f(t) + \frac{4\dot{m}_o}{N\pi(D_0 + 2w(t))^2}]^n \quad (2.15)$$

$$G_f(t) = \frac{1}{(D_0 + 2w(t))} 4\rho_f a L_p^{m+1} [G_f(t) + \frac{4\dot{m}_o}{N\pi(D_0 + 2w(t))^2}]^n \quad (2.16)$$

where the initial value of $(D_0 + 2w(t))$ at time $t = 0$ is D_0 , where D_0 is the initial diameter of the circular port and port length of the grain L_p are design parameters that should be chosen carefully in order to achieve the required rocket performance and fulfill any geometrical and burn time constraints.

We have reduced the problem to the solution of two equations (2.15) & (2.16) with two unknowns, $w(t)$ and $G_f(t)$. Equation (2.15) is an ODE, whereas equation (2.16) is a

nonlinear algebraic equation for $G_f(t)$. This is known as a differential algebraic system, in which we need to integrate an ODE, while solving an implicit algebraic equation at every time step, in order to determine the right hand side of the ODE. We cannot solve equation (2.19) explicitly for $G_f(t)$ in terms of D_0 , but we can obtain an approximate solution or solve the equation iteratively. At every time step t , the structure of the algebraic equation is

$$G_f(t) = C_1(t)[G_f(t) + C_2(t)]^n \quad (2.17)$$

$$C_1(t) = \frac{4\rho_f a L_p^{m+1}}{(D_0 + 2w(t))} \quad (2.18)$$

$$C_2(t) = \frac{\dot{m}_o}{N(D_0 + 2w(t))^2} \quad (2.19)$$

This can be solved by the simple iteration

$$G_f(t)(i + 1) = C_1(t)[G_f(t)(i) + C_2(t)]^n \quad (2.20)$$

Here i is an iteration counter. In order to obtain an initial guess we assume $n \cong 1$ and obtain a linear equation for G_f^0

$$G_f^0(t) = C_1(t)[G_f^0(t) + C_2(t)] \quad (2.21)$$

$$G_f^0(t) = \frac{C_1(t)C_2(t)}{1 - C_1(t)} \quad (2.22)$$

where $C_1(t)$ is not equal to 1 at any time t . This initial guess is reasonable since n is usually in the range $n = [0.75, 0.8]$.

The Regression Equation in Non-Dimensional Form

Next we write the equations using non-dimensional variables, we define the following characteristic mass flux rates

$$G_{00} = \frac{\dot{m}_o}{NA_{p0}} = \frac{4\dot{m}_o}{N\pi D_0^2} \quad (2.23)$$

$$G_{f0} = \frac{G_{00}}{(OF)_0} \quad (2.24)$$

where G_{00} is the initial oxidizer mass flux rate, $\frac{\dot{m}_o}{N}$ is the oxidizer mass flow rate per port, A_{p0} is the initial port cross-sectional area, D_0 is the initial diameter of the circular port and $(OF)_0$ is the initial oxidizer to fuel ratio. G_{f0} is the initial fuel mass flux rate. We define non-dimensional variables, denoted by bars in the following way

$$w = \bar{w}D_0, t = \tau\bar{t}, G_o = G_{00}\bar{G}_o, G_f = G_{f0}\bar{G}_f, \tau = \frac{w_f}{\dot{r}_0} \quad (2.25)$$

$$\dot{r}_0 = aL_p^m(G_{00} + G_{f0})^n \quad (2.26)$$

Here τ is a characteristic time defined by $\frac{w_f}{\dot{r}_0}$, where w_f is the final fuel web thickness and \dot{r}_0 is the initial solid fuel regression rate. Upon substituting the new values for different variables in Equations (2.26), (2.15), and (2.16), we obtain

Using $G_{f0} = \frac{G_{00}}{(OF)_0}$ in the above equation, we get

$$\dot{r}_0 = aL_p^m G_{f0}^n ((OF)_0 + 1)^n \quad (2.27)$$

The area A_p and perimeter P_p at any time are given by

$$A_p = \frac{\pi(D_0 + 2w)^2}{4} \quad (2.28)$$

$$P_p = \pi(D_0 + 2w) \quad (2.29)$$

Based on the values of A_p & P_p , the oxidizer and fuel mass fluxes are defined as

$$G_o = \frac{\dot{m}_o}{NA_p} = \frac{4\dot{m}_o}{N\pi(D_0 + 2w)^2} \quad (2.30)$$

$$G_f = \frac{4\rho_f L_p \dot{r}(t) \pi (D_0 + 2w)}{\pi (D_0 + 2w)^2}$$

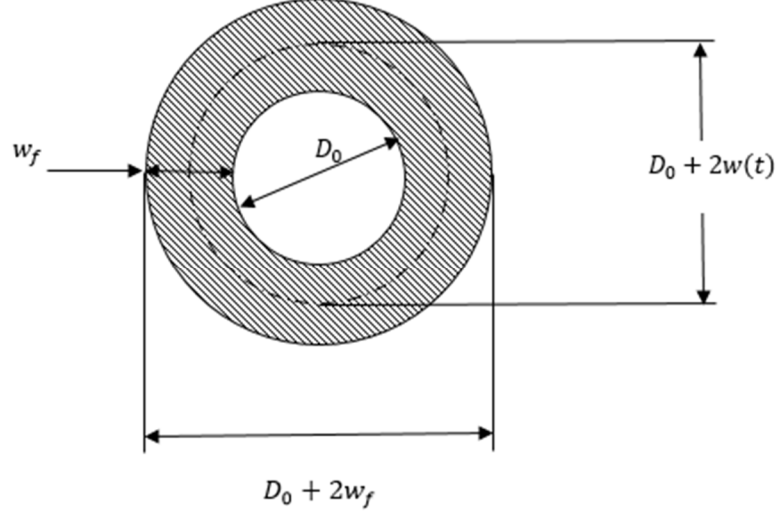


Figure 2.1. Schematic of cross-section of solid fuel grain

Substituting \dot{r} from equation (2.12) in the above equation we get

$$G_f = a\rho_f L_p^{m+1} (G_o + G_f)^n \frac{4}{D_0 + 2w} \quad (2.31)$$

Non-dimensionalizing equations (2.31) and (2.30), we get

$$G_{f0} \bar{G}_f = a\rho_f L_p^{m+1} (G_{o0} \bar{G}_o + G_{f0} \bar{G}_f)^n \frac{4}{D_0 (1 + 2\bar{w})}$$

Using $G_{f0} = \frac{G_{o0}}{(OF)_0}$ in the above equation, we get

$$G_{f0} \bar{G}_f = a\rho_f L_p^{m+1} G_{f0}^n ((OF)_0 \bar{G}_o + \bar{G}_f)^n \frac{4}{D_0 (1 + 2\bar{w})} \quad (2.32)$$

But from equation (2.27)

$$a L_p^m G_{f0}^n = \frac{\dot{r}_0}{((OF)_0 + 1)^n} \quad (2.33)$$

Substituting equation (2.33) in equation (2.32), we get

$$G_{f0}\bar{G}_f = \frac{4L_p\rho_f\dot{r}_0}{D_0} \frac{1}{((OF)_0 + 1)^n} ((OF)_0\bar{G}_o + \bar{G}_f)^n \frac{1}{(1 + 2\bar{w})}$$

$$\text{But } G_{f0} = L_p\rho_f\dot{r}_0 \frac{p_{p0}}{A_{p0}} = L_p\rho_f\dot{r}_0 \frac{\pi D_0}{(\frac{\pi D_0^2}{4})} = \frac{4L_p\rho_f\dot{r}_0}{D_0}$$

$$\bar{G}_f = \frac{1}{((OF)_0 + 1)^n} ((OF)_0\bar{G}_o + \bar{G}_f)^n \frac{(4 + 2\pi\bar{w})}{(1 + 4\bar{w} + \pi\bar{w}^2)} \quad (2.34)$$

Now, let us find equation for \bar{G}_o with respect to non-dimensional variables

$$\bar{G}_o = \frac{G_o}{G_{o0}}$$

$$\bar{G}_o = \frac{\frac{\dot{m}_o}{N(D_0^2 + 4D_0w + 4w^2)}}{\frac{\dot{m}_o}{ND_0^2}}$$

$$\bar{G}_o = \frac{D_0^2}{(D_0^2 + 4D_0w + 4w^2)}$$

Non-dimensionalizing the above equation with $w = \bar{w}D_0$, we get

$$\bar{G}_o = \frac{1}{(1 + 4\bar{w} + 4\bar{w}^2)} \quad (2.35)$$

Let $t = \tau\bar{t}$ and Consider equation (2.12),

$$\dot{r} = \frac{dw}{dt} = aL_p^m [G_f + G_o]^n \quad (2.36)$$

$$\frac{D_0}{\tau} \frac{d\bar{w}}{d\bar{t}} = aL_p^m (G_{o0}\bar{G}_o + G_{f0}\bar{G}_f)^n$$

$$\frac{d\bar{w}}{d\bar{t}} = \frac{\tau}{D_0} aL_p^m G_{f0}^n ((OF)_0\bar{G}_o + \bar{G}_f)^n$$

Substituting equation (2.33) in the above equation, and using $\tau = \frac{w_f}{\dot{r}_0}$

$$\frac{d\bar{w}}{d\bar{t}} = \frac{w_f}{\dot{r}_0} \frac{1}{D_0} \frac{\dot{r}_0}{((OF)_0 + 1)^n} ((OF)_0\bar{G}_o + \bar{G}_f)^n$$

After cancelling \dot{r}_0

$$\frac{d\bar{w}}{d\bar{t}} = \frac{w_f}{D_0} \frac{1}{((OF)_0 + 1)^n} ((OF)_0 \bar{G}_o + \bar{G}_f)^n \quad (2.37)$$

This initial value of \bar{w} becomes the initial condition for the ODE

$$\bar{w}(0) = 0, (OF)_0 = 2$$

$$\dot{m}_{prop} = \dot{m}_o + \dot{m}_f \quad (2.38)$$

where \dot{m}_{prop} is the mass flow rate of the propellant

In order to check the accuracy of the procedure, we need to compare our results with the reference values. In this process we need to find more characteristics of the model like the thrust, the chamber pressure, the exit velocity and the specific impulse of the fuel grain. Below equations are used to find the appropriate values of the flow properties. These equations are purely based on the choice of propellant type and the propellant considered for our reference is the combination of N_2O_4 and HTPB. N_2O_4 is an oxidizer and HTPB is a fuel. These equations are taken from [Altman, 1995] Appendix B.

$$T_f = -15.854(OF)^4 + 314.21(OF)^3 - 2334.4(OF)^2 + 7623.5(OF) - 5742.5 \quad (2.39)$$

$$MW = 0.1126(OF)^3 - 1.8711(OF)^2 + 11.386(OF) + 3.8214 \quad (2.40)$$

$$\begin{aligned} \gamma = & 0.000672(OF)^4 - 0.013233(OF)^3 + 0.09848(OF)^2 - 0.330475(OF) \\ & + 1.645795 \end{aligned} \quad (2.41)$$

where T_f, MW, γ are temperature, molecular weight and isentropic parameter of the propellant

$$c^* = \frac{0.95\sqrt{\gamma RT_f}}{f(\gamma)} \quad (2.42)$$

$$f(\gamma) = \gamma \left(\frac{2}{\gamma + 1} \right)^{\frac{\gamma+1}{2\gamma-2}}$$

where c^* is the characteristic velocity, R is the gas constant.

$$A_t = \frac{\dot{m}_{prop0} c^*}{P_{c0}} \quad (2.43)$$

where \dot{m}_{prop0} is the initial propellant mass flow rate, P_{c0} is the initial chamber pressure and A_t is the throat area.

$$P_c = \frac{\dot{m}_{prop} c^*}{A_t} \quad (2.44)$$

where P_c is the chamber pressure at any time t

$$A_e = \varepsilon A_t \quad (2.45)$$

where A_e is the exit area and ε is the expansion ratio

$$V_e = \sqrt{\frac{2\gamma RT_f}{(\gamma - 1)} \left\{ 1 - \left(\frac{P_e}{P_c} \right)^{\frac{\gamma-1}{\gamma}} \right\}} \quad (2.46)$$

where V_e is the exit velocity and P_e is the exit pressure

$$F = 0.98(\dot{m}_{prop} V_e + P_e A_e) \quad (2.47)$$

where F is the thrust

$$I_{sp} = \frac{F}{\dot{m}_{prop} g_0} \quad (2.48)$$

where I_{sp} is the specific impulse and g_0 is the gravitational acceleration

Numerical Results

Having determined the non-dimensional parameters, we can solve the non-dimensional internal ballistics equations numerically using a standard ODE solver

$$\frac{d\bar{w}}{d\bar{t}} = \frac{w_f}{D_0} \frac{1}{((OF)_0 + 1)^n} ((OF)_0 \frac{1}{(1 + 4\bar{w} + 4\bar{w}^2)} + \bar{G}_f)^n \quad (2.37)$$

$$\bar{G}_f = \frac{1}{((OF)_0 + 1)^n} ((OF)_0 \frac{1}{(1 + 4\bar{w} + 4\bar{w}^2)} + \bar{G}_f)^n \frac{(4 + 2\pi\bar{w})}{(1 + 4\bar{w} + \pi\bar{w}^2)} \quad (2.34)$$

with initial condition $\bar{w}(0) = 0$ and $(OF)_0 = 2$. The initial Oxidizer to fuel ratio is chosen as 2 since there is a OF shift along the burn time and this is the minimum value for the choice of propellant. Initial guess for w_f is taken to be 7 cm.

We now have the first order differential equation supported by the algebraic function. This first order ODE is integrated from $t = 0$ to 60 seconds, which is then solved for getting the values of $G_f(t), G_o(t), \dot{r}(t), w(t), OF(t)$. Based on these values the remaining flow properties are calculated.

Results & Discussion for single circular port solid grain

The solid fuel grain of length 4 meters is considered with a diameter of 0.152 meters.

Density is 1000 kg/m^3 , Initial chamber pressure is 3.45 MPa, Exit Pressure is 13800 Pa

$a = 2.066\text{e-}5$, $n = 0.75$, $m = -0.15$, $\dot{m}_o = 7.95 \text{ kg/s}$, $(OF)_0 = 2$, $\varepsilon = 70$

The value of w_f obtained for the single circular port is used to calculate the mass of the fuel grain as follows.

$$m_f = \text{volume} * \text{Density}$$

$$m_f = \left\{ \frac{\pi}{4} (D_1^2 + 2w_f^2) - \frac{\pi}{4} D_1^2 \right\} L_{p1} \rho_f$$

$$m_f = \pi w_f (w_f + D_1) L_{p1} \rho_f \quad (2.49)$$

where m_f is the mass of the solid fuel, D_1 is the diameter of the single circular port and L_{p1} is the length of single port solid fuel grain. From the results the web thickness obtained is equal to 0.0693 m, and the mass of the fuel obtained is equal to 192 kg. The Oxidizer mass flux for the single port is beginning from $438 \text{ kg/m}^2\text{s}$ and reaching a value of $120 \text{ kg/m}^2\text{s}$. The fuel flux is varying from $219 \text{ kg/m}^2\text{s}$ to $39 \text{ kg/m}^2\text{s}$, these

values are decreasing with time which is true for a Hybrid rocket engine. The thrust produced by this fuel grain is equal to 34 KN and the chamber pressure is equal to 3.45 MPa. The specific impulse increases from 293 to 297 and it is within the range of hybrid rockets. The exit velocity varies from 2536 (m/sec) to 2522 (m/sec). Mass flux has a practical upper limit. With liquid oxidizers, flooding [Humble, 1995] can occur, extinguishing the flame. Gaseous oxidizers also have this limit, termed blow-off. This phenomenon is analogous to extinguishing a candle by vigorously blowing on it. Typically the upper limit on oxidizer mass flux is between 350 and 700 kg/m^2s . The lower limit is a conservative initial estimate for liquids; the higher limit is more appropriate for gases.

Validation of Results

The results obtained from the above procedure are then compared to the values of

[Altman, 1995] chapter-7, page-382, Table-7.1.

x(m)	t = 0.1 sec			t = 20 sec			t = 60 sec		
	Port Dia.(m)	\dot{r} (cm/sec)	O/F	Port Dia.(m)	\dot{r} (cm/sec)	O/F	Port Dia.(m)	\dot{r} (cm/sec)	O/F
0.381	0.152	0.263	17.19	0.227	0.143	21.34	0.315	0.087	24.11
0.762	0.152	0.231	9.102	0.22	0.131	11.4	0.301	0.081	13.2
1.143	0.152	0.221	6.316	0.217	0.127	7.983	0.296	0.078	9.64
1.524	0.152	0.217	4.835	0.216	0.125	6.139	0.293	0.077	7.249
1.905	0.152	0.215	3.917	0.215	0.123	4.974	0.292	0.076	6.006
2.286	0.152	0.215	3.31	0.215	0.123	4.177	0.291	0.076	4.972
2.667	0.152	0.215	2.852	0.215	0.123	3.594	0.291	0.076	4.342
3.048	0.152	0.216	2.506	0.215	0.123	3.115	0.291	0.075	3.757
3.429	0.152	0.218	2.234	0.216	0.123	2.771	0.291	0.075	3.375
3.81	0.152	0.219	2.016	0.216	0.123	2.495	0.292	0.075	3.008
4.191	0.152	0.221	1.831	0.216	0.124	2.263	0.292	0.075	2.747
4.572	0.152	0.224	1.667	0.217	0.124	2.073	0.293	0.076	2.492

Table. 2.1. Reference Values for the results from Altman for a single circular port

Port Length (m)	t = 0.1 sec			t = 60 sec		
	Port Dia. (m)	\dot{r} (cm/sec)	O/F	Port Dia.(m)	\dot{r} (cm/sec)	O/F
4	0.152	0.216	2.007	0.2213	0.075	3.025

Table. 2.2. Results obtained by the proposed procedure for a single circular port

As we are not considering the variations along the axial length there is a slight difference in the resulting values. The flow properties based on the above values are presented below from Fig 2.2 to Fig. 2.6.

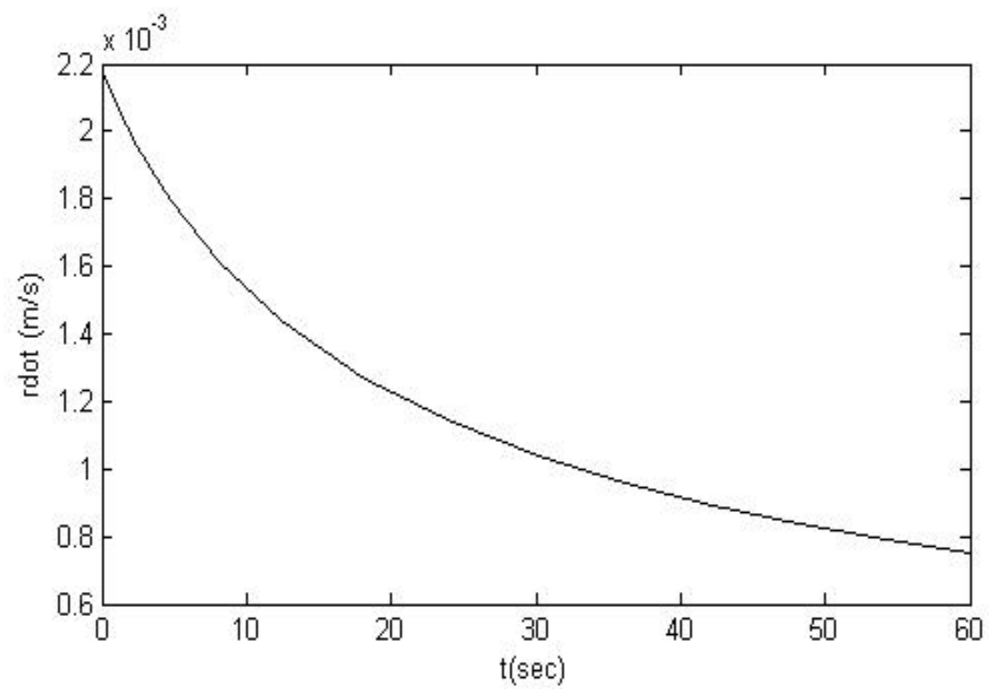
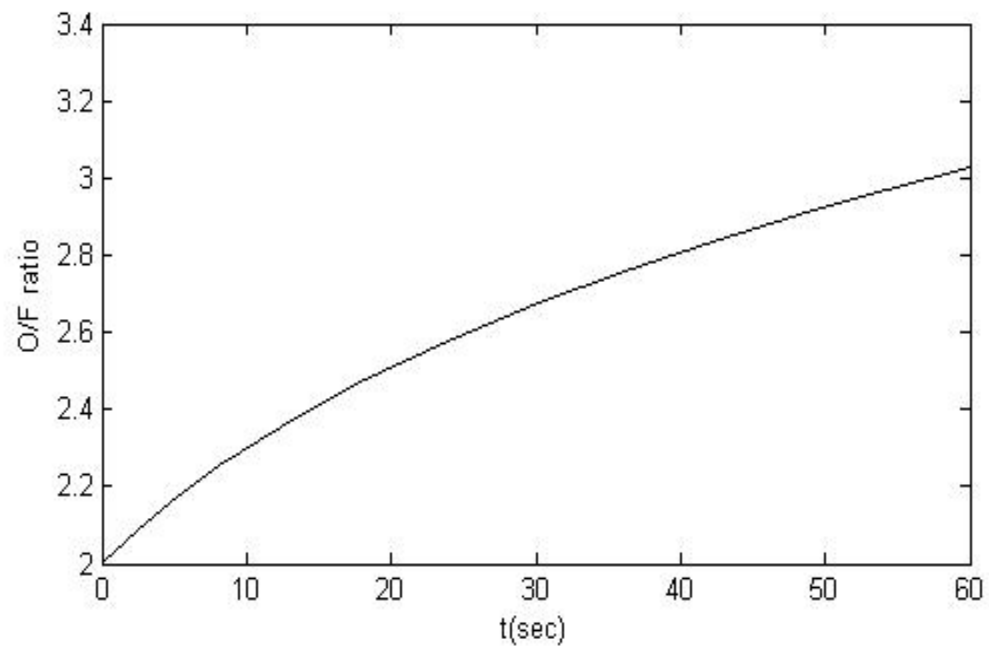


Figure. 2.2. (O/F) ratio and Regression rate vs Burn Time

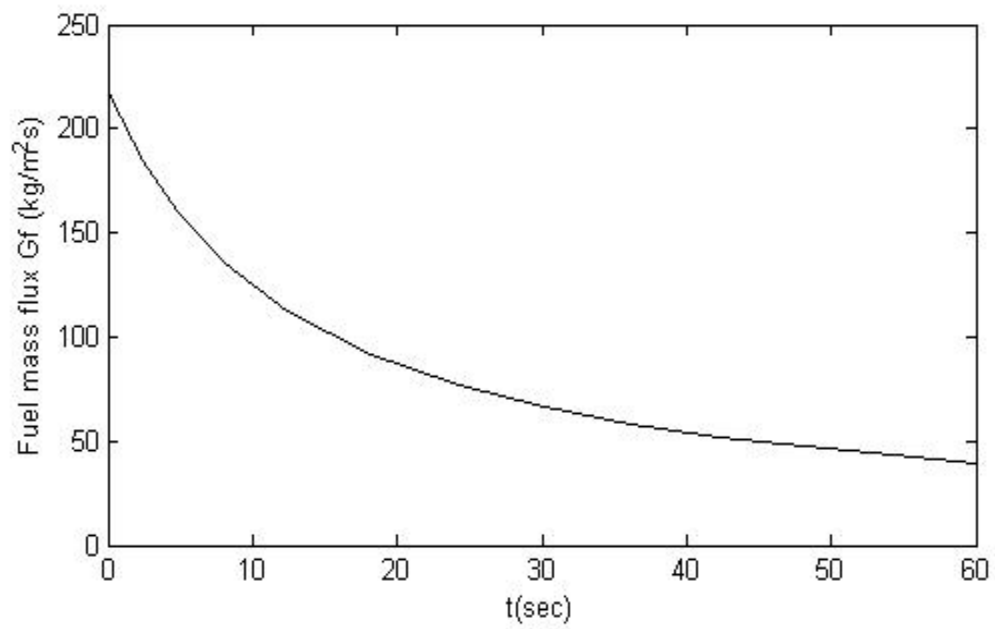
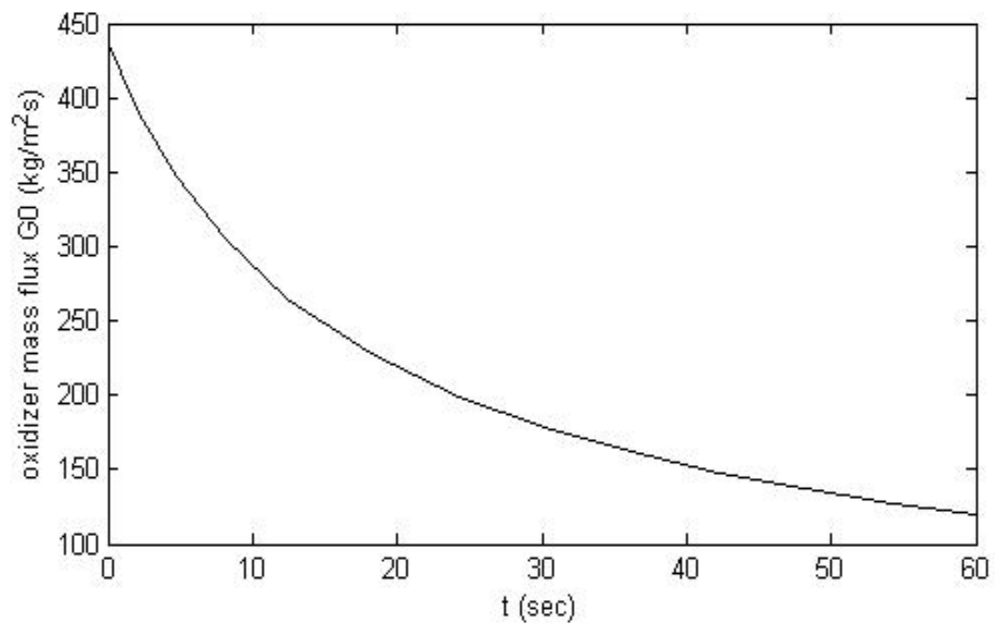


Figure. 2.3. Oxidizer mass flux and Fuel mass flux vs Burn Time

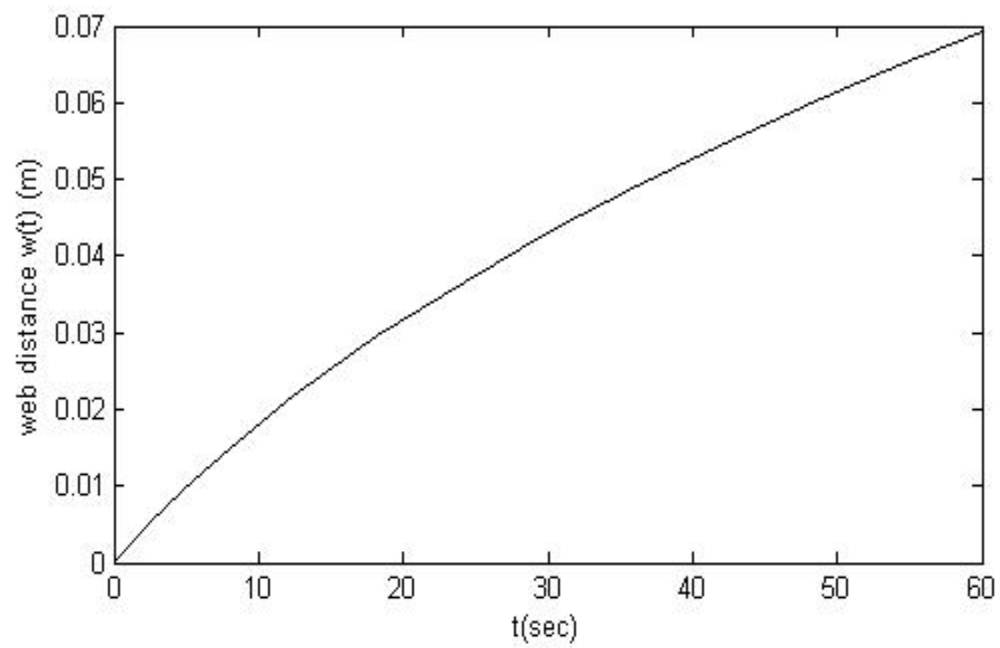
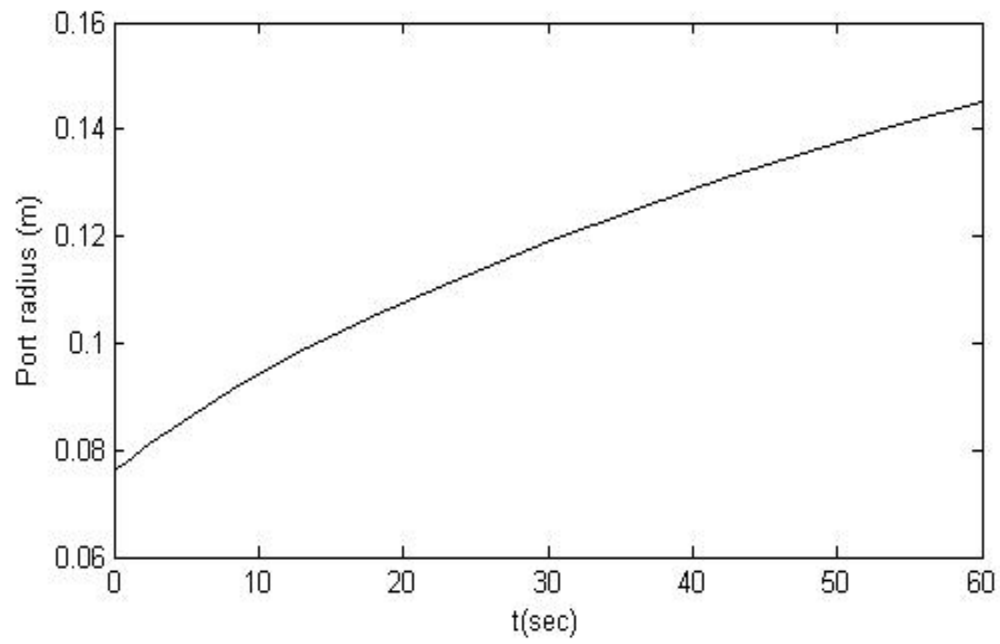


Figure. 2.4. Port radius and Web thickness vs Burn Time

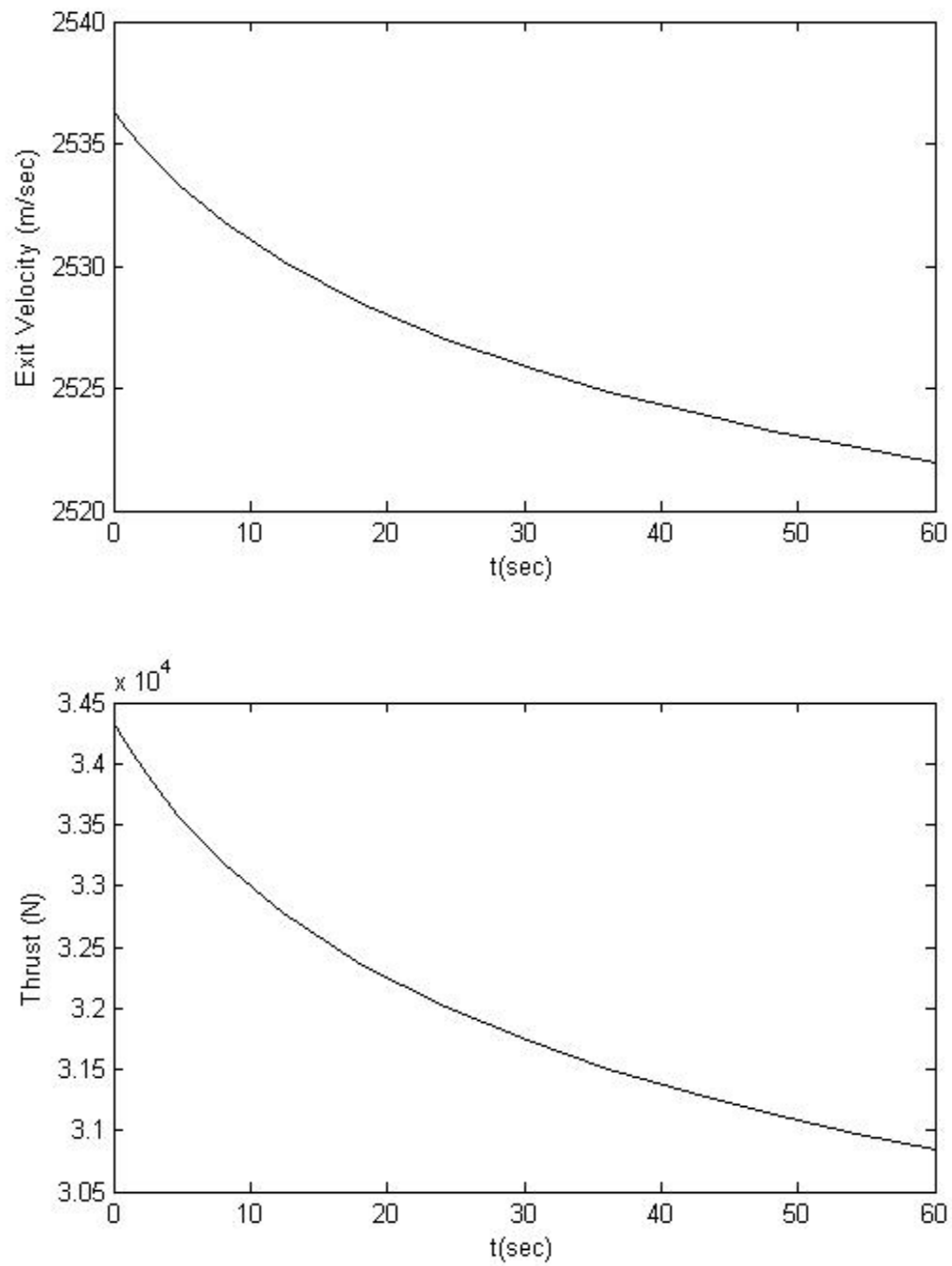


Figure. 2.5. Exit Velocity and Thrust vs Burn Time

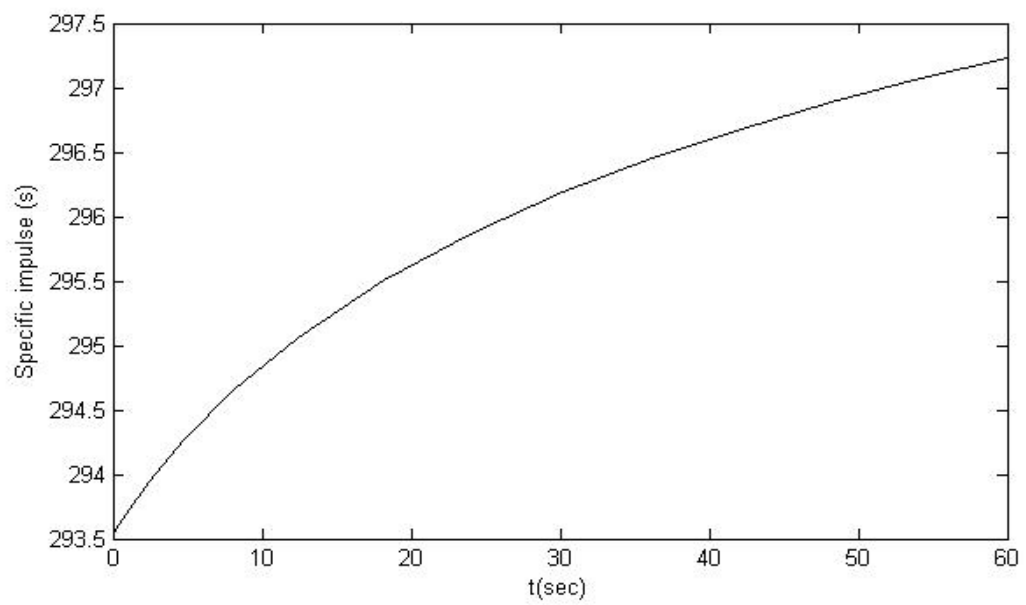
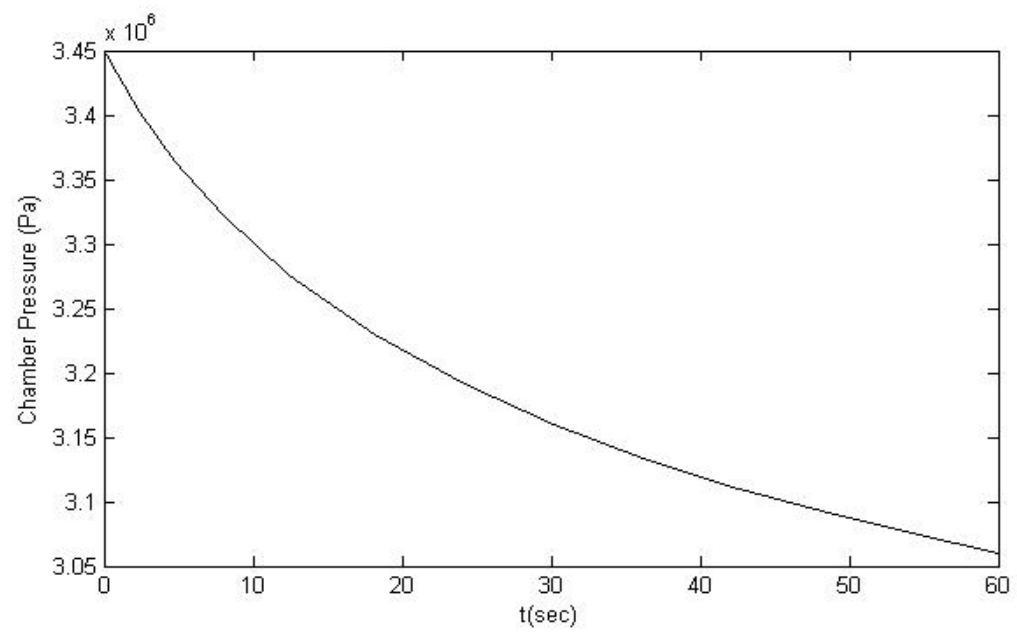


Figure. 2.6. Chamber Pressure and Specific Impulse vs Burn Time

Results & Discussion for four circular ports solid grain

$$m_f = \text{volume} * \text{Density}$$

$$m_f = N \pi w_f (w_f + D_4) L_{p4} \rho_s$$

$$192 = 4 \pi 0.0693 (0.0693 + D_4) L_{p4} 1000 \quad (2.50)$$

By considering the same amount of solid fuel and same amount of web thickness as for the single port, see equation (2.49), the above equation is iterated to produce the same amount of burn time by varying the number of ports. The final values for the above equation are D_4 is 0.0406 and L_{p4} is 2.01m. The results obtained for this case are presented below from Fig. 2.7 to Fig. 2.11.

Port Length (m)	t = 0.1 sec			t = 60 sec		
	Port Dia.(m)	\dot{r} (cm/sec)	O/F	Port Dia.(m)	\dot{r} (cm/sec)	O/F
2.01	0.0406	0.551	2.007	0.1099	0.056	4.962

Table 2.3. Results obtained by the proposed procedure for 4 circular ports

The Oxidizer mass flux through each of the four ports is ranging from $1400 \text{ kg/m}^2\text{s}$ to reaching a value of $78 \text{ kg/m}^2\text{s}$. The fuel flux is varying from $767 \text{ kg/m}^2\text{s}$ to $15 \text{ kg/m}^2\text{s}$. However the thrust produced by this fuel grain is equal to 34 KN and the chamber pressure is equal to 3.45 MPa which are equal to those from a single port. The specific impulse increases from 293 to 300 sec and the exit velocity varies from 2536 (m/sec) to 2509 (m/sec).

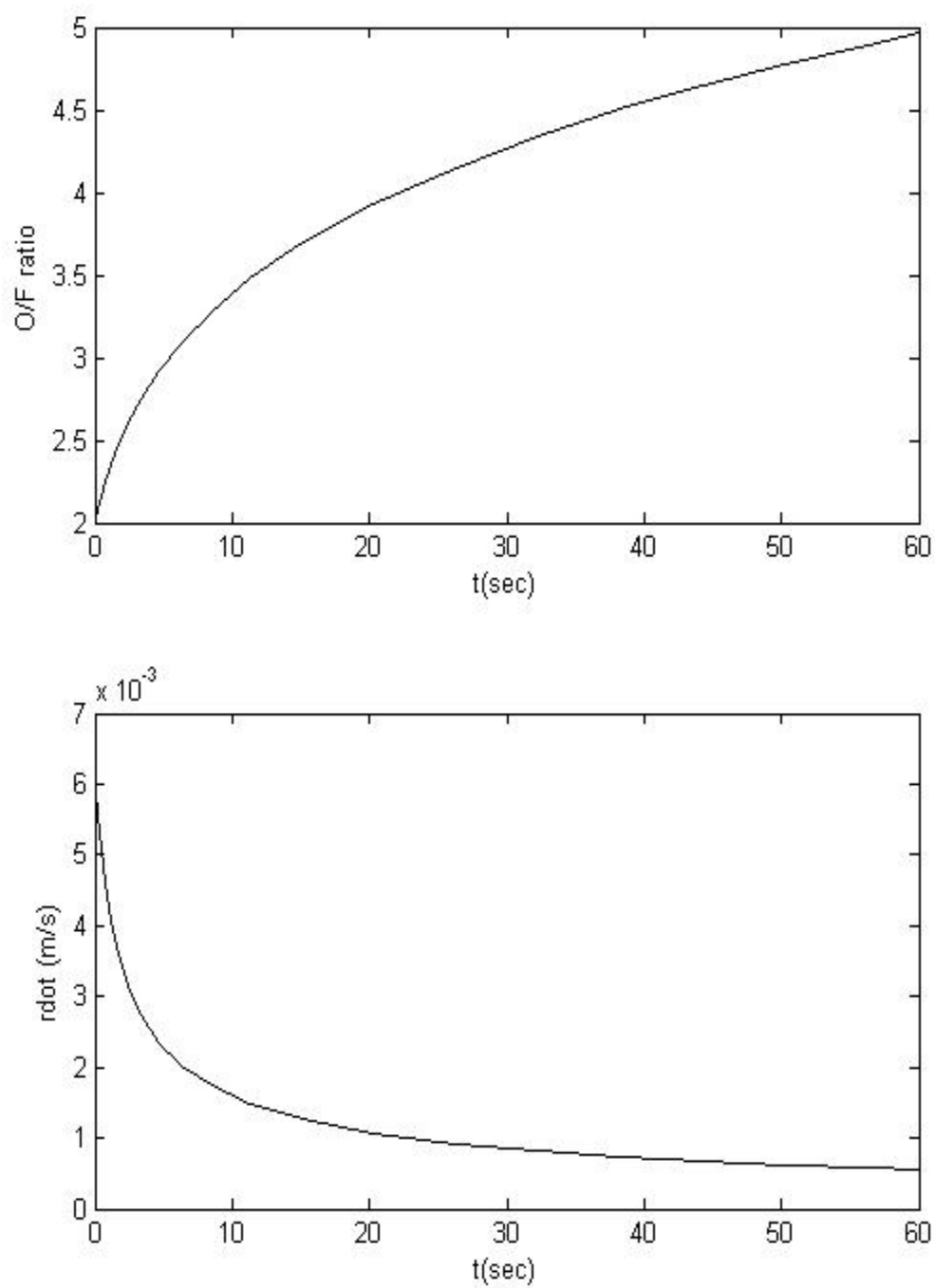


Figure. 2.7. (O/F) ratio and Regression rate vs Burn time

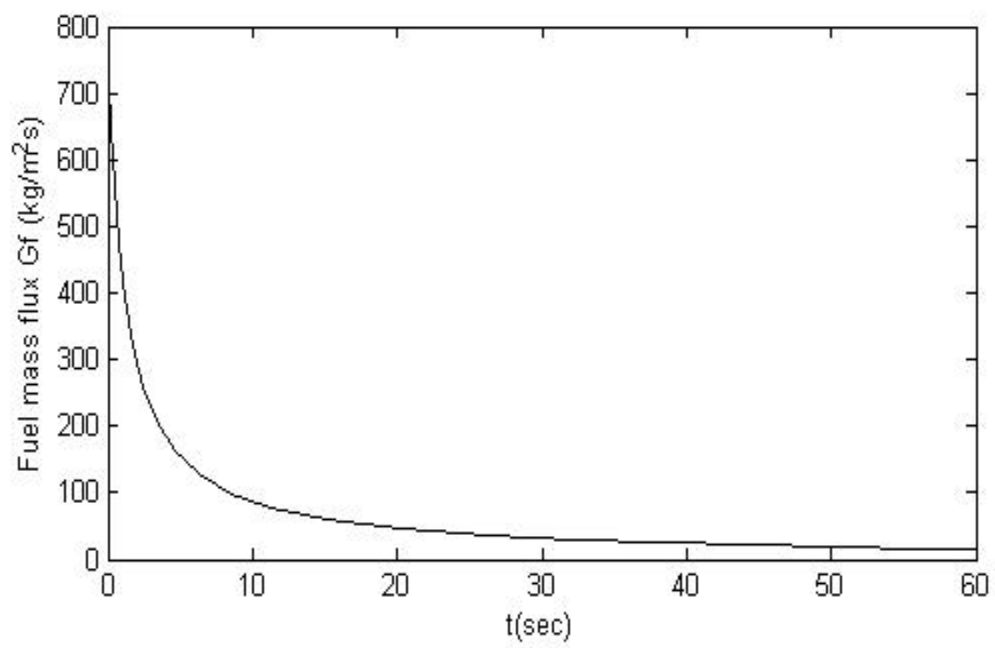
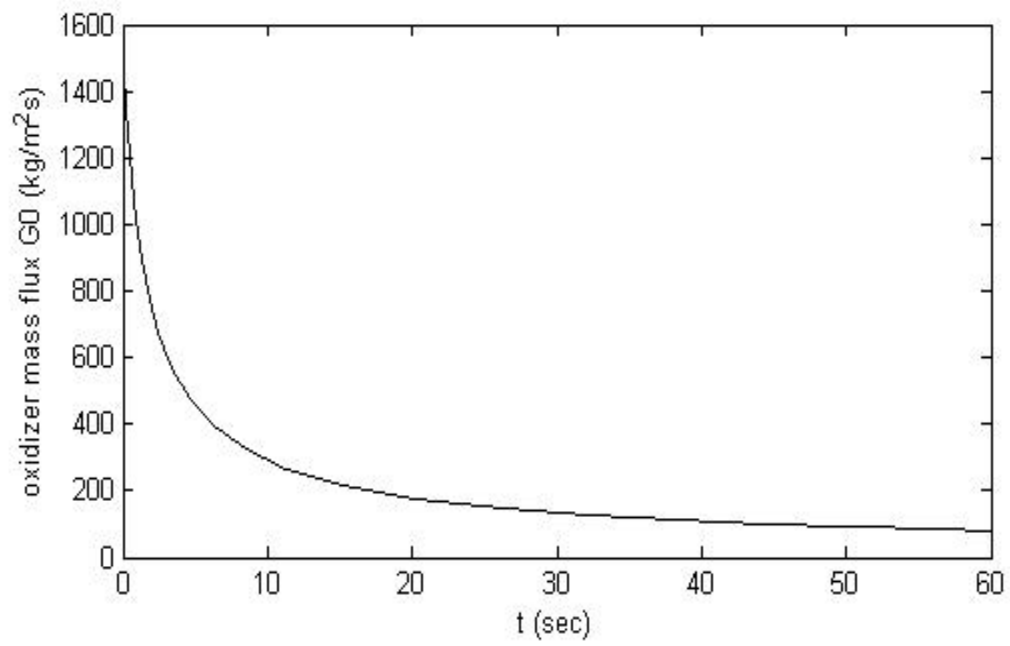


Figure. 2.8. Oxidizer mass flux and the Fuel mass flux vs Burn time

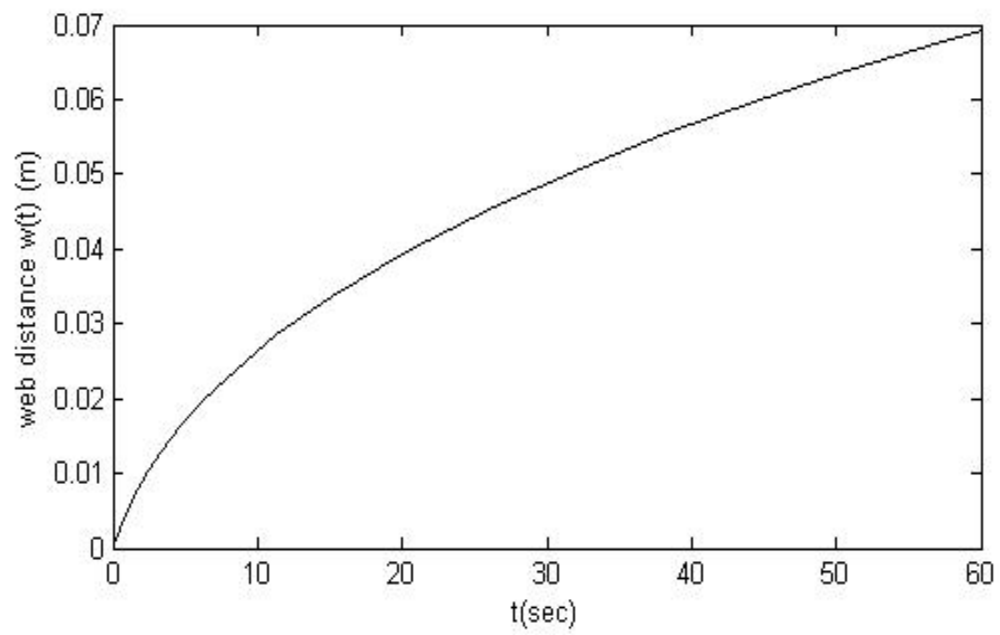
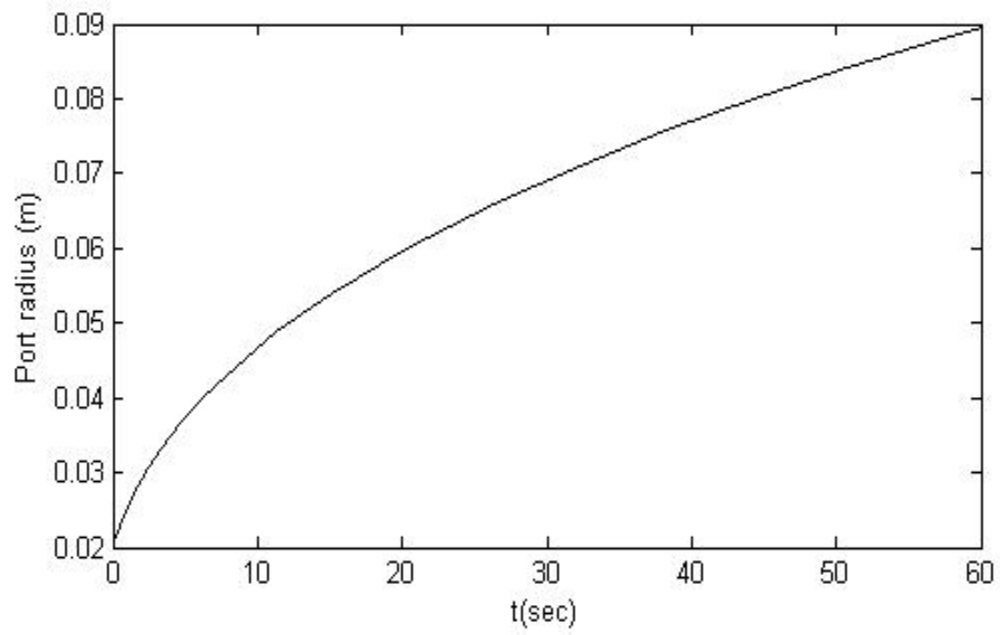


Figure. 2.9. Port radius and Web thickness vs Burn time

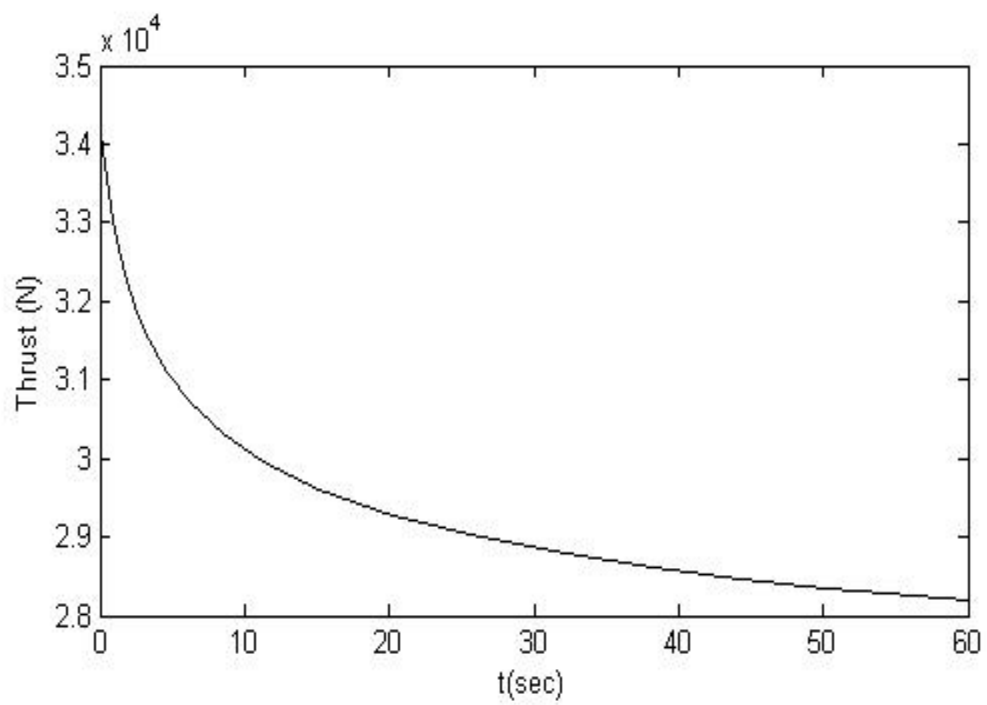
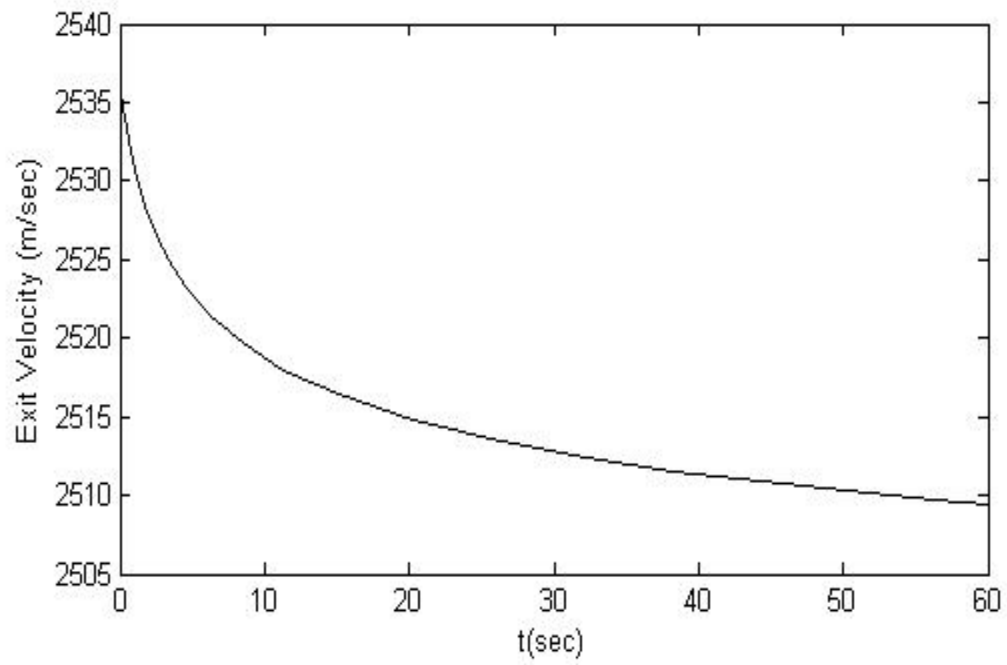


Figure. 2.10. Exit Velocity and Thrust vs Burn time

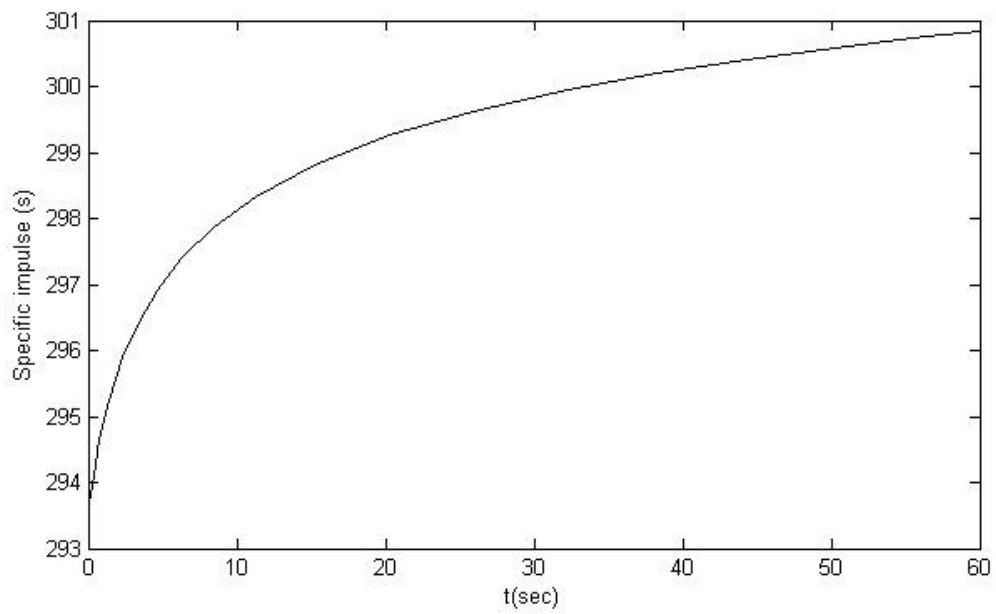
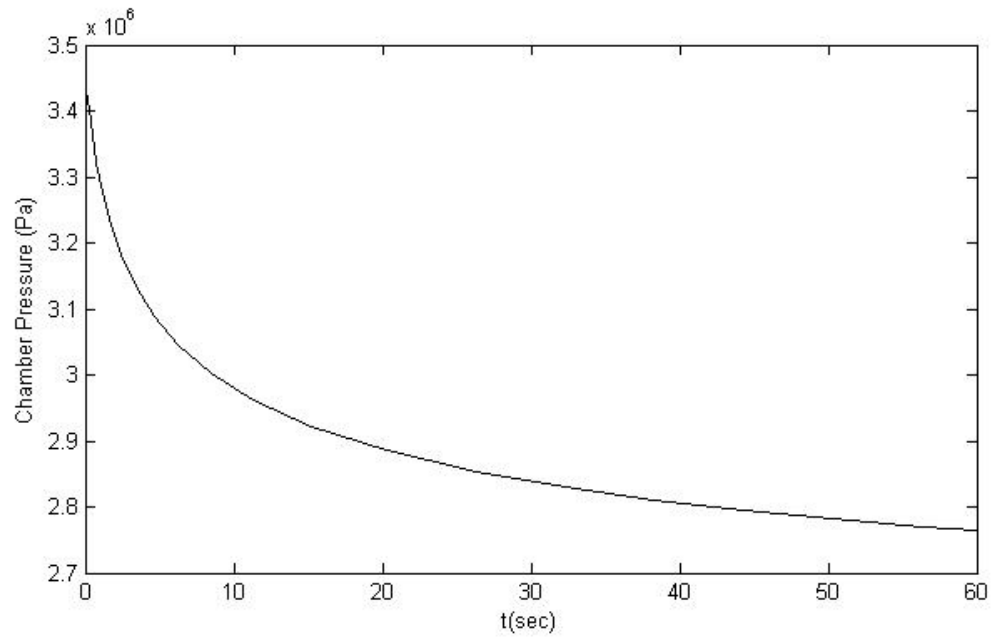


Figure. 2.11. Chamber Pressure and Specific Impulse vs Burn time

Chapter III

Hybrid-Motor Ballistics for Square ports

Introduction

This chapter considers different number of square ports that are transformed from the same amount of fuel from the circular port. The internal ballistics are analyzed for these port geometries and the optimum value for the number of ports is reached based on the volumetric efficiency graph for the same amount of fuel.

Volumetric Efficiency for square ports

The number of ports, web thickness, and oxidizer mass flux influence volumetric efficiency [Altman, 1995]. For a web of given size in a given chamber, we want to be as near to the maximum volumetric efficiency as possible because this gives us the smallest engine. For a small number of ports (N), the corresponding number of webs limits the total web cross section. In order to obtain the volumetric efficiency curve of the fuel grain let us make the fuel surface area, the mass of the solid fuel and the web thickness as constants. Constant web thickness gives us the constant burn time and constant surface area of the grain maintains constant volume. By making the mass of the fuel constant, we can determine the best selection of number of ports for the given amount of fuel. The volumetric efficiency can be obtained by working on different number of ports with the constraints mentioned below.

$$\text{Volumetric efficiency} = \frac{\text{Volume of the solid fuel}}{\text{Total volume of the chamber}}$$

Single Square Port

Let us consider a solid fuel grain with a square cross section and single square port of side b_1 each with fuel web thickness w_f . The side of the total fuel grain

with single port is $B_1 = b_1 + 2w_f$, where B_1 is the side of total fuel grain. The initial area of the square port is b_1^2 and total area of the fuel grain including the port is given by $(b_1 + 2w_f)^2$

The surface area of the solid fuel with single port is given by

$$A_{sf1} = (b_1 + 2w_f)^2 - b_1^2 \quad (3.1)$$

$$A_{sf1} = b_1^2 + 4b_1w_f + 4w_f^2 - b_1^2$$

$$A_{sf1} = 4w_f(b_1 + w_f) \quad (3.2)$$

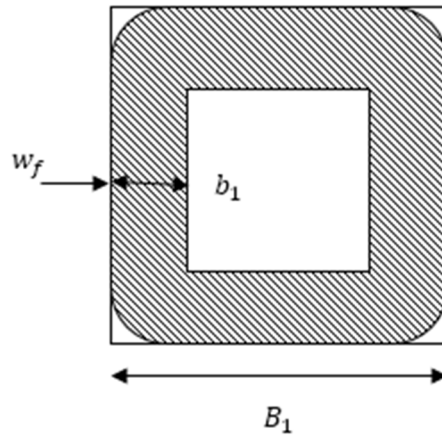


Figure 3.1. Schematic of cross-section of square solid fuel grain with single port

where A_{sf1} is the surface area of solid fuel with single port, the total volume of the solid grain can be obtained by multiplying the surface area with the total length of the grain (not shown in the figure).

$$V_{sf1} = A_{sf1}L_p \quad (3.3)$$

where V_{sf1} is the volume of solid fuel grain with single port, the total mass required for the desired burn time can be obtained by multiplying volume of the solid fuel with the density of the solid fuel. The total mass m_{f1} is given by

$$\begin{aligned} m_{f1} &= V_{sf1}\rho_f \\ m_{f1} &= A_{sf1}L_p\rho_f \\ m_{f1} &= 4w_f(b_1 + w_f)L_p\rho_f \end{aligned} \quad (3.4)$$

Four Square Ports

Let us consider a solid fuel grain with a square cross section and four square ports of side b_4 each with fuel web thickness w_f . The side of the total fuel grain with four ports is $B_4 = 2b_4 + 4w_f$, where B_4 is the side of the total solid fuel grain. The initial area of the square port is b_4^2 and total area of the solid fuel grain including the port is given by $(2b_4 + 4w_f)^2$

The surface area of the solid fuel with four ports is given by

$$A_{sf4} = (2b_4 + 4w_f)^2 - 4b_4^2 \quad (3.5)$$

$$A_{sf4} = 4b_4^2 + 16b_4w_f + 16w_f^2 - 4b_4^2$$

$$A_{sf4} = 16w_f(b_4 + w_f) \quad (3.6)$$

where A_{sf4} is the surface area of solid fuel grain with four ports, the total volume of the solid grain can be obtained by multiplying the surface area with the total length of the grain (not shown in the figure).

$$V_{sf4} = A_{sf4}L_p \quad (3.7)$$

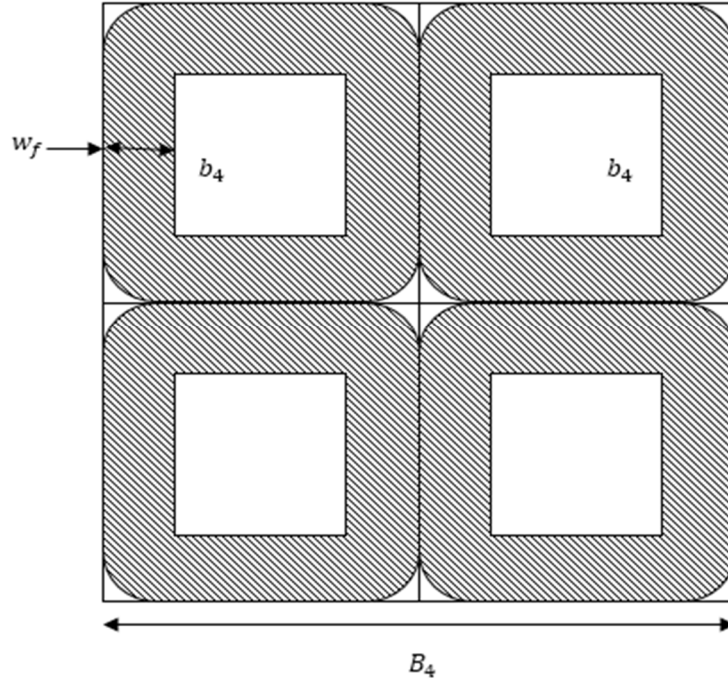


Figure 3.2. Schematic of cross-section of square solid fuel grain with four ports

where V_{sf4} is the volume of solid fuel grain with four ports, the total mass required for the desired burn time can be obtained by multiplying volume of the solid fuel with the density of the solid fuel. The total mass m_{f4} is given by

$$m_{f4} = V_{sf4}\rho_f$$

$$m_{f4} = A_{sf4}L_p\rho_f$$

$$m_{f4} = 16w_f(b_4 + w_f)L_p\rho_f \quad (3.8)$$

Nine Square Ports

Let us consider a solid fuel grain with a square cross section and nine square ports of side b_9 each with fuel web thickness w_f . The side of the total fuel grain with nine ports is $B_9 = 3b_9 + 6w_f$, where B_9 is the side of the total solid fuel grain. The initial area of

the square port is b_9^2 and total area of the solid fuel grain including the port is given by $9(b_9 + 2w_f)^2$

The surface area of the solid fuel with nine ports is given by

$$A_{sf9} = 9(b_9 + 2w_f)^2 - 9b_9^2 \quad (3.9)$$

$$A_{sf9} = 9b_9^2 + 36b_9w_f + 36w_f^2 - 9b_9^2$$

$$A_{sf9} = 36w_f(b_9 + w_f) \quad (3.10)$$

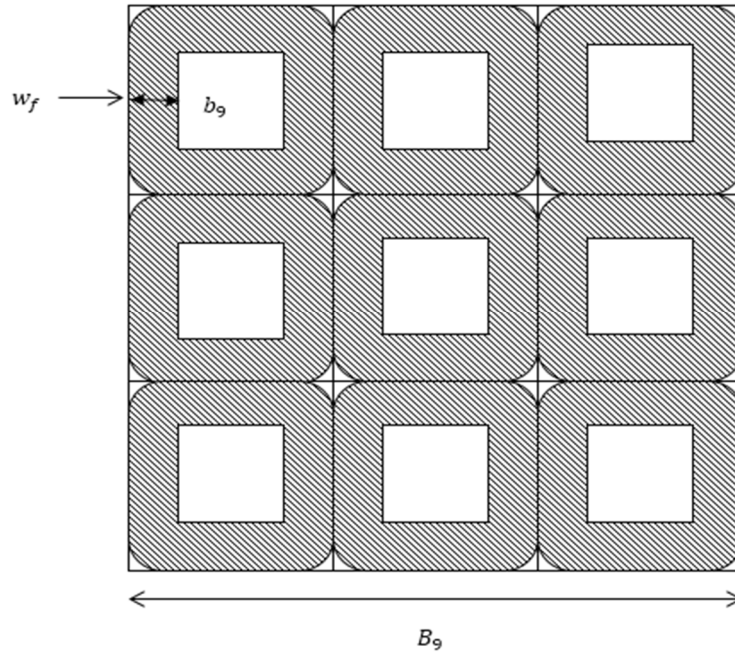


Figure 3.3. Schematic of cross-section of square solid fuel grain with nine ports

where A_{sf9} is the surface area of solid fuel grain with nine ports, the total volume of the solid grain can be obtained by multiplying the surface area with the total length of the grain (not shown in the figure).

$$V_{sf9} = A_{sf9}L_p \quad (3.11)$$

where V_{sf9} is the volume of solid fuel grain with nine ports, the total mass required for the desired burn time can be obtained by multiplying volume of the solid fuel with the density of the solid fuel. The total mass m_{f9} is given by

$$\begin{aligned} m_{f9} &= V_{sf9} \rho_f \\ m_{f9} &= A_{sf9} L_p \rho_f \\ m_{f9} &= 36 w_f (b_9 + w_f) L_p \rho_f \end{aligned} \quad (3.12)$$

Sixteen Square Ports

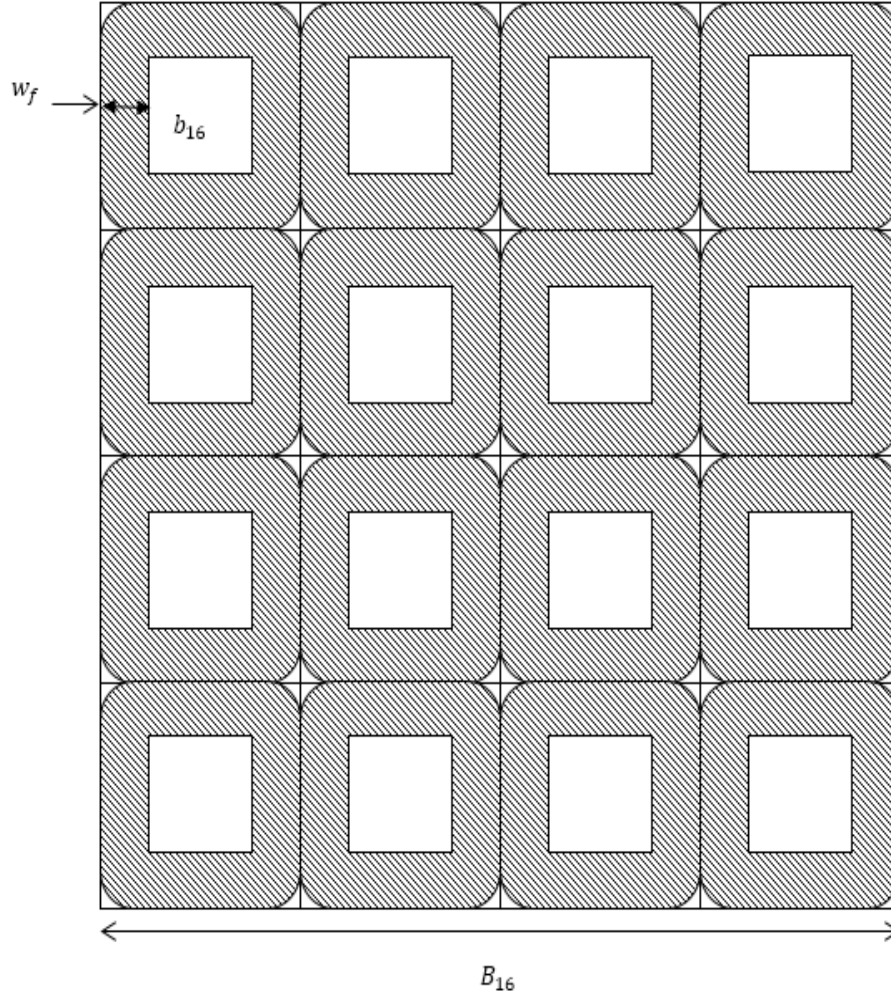


Figure 3.4. Schematic of cross-section of square solid fuel grain with sixteen ports

Let us consider a solid fuel grain with a square cross section and sixteen square ports of side b_{16} each with fuel web thickness w_f . The side of the total fuel grain with sixteen ports is $B_{16} = 4b_{16} + 8w_f$, where B_{16} is the side of the total solid fuel grain. The initial area of the square port is b_{16}^2 and total area of the solid fuel grain including the port is given by $16(b_{16} + 2w_f)^2$

The surface area of the solid fuel with sixteen ports is given by

$$A_{sf16} = 16(b_{16} + 2w_f)^2 - 16b_{16}^2 \quad (3.13)$$

$$A_{sf16} = 16b_{16}^2 + 64b_{16}w_f + 64w_f^2 - 16b_{16}^2$$

$$A_{sf16} = 64w_f(b_{16} + w_f) \quad (3.14)$$

where A_{sf16} is the surface area of solid fuel grain with sixteen ports, the total volume of the solid grain can be obtained by multiplying the surface area with the total length of the grain (not shown in the figure).

$$V_{sf16} = A_{sf16}L_p \quad (3.15)$$

where V_{sf16} is the volume of solid fuel grain with sixteen ports, the total mass required for the desired burn time can be obtained by multiplying volume of the solid fuel with the density of the solid fuel. The total mass m_{f16} is given by

$$m_{f16} = V_{sf16}\rho_f$$

$$m_{f16} = A_{sf16}L_p\rho_f$$

$$m_{f16} = 64w_f(b_{16} + w_f)L_p\rho_f \quad (3.16)$$

The Regression Equation in Non-Dimensional Form

Now we write the equations for square port using non-dimensional variables, we define the following characteristic mass flux rates

$$G_{00} = \frac{\dot{m}_o}{NA_{p0}} = \frac{\dot{m}_o}{Nb^2} \quad (3.17)$$

$$G_{f0} = \frac{G_{o0}}{(OF)_0} \quad (3.18)$$

where G_{00} is the initial oxidizer mass flux rate, $\frac{\dot{m}_o}{N}$ is the oxidizer mass flow rate per port, A_{p0} is the initial port cross-sectional area, b is the initial length of the square port and $(OF)_0$ is the initial oxidizer to fuel ratio. G_{f0} is the initial fuel mass flux rate. We define non-dimensional variables, denoted by bars in the following way

$$w = \bar{w}b, t = \tau\bar{t}, G_o = G_{00}\bar{G}_o, G_f = G_{f0}\bar{G}_f, \tau = \frac{w_f}{\dot{r}_0} \quad (3.19)$$

$$\dot{r}_0 = aL_p^m(G_{00} + G_{f0})^n \quad (3.20)$$

Here τ is a characteristic time defined by $\frac{w_f}{\dot{r}_0}$, where w_f is the final fuel web thickness and \dot{r}_0 is the initial solid fuel regression rate. Upon substituting the new values for different variables in Equations (3.20), and, we obtain

$$\dot{r}_0 = aL_p^m(G_{00} + G_{f0})^n$$

Using $G_{f0} = \frac{G_{00}}{(OF)_0}$ in the above equation, we get

$$\begin{aligned} \dot{r}_0 &= aL_p^m(G_{f0}(OF)_0 + G_{f0})^n \\ \dot{r}_0 &= aL_p^m G_{f0}^n ((OF)_0 + 1)^n \end{aligned} \quad (3.21)$$

As the burn progress the shape of the square is not the same after time t , the corners are transformed into quarter circle which gives the solid grain a new shape and the final

shape is shown in the above figure. Keeping in mind about this change, the new area A_p and new perimeter P_p at any time is given as

$$A_p = b^2 + 4bw + 4\frac{\pi w^2}{4} \quad (3.22)$$

$$P_p = 4b + 2\pi w \quad (3.23)$$

Non-dimensionalizing equations (3.67) and (3.68), we get

$$\begin{aligned} A_p &= b^2 + 4b\bar{w}b + \pi(\bar{w}b)^2 \\ P_p &= 4b + 2\pi\bar{w}b \\ \frac{A_p}{P_p} &= \frac{b(1 + 4\bar{w} + \pi\bar{w}^2)}{4 + 2\pi\bar{w}} \end{aligned} \quad (3.24)$$

Based on the new values of A_p & P_p , new oxidizer and fuel mass fluxes from chapter 2, equations (2.6), (2.14) are defined as

$$G_o = \frac{\dot{m}_o}{NA_p} = \frac{\dot{m}_o}{N(b^2 + 4bw + \pi w^2)} \quad (3.25)$$

$$G_f = G_f(t, x) = \int_0^x \frac{d\dot{m}_f}{A_p(t, \xi)} = \int_0^x \frac{\rho_f \dot{r}(t, \xi) P_p(t, \xi) d\xi}{A_p(t, \xi)} = \frac{\rho_f L_p \dot{r}(t)(4 + 2\pi\bar{w})}{b(1 + 4\bar{w} + \pi\bar{w}^2)}$$

Using regression rate equation for \dot{r} in the above equation we get

$$G_f = a\rho_f L_p^{m+1} (G_o + G_f)^n \frac{(4 + 2\pi\bar{w})}{b(1 + 4\bar{w} + \pi\bar{w}^2)} \quad (3.26)$$

Non-dimensionalizing equations (3.25) and (3.26), we get

$$G_{f0}\bar{G}_f = a\rho_f L_p^{m+1} (G_{o0}\bar{G}_o + G_{f0}\bar{G}_f)^n \frac{(4 + 2\pi\bar{w})}{b(1 + 4\bar{w} + \pi\bar{w}^2)}$$

Using $G_{f0} = \frac{G_{o0}}{(OF)_0}$ in the above equation, we get

$$G_{f0}\bar{G}_f = a\rho_f L_p^{m+1} G_{f0}^n ((OF)_0\bar{G}_o + \bar{G}_f)^n \frac{(4 + 2\pi\bar{w})}{b(1 + 4\bar{w} + \pi\bar{w}^2)} \quad (3.27)$$

But from equation (3.21)

$$aL_p^m G_{f0}^n = \frac{\dot{r}_0}{((OF)_0 + 1)^n} \quad (3.28)$$

Substituting equation (3.28) in equation (3.27)

$$G_{f0} \bar{G}_f = \rho_f \frac{L_p}{b} \frac{\dot{r}_0}{((OF)_0 + 1)^n} ((OF)_0 \bar{G}_o + \bar{G}_f)^n \frac{(4 + 2\pi\bar{w})}{(1 + 4\bar{w} + \pi\bar{w}^2)}$$

$$\bar{G}_f = \left(\frac{L_p}{b}\right) \left(\frac{\dot{r}_0 \rho_f}{G_{f0}}\right) \frac{1}{((OF)_0 + 1)^n} ((OF)_0 \bar{G}_o + \bar{G}_f)^n \frac{(4 + 2\pi\bar{w})}{(1 + 4\bar{w} + \pi\bar{w}^2)} \quad (3.29)$$

For making equation simpler we are rewriting some terms as constants

$$\frac{L_p}{b} = \beta \quad (3.30)$$

$$\delta = \frac{\dot{r}_0 \rho_f}{G_{f0}} = \frac{\dot{r}_0 \rho_f}{\dot{r}_0 \rho_f} \frac{A_{p0}}{P_{p0} L_p} = \frac{A_{p0}}{P_{p0} L_p} = \frac{b^2}{4bL_p} = \frac{b}{4L_p} = \frac{1}{4\beta} \quad (3.31)$$

β is defined as fineness ratio, using equations (3.30) & (3.31), \bar{G}_f can be written as

$$\bar{G}_f = \beta \delta \frac{1}{((OF)_0 + 1)^n} ((OF)_0 \bar{G}_o + \bar{G}_f)^n \frac{(4 + 2\pi\bar{w})}{(1 + 4\bar{w} + \pi\bar{w}^2)} \quad (3.32)$$

$$\bar{G}_f = (0.25) \frac{1}{((OF)_0 + 1)^n} ((OF)_0 \bar{G}_o + \bar{G}_f)^n \frac{(4 + 2\pi\bar{w})}{(1 + 4\bar{w} + \pi\bar{w}^2)} \quad (3.33)$$

Consider regression rate equation

$$\dot{r} = \frac{dw}{dt} = aL_p^m (G_f + G_o)^n \quad (3.34)$$

$$\frac{b}{\tau} \frac{d\bar{w}}{d\bar{t}} = aL_p^m (G_{o0} \bar{G}_o + G_{f0} \bar{G}_f)^n$$

$$\frac{d\bar{w}}{d\bar{t}} = \frac{\tau}{b} a L_p^m G_{f0}^n ((OF)_0 \bar{G}_o + \bar{G}_f)^n$$

Substituting equation (3.28) in the above equation, and using $\tau = \frac{w_f}{\dot{r}_0}$

$$\begin{aligned} \frac{d\bar{w}}{d\bar{t}} &= \frac{w_f}{\dot{r}_0} \frac{1}{b} \frac{\dot{r}_0}{((OF)_0 + 1)^n} ((OF)_0 \bar{G}_o + \bar{G}_f)^n \\ \frac{d\bar{w}}{d\bar{t}} &= \frac{w_f}{b} \frac{1}{((OF)_0 + 1)^n} ((OF)_0 \bar{G}_o + \bar{G}_f)^n \end{aligned} \quad (3.35)$$

This initial value of \bar{w} becomes the initial condition for the ODE

$$\bar{w}(0) = 0$$

Now, let us find equation for \bar{G}_o with respect to new values

$$\begin{aligned} \bar{G}_o &= \frac{G_o}{G_{00}} \\ \bar{G}_o &= \frac{\frac{\dot{m}_o}{N(b^2 + 4bw + \pi w^2)}}{\frac{\dot{m}_o}{Nb^2}} \\ \bar{G}_o &= \frac{b^2}{(b^2 + 4bw + \pi w^2)} \end{aligned}$$

Non-dimensionalizing above equation with $w = \bar{w}b$, we get

$$\bar{G}_o = \frac{1}{(1 + 4\bar{w} + \pi\bar{w}^2)} \quad (3.36)$$

Numerical Results

Having determined the non-dimensional parameters, we can solve the non-dimensional internal ballistics equations numerically using a standard ODE solver

$$\frac{d\bar{w}}{d\bar{t}} = \frac{w_f}{b} \frac{1}{((OF)_0 + 1)^n} ((OF)_0 \frac{1}{(1 + 4\bar{w} + \pi\bar{w}^2)} + \bar{G}_f)^n \quad (3.35)$$

$$\bar{G}_f = (0.25) \frac{1}{((OF)_0 + 1)^n} \left((OF)_0 \frac{1}{(1 + 4\bar{w} + \pi\bar{w}^2)} + \bar{G}_f \right)^n \frac{(4 + 2\pi\bar{w})}{(1 + 4\bar{w} + \pi\bar{w}^2)} \quad (3.33)$$

with initial condition $\bar{w}(0) = 0$ and $(OF)_0 = 2$. The initial Oxidizer to fuel ratio is chosen as 2 since there is a OF shift along the burn time and this is the minimum value for the choice of propellant. Initial guess for w_f is taken to be 6 cm.

We now have the first order differential equation supported by the algebraic function. This first order ODE is integrated from $t = 0$ to 60 seconds, which is then solved for getting the values of $G_f(t), G_o(t), \dot{r}(t), w(t), OF(t)$. Based on these values the remaining flow properties are calculated.

Results & Discussion for a Single Square Port

$$m_f = volume * Density$$

$$m_f = 4Nw_f(b_1 + w_f)L_{p1}\rho_f$$

$$192 = 4 * 0.0535(b_1 + 0.0535)L_{p1}1000 \quad (3.37)$$

By considering the same amount of solid fuel and same amount of web thickness as for the single port, see equation (2.49), the above equation is iterated to produce the same amount of burn time by varying the number of ports. The final values for the above equation are b_1 is 0.183 and L_{p1} is 4m. The results obtained for this case are presented below from Fig. 3.5 to Fig. 3.9.

Port length x(m)	t = 0.1 sec		t = 60 sec	
	\dot{r} (cm/sec)	O/F	\dot{r} (cm/sec)	O/F
4	0.135	2.007	0.064	2.903

Table 3.1. Results obtained by the proposed procedure for a single square port

The Oxidizer mass flux for the single port is beginning from $237 \text{ kg/m}^2\text{s}$ and reaching a value of $97 \text{ kg/m}^2\text{s}$. The fuel flux is varying from $118 \text{ kg/m}^2\text{s}$ to $33 \text{ kg/m}^2\text{s}$. However the thrust produced by this fuel grain is equal to 34 KN and the chamber pressure is equal to 3.45 MPa which are equal to that of single port. The specific impulse increases from 293 to 296 sec and the exit velocity varies from 2536 (m/sec) to 2523 (m/sec). The solid fuel grain of length 4 meters is considered with a port side of 0.183 meters. Density of 1000 kg/m^3 , Initial chamber pressure is 3.45 MPa, Exit Pressure is 13800 Pa, $a = 2.066\text{e-}5$, $n = 0.75$, $m = -0.15$, $\dot{m}_o = 7.95 \text{ kg/s}$, $(OF)_0 = 2$, $\varepsilon = 70$.

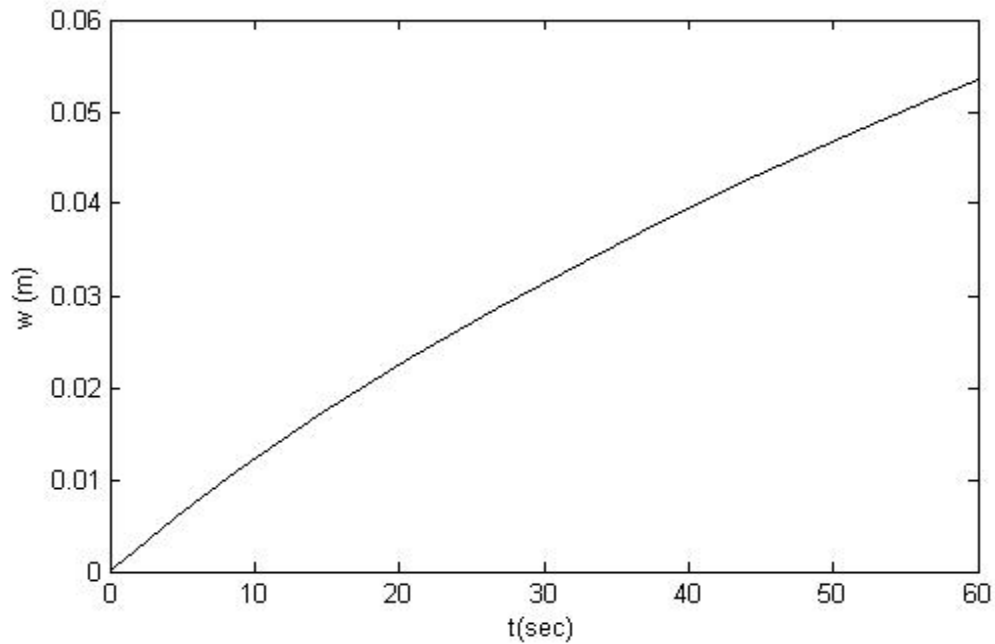


Figure. 3.5. Web thickness vs Burn time

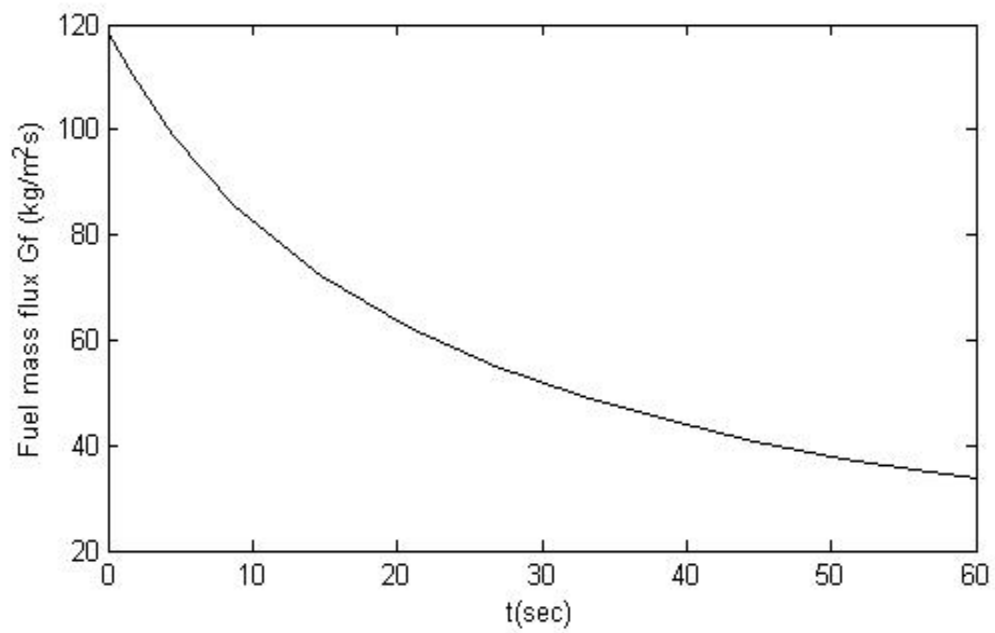
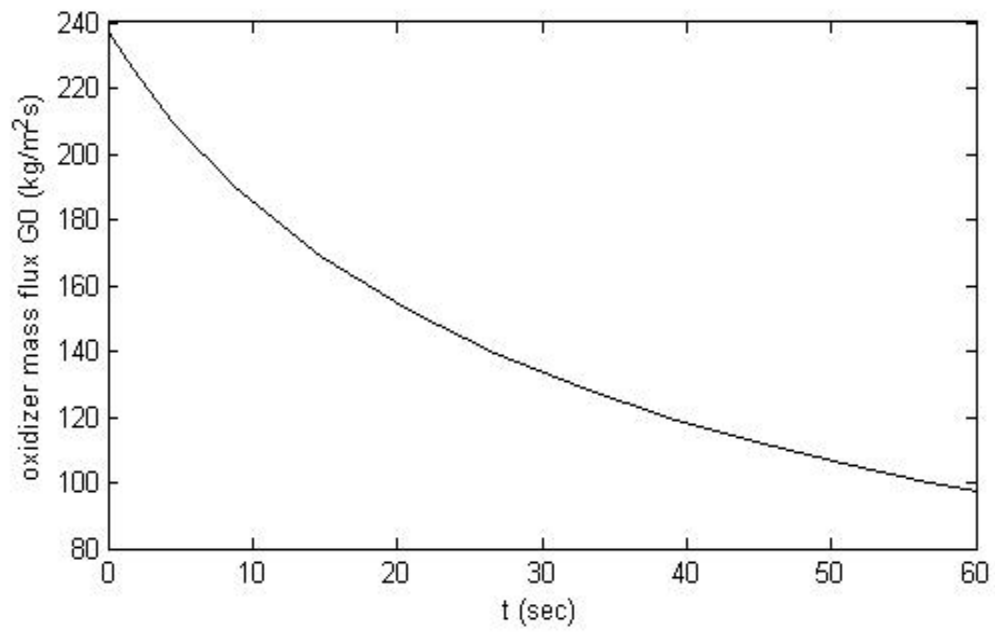


Figure. 3.6. Oxidizer mass flux and fuel mass flux vs Burn time

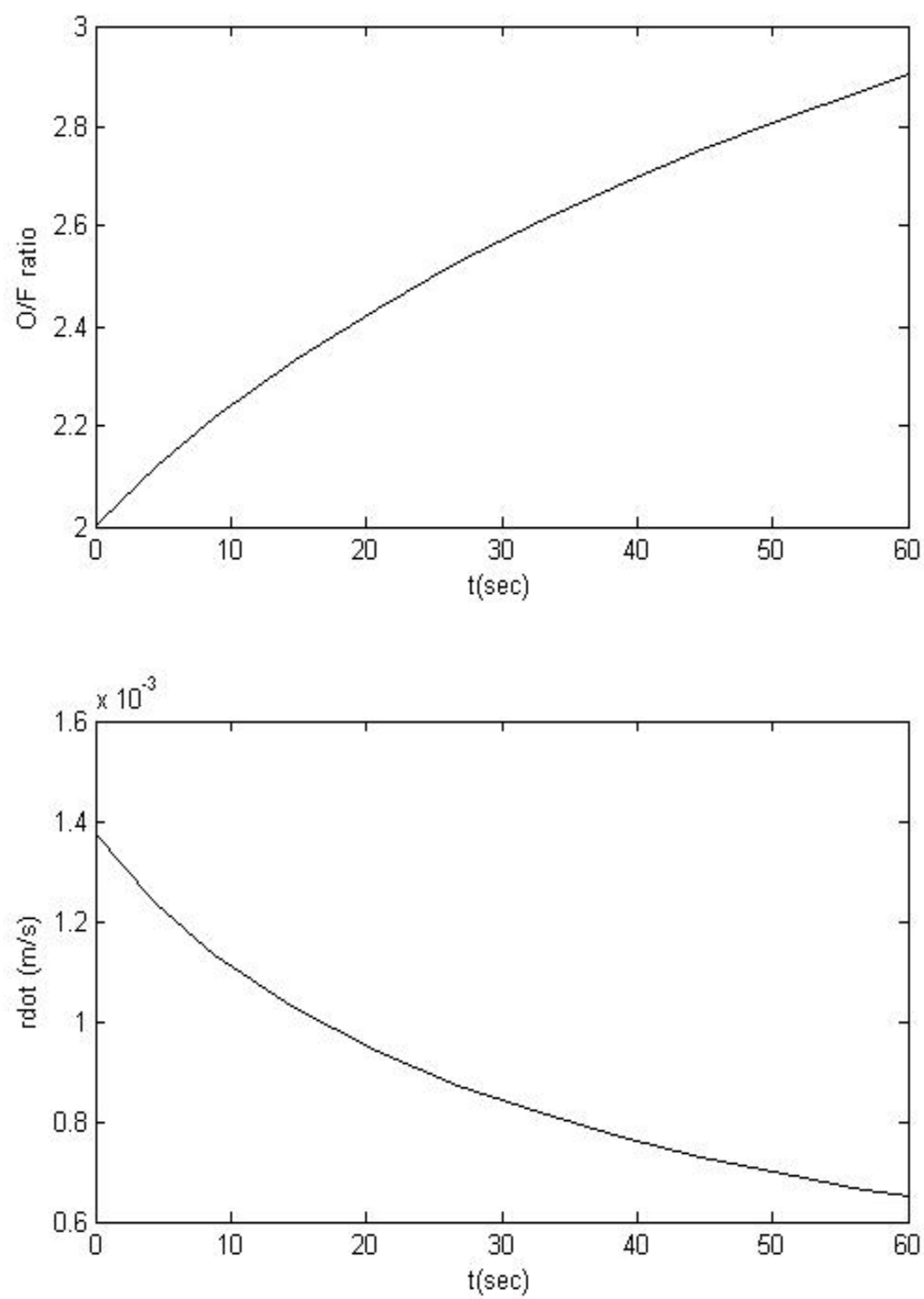


Figure.3.7. (O/F) ratio and Regression rate vs Burn time

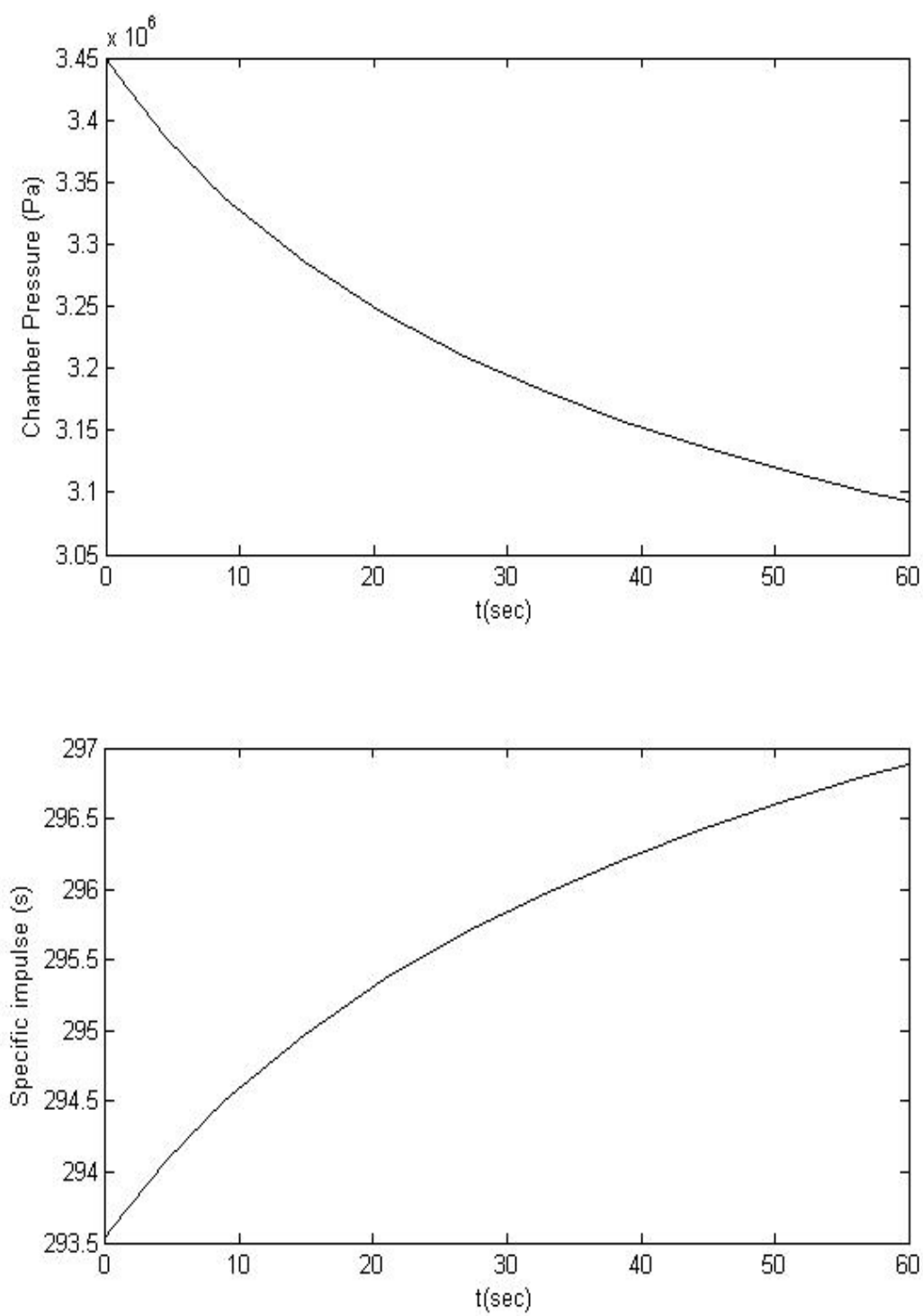


Figure.3.8. Chamber Pressure and Specific Impulse vs Burn time

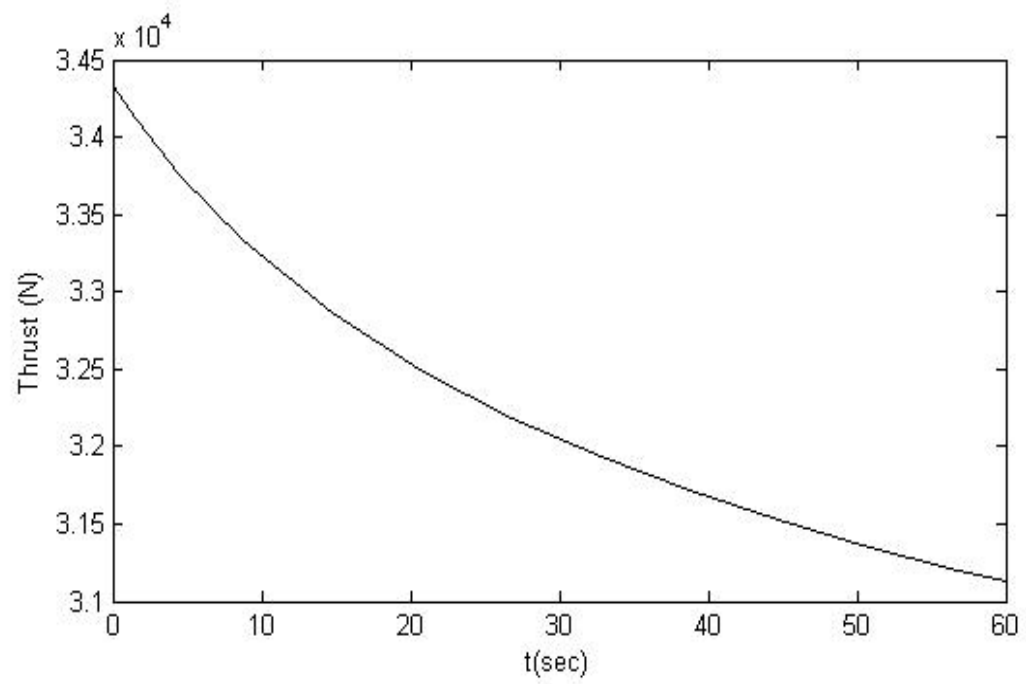
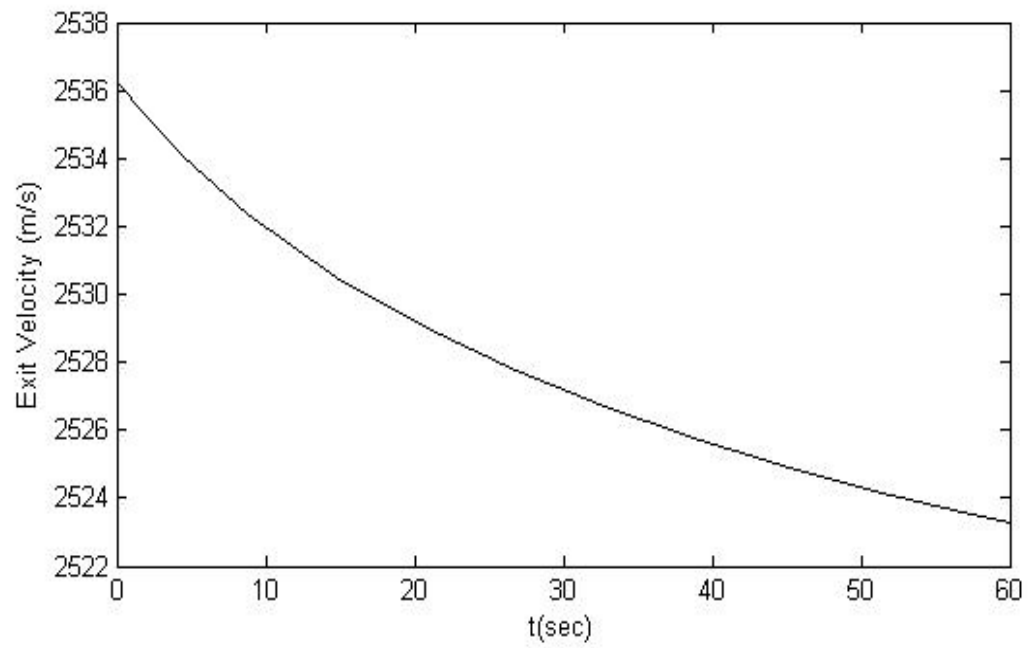


Figure.3.9. Exit velocity and the Thrust vs Burn time

Results & Discussion for Four square ports

$$m_f = \text{volume} * \text{Density}$$

$$m_f = 4Nw_f(b_4 + w_f)L_{p4}\rho_f$$

$$192 = 16 * 0.0535(b_4 + 0.0535)L_{p4}1000 \quad (3.38)$$

By considering the same amount of solid fuel and same amount of web thickness as for the single port, see equation (2.49), the above equation is iterated to produce the same amount of burn time by varying the number of ports. The final values for the above equation are b_4 is 0.07 and L_{p4} is 2.01m. The results obtained for this case are presented below from Fig 3.10 to Fig 3.13.

Port length x(m)	t = 0.1 sec		t = 60 sec	
	\dot{r} (cm/sec)	O/F	\dot{r} (cm/sec)	O/F
2.01	0.23	2.007	0.0526	2.903

Table 3.2. Results obtained by the proposed procedure for four square ports

The Oxidizer mass flux through each of the four ports ranges from $405 \text{ kg/m}^2\text{s}$ to $68 \text{ kg/m}^2\text{s}$. The fuel flux is varying from $202 \text{ kg/m}^2\text{s}$ to $17.5 \text{ kg/m}^2\text{s}$. However the thrust produced by this fuel grain is equal to 34 KN and the chamber pressure is equal to 3.43 MPa which are almost equal to those from a single port. The specific impulse increases from 293 to 300 sec and the exit velocity varies from 2536 (m/sec) to 2514 (m/sec).

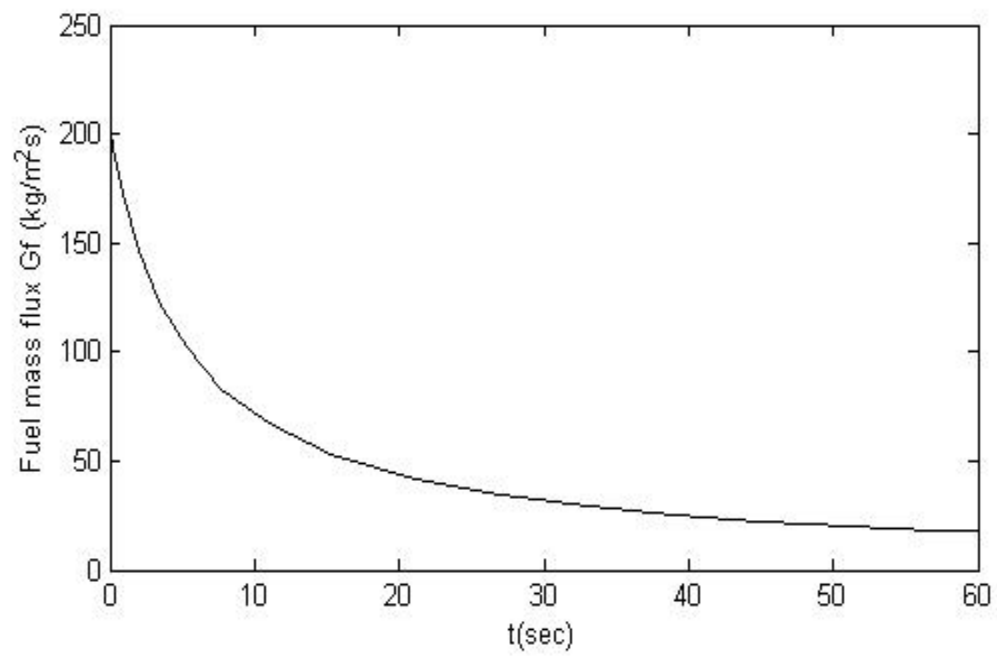
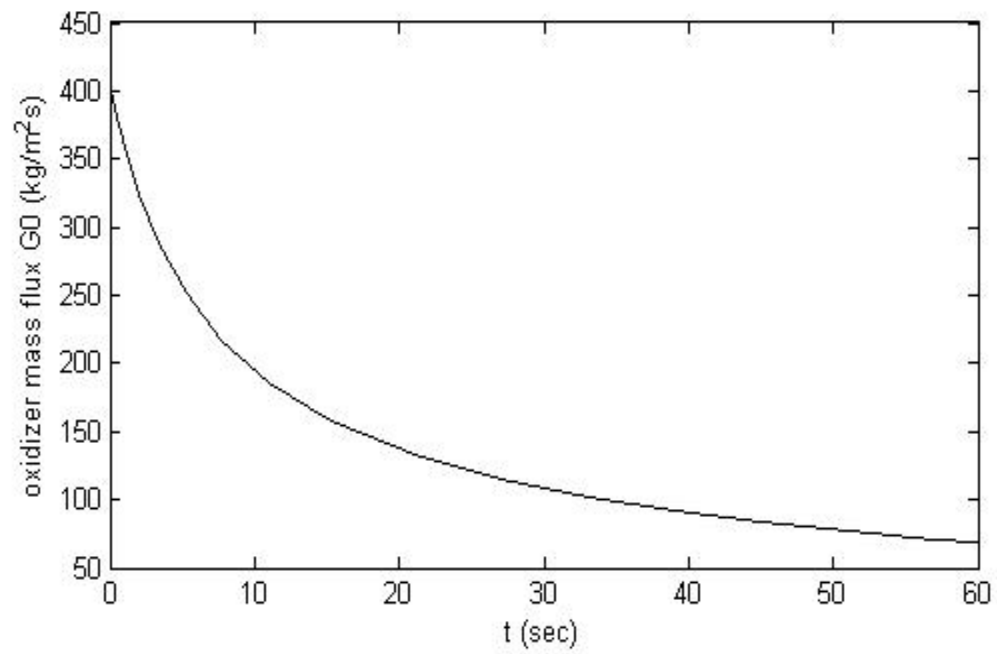


Figure. 3.10. Oxidizer mass flux and fuel mass flux vs Burn time

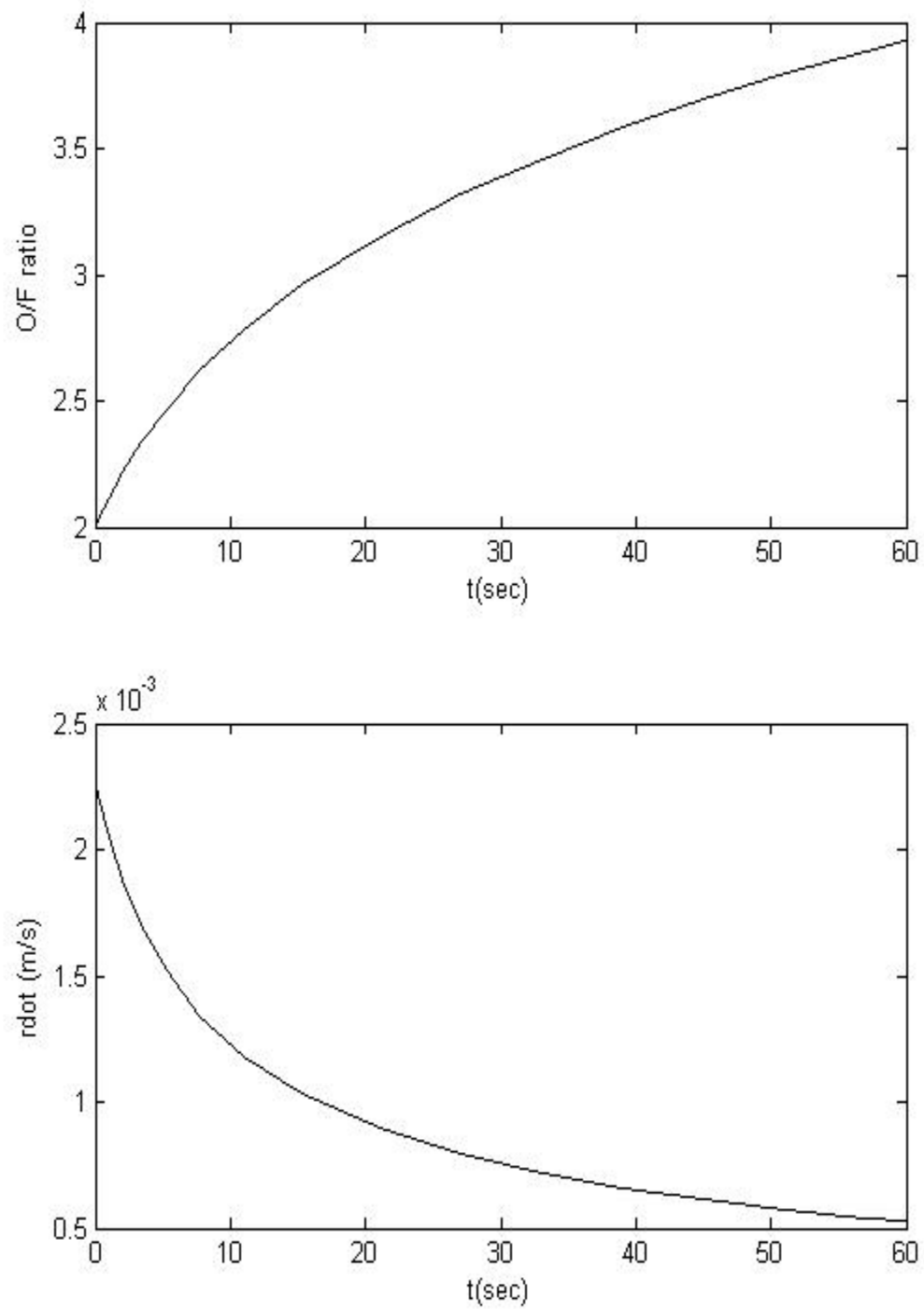


Figure. 3.11. (OF) ratio and regression rate vs Burn time

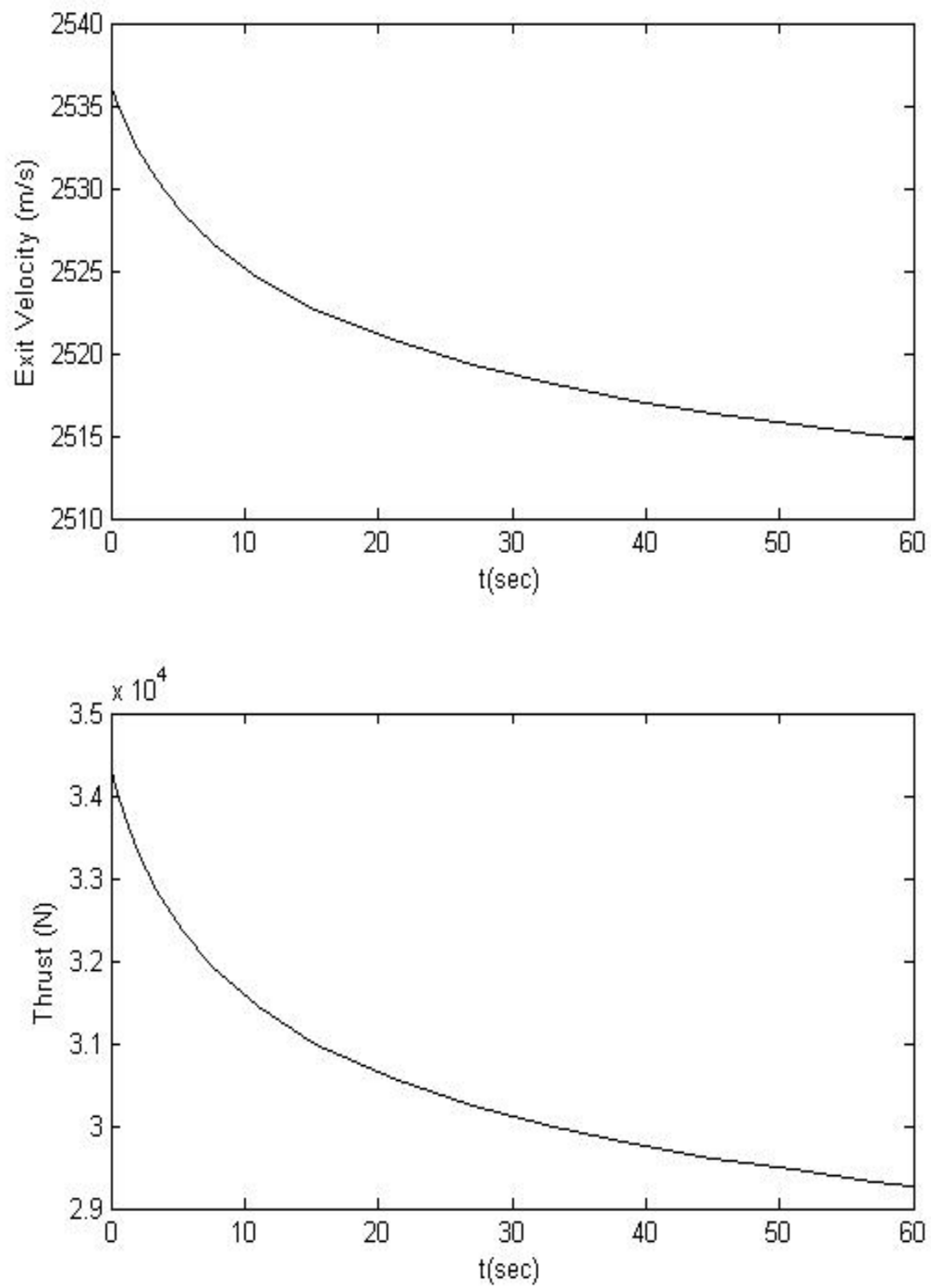


Figure. 3.12. Exit Velocity and the Thrust vs Burn time

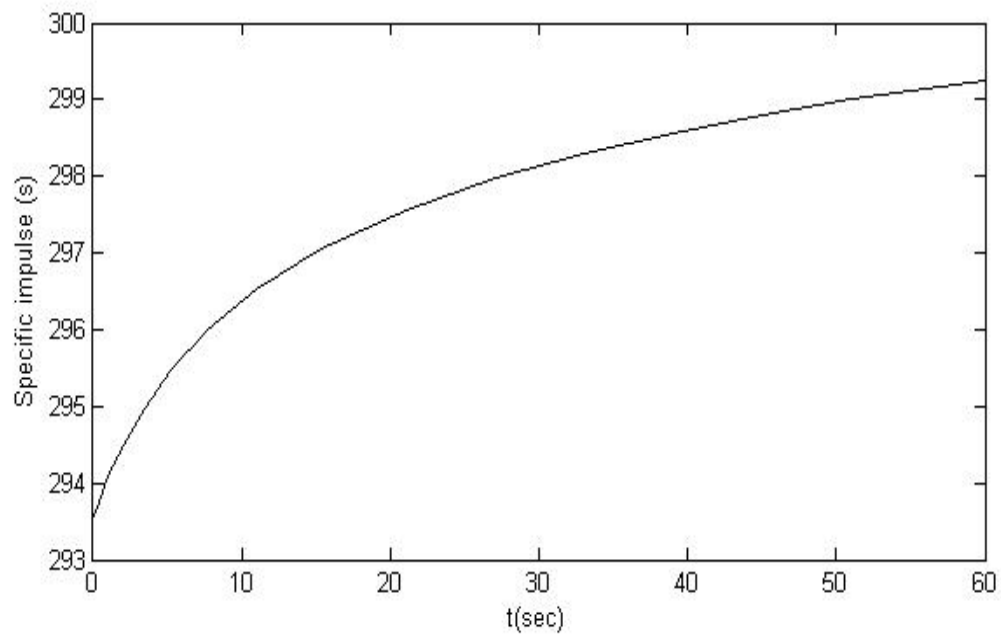
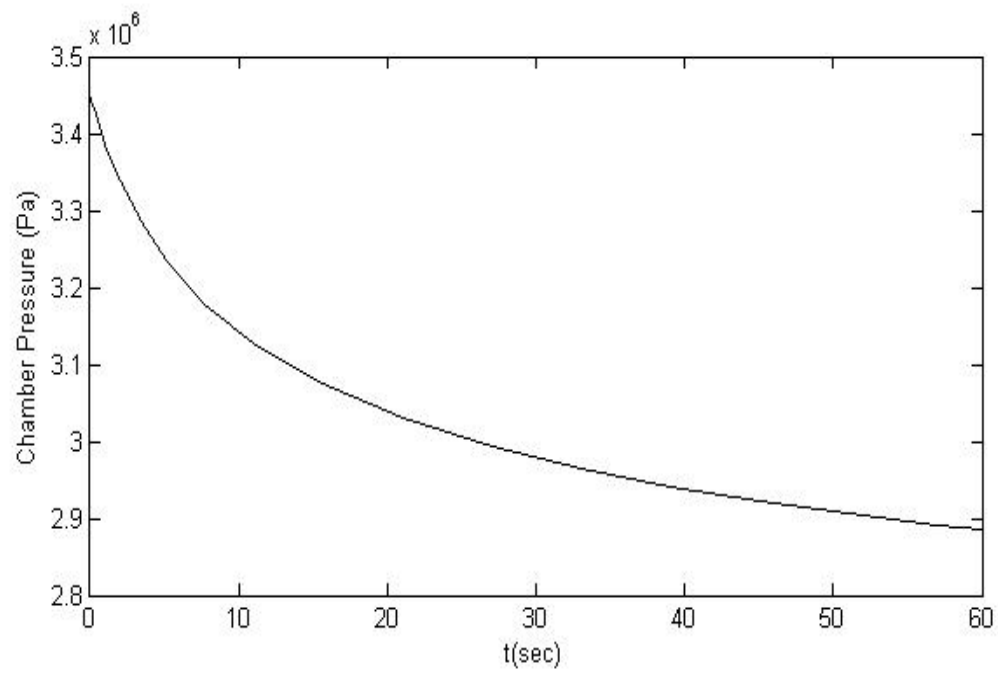


Figure. 3.13. Chamber Pressure and the Specific Impulse vs Burn time

Results for Volumetric Efficiency of the Square ports

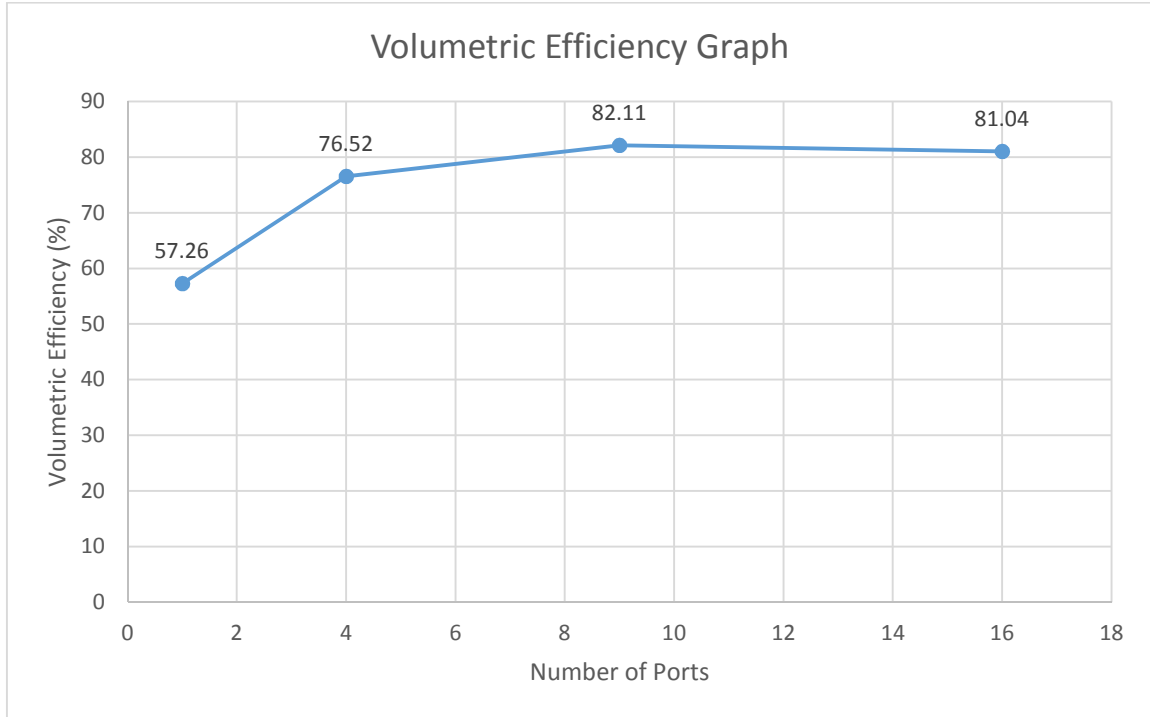


Figure. 3.14. The Schematic of volumetric efficiency vs the Number of Ports

The volumetric efficiency graph for the square port starts from 57.26 % for the single port and reaches maximum value of 82.11 % for nine ports and remains almost constant after that for sixteen ports.

Chapter IV

Variation of the Flow Properties along the Axial Direction

Introduction

This chapter deals with analytical modeling of the basic flow field in hybrid rockets with wall injection. In contrast to the preceding chapters, which neglect the effect of axial length in the regression rate equation, this section considers the variation of properties and their effects along the axial length.

We focus on the conventional flow configuration assuming a full length, internal burning cylinder. The solution is sought in a non-reactive, non-swirling, compressible, and viscous with headwall injection.

Modeling of Generalized One-Dimensional Flow

Despite the relative complexity of the fluid structures that lie directly adjacent to the fuel surface, the trajectory followed by gases ejected into a hybrid chamber can be assumed to be normal to the surface. The interactions within the flame zone are ignored. The one dimensional approximations are assumed for the viscous flow in a rocket chamber with regressing walls. A closed form analytical approximation can be used to describe the gas motion corresponding to this idealized representation of a hybrid engine. The technique we choose relies on a conventional similarity approach, this will be employed in conjunction with Euler's equations. This will result in a steady, compressible mean flow solution for a full-length circular port hybrid engine. Until more refined models become available, these approximations will provide simplistic idealizations owing to the following reasons and limitations:

1. The burning rate of hybrid rocket is very sensitive to the flow field in the chamber. Hence, many standard assumptions, such as uniform burning rate, which can be justified in SRM's become less suitable in hybrids. The regression rate is strongly controlled by the pyrolyzing fluid and flow conditions; it is prescribed by complex fluid dynamics and interactions with heat transfer from the hot core to the solid fuel surface. The heat flux is related, in turn, to turbulent conditions, multiphase effects, and radiation. These factors are not considered here.
2. The real challenge of hybrid propulsion is in the mixing and the vaporization of the two streams. However, in seeking a basic description, no attempts will be made to capture the mixing patterns of oxidizer and fuel or to model the vaporization of the two streams.

Consider the flow in a full-length cylindrical hybrid motor between two sections an infinitesimal distance dx apart (Fig 4.1). In this element of duct length gas is injected into the stream at the mass rate of flow dw_g , into the stream. The various physical equations and definitions will be expressed in logarithmic differential form. It will be seen that this procedure allows easy separation of the physical variables.

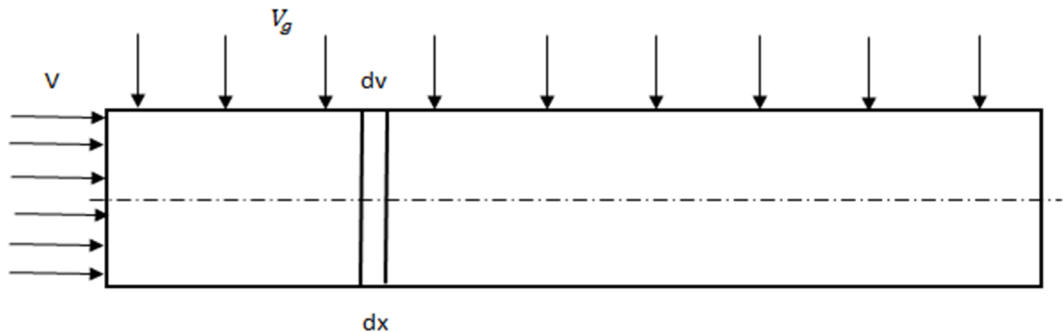


Figure 4.1. Schematic of the combustion hybrid chamber

Equation of State: The Pressure density temperature relation [Ascher, 1953] is

$$P = \rho RT \quad (4.1)$$

where P is the pressure, ρ is the density, R is the Universal Gas constant and T is the temperature in the combustion chamber.

Taking logarithms on both sides for the equation 4.1, we get

$$\log P = \log \rho + \log R + \log T \quad (4.2)$$

Then, taking the differential of each side for equation 4.2, we have

$$\begin{aligned} \frac{dP}{P} &= \frac{d\rho}{\rho} + \frac{dT}{T} \\ \frac{d\rho}{\rho} + \frac{dT}{T} - \frac{dP}{P} &= 0 \end{aligned} \quad (4.3)$$

Sound Velocity: The expression for the sound velocity [Ascher, 1953] in a semi-perfect gas is

$$c^2 = \gamma RT \quad (4.4)$$

where c is the velocity of the sound, R is the Universal Gas constant, γ is the perfect gas constant, T is the temperature of the flow

Taking logarithms on both sides for the equation 4.4, we get

$$2 \log c = \log \gamma + \log R + \log T$$

Then taking differential of equation 4.5 each side, we have

$$\frac{dc}{c} = \frac{1}{2} \frac{dT}{T} \quad (4.5)$$

Definition of Mach number: From the definition of the Mach number [Ascher, 1953] and equation 4.4, we find that

$$M^2 = V^2/c^2 = V^2/\gamma RT \quad (4.6)$$

where M is the Mac number of the flow, V is the velocity of the flow and c is the local velocity of the sound

Taking logarithms on both sides for the equation 4.6, we get

$$\log M^2 = 2\log V - \log \gamma - \log R - \log T$$

Then taking differential of equation 4.6 each side, we have

$$\frac{dM^2}{M^2} = 2 \frac{dV}{V} - \frac{dT}{T} \quad (4.7)$$

Equation of Continuity: Fig. 4.1 shows several methods by which the injected gas is brought into the main stream. Also shown are the corresponding control surfaces employed for the purposes of analysis. The injected gas flow dw_g is assumed to be injected continuously along the length of the grain, i.e., dw_g/dx is assumed to be finite or zero. This may be thought of as a simple model of real injection processes. It is assumed further that the injected streams are mixed perfectly with the main gas stream.

The mass flow [Ascher, 1953] of the main gas stream may be expressed as

$$w = \rho AV \quad (4.8)$$

where w is the mass flow rate of the flow, A is the area of the port, ρ is the density of the flow, V is the velocity of the flow Differentiating equation 4.8 on both sides, to get

$$dw = d(\rho AV)$$

$$dw = AVd\rho + \rho VdA + \rho AdV \quad (4.9)$$

Dividing equation 4.9 with equation 4.8 to obtain a relation

$$\frac{dw}{w} = \frac{d\rho}{\rho} + \frac{dV}{V} + \frac{dA}{A}$$

In this expression 'dw' denotes the total increase of mass flow in the main stream and includes evaporated gas. The equation of continuity is, therefore,

$$dw = dw_g$$

$$\frac{dw_g}{w} = \frac{d\rho}{\rho} + \frac{dV}{V} + \frac{dA}{A} \quad (4.10)$$

Energy Equation: Only the liquid crossing the control-surface boundary and evaporating within the control surface is taken into account in evaluating the flux of enthalpy. Changes in temperature of the gas traveling along with the stream are taken to be the result of external heat change to or from the main stream. As the flow thoroughly mixed with the main stream, pass out of the control surface, they are assumed to be at the temperature of the latter. Assuming no heat is added to the stream by conduction or radiation and no net external work is delivered to outside bodies. The heat change is purely by combustion. The energy equation [Ascher, 1953] for the flow through the control surface may be written, assuming gravity effects to be negligible, as

$$dH = C_p dT + d\left(\frac{V^2}{2}\right) \quad (4.11)$$

Considering h_{gt} as the enthalpy of the injected gas dw_g at temperature T_c and h_g as the enthalpy at the temperature T in the control volume respectively, dh_{pr} as the enthalpy increase at the temperature T and pressure P for a change from products to reactants, is

positive for exothermic reactions. V_g is the velocity of the injected gas. The energy term dH is defined as

$$dH = dh_{pr} - (h_{gT} - h_g - \frac{V_g^2}{2} + \frac{V^2}{2}) \frac{dw_g}{w} \quad (4.12)$$

Dividing equation (4.11) by $C_p T$, where C_p is specific heat at constant pressure, we obtain

$$\frac{dH}{C_p T} = \frac{dT}{T} + \frac{1}{C_p T} \frac{dV^2}{2} \quad (4.13)$$

Using definition of C_p

$$C_p = \frac{\gamma R}{\gamma - 1} \quad (4.14)$$

Multiplying by 'T' on both sides

$$C_p T = \frac{\gamma R T}{\gamma - 1} \quad (4.15)$$

From definition of Mac Number

$$M^2 = \frac{V^2}{c^2} \quad (4.16)$$

Where 'c' is sound velocity which is given by

$$c^2 = \gamma R T \quad (4.17)$$

$$\gamma R T = \frac{V^2}{M^2} \quad (4.18)$$

Substituting equation (4.18) in equation (4.15) to get

$$C_p T = \frac{1}{\gamma - 1} \frac{V^2}{M^2} \quad (4.19)$$

$$\frac{dH}{C_p T} = \frac{dT}{T} + \frac{\gamma - 1}{2} M^2 \frac{dV^2}{V^2} \quad (4.20)$$

Momentum Equation: The net force acting on the material within the control surface is equal to the increase of momentum flux of the streams flowing through the control surface. Consider forces in the direction of flow acting on the control surface in Fig. 4.1. The momentum equation [Ascher, 1953] may be written using dP as the change in the pressure, dV as the change in the velocity, f as the frictional coefficient, D as the mean hydraulic diameter. In the model there are no body forces considered.

$$\frac{dP}{P} + \frac{\gamma M^2}{2} \frac{dV^2}{V^2} + 2\gamma M^2 f \frac{dx}{D} + \gamma M^2 \frac{dw_g}{w} = 0 \quad (4.21)$$

Working Equations and Tables of Influence Coefficients

Six independent relations between the differential parameters have been set forth, namely, EQs. (4.3), (4.5), (4.7), (4.10), (4.20) and (4.21).

$$\frac{d\rho}{\rho} + \frac{dT}{T} - \frac{dP}{P} = 0 \quad (4.3)$$

$$\frac{dc}{c} = \frac{1}{2} \frac{dT}{T} \quad (4.5)$$

$$\frac{dM^2}{M^2} = 2 \frac{dV}{V} - \frac{dT}{T} \quad (4.7)$$

$$\frac{dw_g}{w} = \frac{d\rho}{\rho} + \frac{dV}{V} + \frac{dA}{A} \quad (4.10)$$

$$\frac{dH}{C_p T} = \frac{dT}{T} + \frac{\gamma - 1}{2} M^2 \frac{dV^2}{V^2} \quad (4.20)$$

$$\frac{dP}{P} + \frac{\gamma M^2}{2} \frac{dV^2}{V^2} + 2\gamma M^2 f \frac{dx}{D} + \gamma M^2 \frac{dw_g}{w} = 0 \quad (4.21)$$

Using equation (4.20)

$$\frac{dH}{C_p T} = \frac{dT}{T} + (\gamma - 1)M^2 \frac{dV}{dV} \quad (4.22)$$

Using equation (4.3) & (4.10)

$$\frac{dV}{V} + \frac{dP}{P} - \frac{dT}{T} = \frac{dw_g}{w} - \frac{dA}{A} \quad (4.23)$$

Now adding equations (4.22) & (4.23) to get

$$\frac{dH}{C_p T} + \frac{dw_g}{w} - \frac{dA}{A} = \frac{dV}{V} (1 + (\gamma - 1)M^2) + \frac{dP}{P} \quad (4.24)$$

Subtracting equation (4.21) and (4.24) to get

$$\frac{dV}{V} = \frac{-1}{1 - M^2} \frac{dA}{A} + \frac{1 + \gamma M^2}{1 - M^2} \frac{dw_g}{w} + \frac{1}{1 - M^2} \frac{dH}{C_p T} + \frac{\gamma M^2}{2(1 - M^2)} 4f \frac{dx}{D} \quad (4.25)$$

Substituting equation (4.25) in equation (4.20) to get

$$\begin{aligned} \frac{dT}{T} = & \frac{(\gamma - 1)M^2}{1 - M^2} \frac{dA}{A} - \frac{(\gamma - 1)M^2(1 + \gamma M^2)}{1 - M^2} \frac{dw_g}{w} + \frac{dH}{C_p T} \frac{1 - \gamma M^2}{1 - M^2} \\ & - \frac{\gamma(\gamma - 1)M^4}{2(1 - M^2)} 4f \frac{dx}{D} \end{aligned} \quad (4.26)$$

Plugging values of $\frac{dV}{V}$, $\frac{dT}{T}$ in equation (4.7) to get

$$\begin{aligned} \frac{dM^2}{M^2} = & - \frac{2(1 + \frac{\gamma - 1}{2} M^2)}{1 - M^2} \frac{dA}{A} + \frac{1 + \gamma M^2}{1 - M^2} \frac{dH}{C_p T} + \frac{\gamma M^2(1 + \frac{\gamma - 1}{2} M^2)}{1 - M^2} 4f \frac{dx}{D} \\ & + \frac{2(1 + \gamma M^2)(1 + \frac{\gamma - 1}{2} M^2)}{1 - M^2} \frac{dw_g}{w} \end{aligned} \quad (4.27)$$

From equation (4.5)

$$\begin{aligned} \frac{dc}{c} = & \frac{(\gamma - 1)M^2}{2(1 - M^2)} \frac{dA}{A} + \frac{1 - \gamma M^2}{2(1 - M^2)} \frac{dH}{C_p T} - \frac{\gamma(\gamma - 1)M^4}{4(1 - M^2)} 4f \frac{dx}{D} \\ & + \frac{(\gamma - 1)M^2(1 + \gamma M^2)}{2(1 - M^2)} \frac{dw_g}{w} \end{aligned} \quad (4.28)$$

Substituting $\frac{dv}{v}$ in equation (4.10)

$$\frac{d\rho}{\rho} = \frac{dA}{A} \left(\frac{M^2}{1 - M^2} \right) - \frac{1}{1 - M^2} \frac{dH}{C_p T} - \frac{\gamma M^2}{2(1 - M^2)} 4f \frac{dx}{D} - \frac{dw_g}{w} \frac{(1 + \gamma)M^2}{1 - M^2} \quad (4.29)$$

Substituting $\frac{d\rho}{\rho}, \frac{dT}{T}$ values in equation (4.3)

$$\begin{aligned} \frac{dP}{P} = & \frac{\gamma M^2}{1 - M^2} \frac{dA}{A} - \frac{\gamma M^2}{1 - M^2} \frac{dH}{C_p T} - \frac{\gamma M^2(1 + (\gamma - 1)M^2)}{2(1 - M^2)} 4f \frac{dx}{D} \\ & - \frac{2\gamma M^2 \left(1 + \frac{(\gamma - 1)M^2}{2} \right)}{1 - M^2} \frac{dw_g}{w} \end{aligned} \quad (4.30)$$

The variation of flow properties along the axial length can be obtained by non-dimensionalizing the above equations with respect to axial length $dx = Ld\bar{x}$. As there are ten differential variables, four may be chosen as independent variables and six as dependent variables. For the independent variables we choose those most easily controlled in practice, as identified below. The usual methods of solving a system of simultaneous, linear, algebraic equations may be employed for obtaining each dependent variable in terms of the six dependent parameters.

$$\frac{1}{V} \frac{dV}{d\bar{x}} = \frac{-1}{1 - M^2} \frac{1}{A} \frac{dA}{d\bar{x}} + \frac{1 + \gamma M^2}{1 - M^2} \frac{1}{w} \frac{dw_g}{d\bar{x}} + \frac{1}{1 - M^2} \frac{1}{C_p T} \frac{dH}{d\bar{x}} + \frac{\gamma M^2}{2(1 - M^2)} 4f \frac{L}{D} \quad (4.31)$$

$$\frac{1}{T} \frac{dT}{d\bar{x}} = \frac{(\gamma - 1)M^2}{1 - M^2} \frac{1}{A} \frac{dA}{d\bar{x}} - \frac{(\gamma - 1)M^2(1 + \gamma M^2)}{1 - M^2} \frac{1}{w} \frac{dw_g}{d\bar{x}} + \frac{1}{C_p T} \frac{1 - \gamma M^2}{1 - M^2} \frac{dH}{d\bar{x}} \quad (4.32)$$

$$- \frac{\gamma(\gamma - 1)M^4}{2(1 - M^2)} 4f \frac{L}{D}$$

$$\begin{aligned} \frac{1}{M^2} \frac{dM^2}{d\bar{x}} = & -\frac{2(1 + \frac{\gamma-1}{2}M^2)}{1-M^2} \frac{1}{A} \frac{dA}{d\bar{x}} + \frac{1+\gamma M^2}{1-M^2} \frac{1}{C_p T} \frac{dH}{d\bar{x}} \\ & + \frac{\gamma M^2(1 + \frac{\gamma-1}{2}M^2)}{1-M^2} 4f \frac{L}{D} + \frac{2(1+\gamma M^2)(1 + \frac{\gamma-1}{2}M^2)}{1-M^2} \frac{1}{w} \frac{dw_g}{d\bar{x}} \end{aligned} \quad (4.33)$$

$$\begin{aligned} \frac{1}{c} \frac{dc}{d\bar{x}} = & \frac{(\gamma-1)M^2}{2(1-M^2)} \frac{1}{A} \frac{dA}{d\bar{x}} + \frac{1-\gamma M^2}{2(1-M^2)} \frac{1}{C_p T} \frac{dH}{d\bar{x}} - \frac{\gamma(\gamma-1)M^4}{4(1-M^2)} 4f \frac{L}{D} \\ & + \frac{(\gamma-1)M^2(1+\gamma M^2)}{2(1-M^2)} \frac{1}{w} \frac{dw_g}{d\bar{x}} \end{aligned} \quad (4.34)$$

$$\begin{aligned} \frac{1}{\rho} \frac{d\rho}{d\bar{x}} = & \frac{1}{A} \frac{dA}{d\bar{x}} \left(\frac{M^2}{1-M^2} \right) - \frac{1}{1-M^2} \frac{1}{C_p T} \frac{dH}{d\bar{x}} - \frac{\gamma M^2}{2(1-M^2)} 4f \frac{L}{D} \\ & - \frac{1}{w} \frac{dw_g}{d\bar{x}} \frac{(1+\gamma)M^2}{1-M^2} \end{aligned} \quad (4.35)$$

$$\begin{aligned} \frac{1}{P} \frac{dP}{d\bar{x}} = & \frac{\gamma M^2}{1-M^2} \frac{1}{A} \frac{dA}{d\bar{x}} - \frac{\gamma M^2}{1-M^2} \frac{1}{C_p T} \frac{dH}{d\bar{x}} - \frac{\gamma M^2(1 + (\gamma-1)M^2)}{2(1-M^2)} 4f \frac{L}{D} \\ & - \frac{2\gamma M^2 \left(1 + \frac{(\gamma-1)M^2}{2} \right)}{1-M^2} \frac{1}{w} \frac{dw_g}{d\bar{x}} \end{aligned} \quad (4.36)$$

Influence Coefficients: We shall call the coefficients of the independent variables as influence coefficients, since they indicate the influence of each independent variable on each of the dependent parameters. They are defined for the above model as

By definition of the oxidizer flux,

$$G_o = \frac{\dot{m}_o}{NA_p}$$

By definition of the fuel flux for circular port,

$$G_f = 4\rho_s \int_0^x \frac{\dot{r}}{D_0} d\xi \quad (4.37)$$

Where regression rate \dot{r} is defined as

$$\dot{r} = ax^m(G_0 + G_f)^n \quad (4.38)$$

Introduce a new variable $q(x)$ where we use ξ instead of x as the integration coordinate

$$q(x) = \int_0^x \frac{\dot{r}}{D_0} d\xi \quad (4.39)$$

Then the Fuel flux becomes

$$G_f = 4\rho_s q(x) \quad (4.40)$$

$$\frac{dq}{dx} = \frac{\dot{r}}{D_0} \quad (4.41)$$

Now, non dimensionalizing the equation with respect to its length L_p

$$x = L_p \bar{x}$$

$$\frac{dq}{d\bar{x}} = L_p \frac{\dot{r}}{D_0} \quad (4.42)$$

Substituting definition of regression rate in the above equation, we get

$$\begin{aligned} \frac{dq}{d\bar{x}} &= \frac{aL_p x^m (G_0 + 4\rho_s q)^n}{D_0} \\ \frac{dq}{d\bar{x}} &= \left(\frac{L_p}{D_0}\right) ax^m (G_0 + 4\rho_s q)^n \end{aligned} \quad (4.43)$$

The above eq. 4.43 is first order differential equation with an initial condition

$$q(0) = 0$$

Now using the definition of continuity for the solid fuel added to the combustion process, the expression obtained is

$$dw_g = \rho_s \dot{r} dA_g \quad (4.44)$$

Where the small area is the product of the circumference times the thickness of the section

$$dA_g = C dx \quad (4.45)$$

Using equation of continuity from equation 4.8 in the flow instead of w

$$w = \rho AV \quad (4.46)$$

Rearranging terms and substituting the circumference of circle in (4.44) we get

$$\frac{dw_g}{dx} = \rho_f \dot{r} C = \rho_f \dot{r} \pi D_0 \quad (4.47)$$

$$\frac{1}{w L_p} \frac{dw_g}{d\bar{x}} = \frac{\rho_f \dot{r} \pi D_0}{\rho AV} = \frac{\rho_f \pi D_0}{\rho AV} a x^m (G_0 + 4\rho_f q)^n \quad (4.48)$$

$$\rho_f \dot{r} = \rho V_g \quad (4.49)$$

where V_g is the speed of the injected gas into the stream, ρ_f is the density of the solid fuel, \dot{r} is the regression rate of the solid fuel and ρ is the density of the oxidizer

$$V_g = \frac{\rho_f}{\rho} \dot{r} = \frac{\rho_f}{\rho} a x^m (G_0 + 4\rho_f q)^n \quad (4.50)$$

$$\frac{dH}{d\bar{x}} \frac{1}{C_p T} = \frac{1}{C_p T} \frac{dh_{pr}}{d\bar{x}} - \frac{1}{C_p T} (C_p T_c - C_p T - \frac{V_g^2}{2} + \frac{V^2}{2}) \frac{1}{w} \frac{dw_g}{d\bar{x}} \quad (4.51)$$

$$\frac{dH}{d\bar{x}} \frac{1}{C_p T} = \frac{1}{C_p T} \frac{dh_{pr}}{d\bar{x}} - (\frac{T_c}{T} - 1 - \frac{V_g^2}{2C_p T} + \frac{V^2}{2C_p T}) \frac{1}{w} \frac{dw_g}{d\bar{x}}$$

The above six equations (4.36, 4.37, 4.38, 4.39, 4.40, 4.41) are solved to obtain the values for six unknowns and the effect of boundary layer, heat addition and the varying area of the port is checked independently to obtain the Fanno line, the Rayleigh line, and the values with respect to isentropic tables respectively. As discussed earlier we neglected the chemical kinetics and the heat addition values are assumed to be known based on the

choice of propellant. The variation of the flow properties along the axial length for hybrid rocket were calculated at three different diameters by integrating from $\bar{x} = 0.08$ to 1. Note that the relatively small variations of the burn rate and the port diameter as a function of axial distance, except near the origin where the Blasius effect occurs. This leading edge effect is not as pronounced in practice, probably because chemical kinetics delay establishing the combustion zone in the boundary layer. The downstream displacement of the combustion zone would tend to decrease the heat transfer at the leading edge. By using the below input values, these equations are solved to find the variation of flow properties along the axial length.

Numerical Setup for D = 0.152 m

The dimensions of the rocket engine we considered for this case is $D_0 = 0.152$ m,

$$\gamma = 1.2, L_p = 4.57m, \dot{m}_o = 7.95kg/s, a = 2.066e-5, m = -0.15, n = 0.75, \rho_f = 1000 \frac{kg}{m^3}, T_c = 3000K, T = 300K, P = 2 MPa, (OF)_0 = 2, MW = 27, R = 8314 \frac{J}{Kg.mol.K}, f = 0, q_{pr} = 4.5e6 \frac{J}{kg}.$$

	x(m)	0.381	0.762	1.143	1.524	1.905	2.286	2.667	3.048	3.429	3.81	4.191	4.572
	Port Dia.(m)	0.152	0.152	0.152	0.152	0.152	0.152	0.152	0.152	0.152	0.152	0.152	0.152
	(cm/sec)	0.263	0.231	0.221	0.217	0.215	0.215	0.215	0.216	0.218	0.219	0.221	0.224
t = 0.1 sec	O/F	17.19	9.102	6.316	4.835	3.917	3.31	2.852	2.506	2.234	2.016	1.831	1.667

Table 4.1. Reference Values for the results from Altman at D = 0.152 m

The results obtained below from Fig 4.2 to Fig 4.7 is a close match to the reference values that are defined above.

Results & Discussion for $D = 0.152$ m

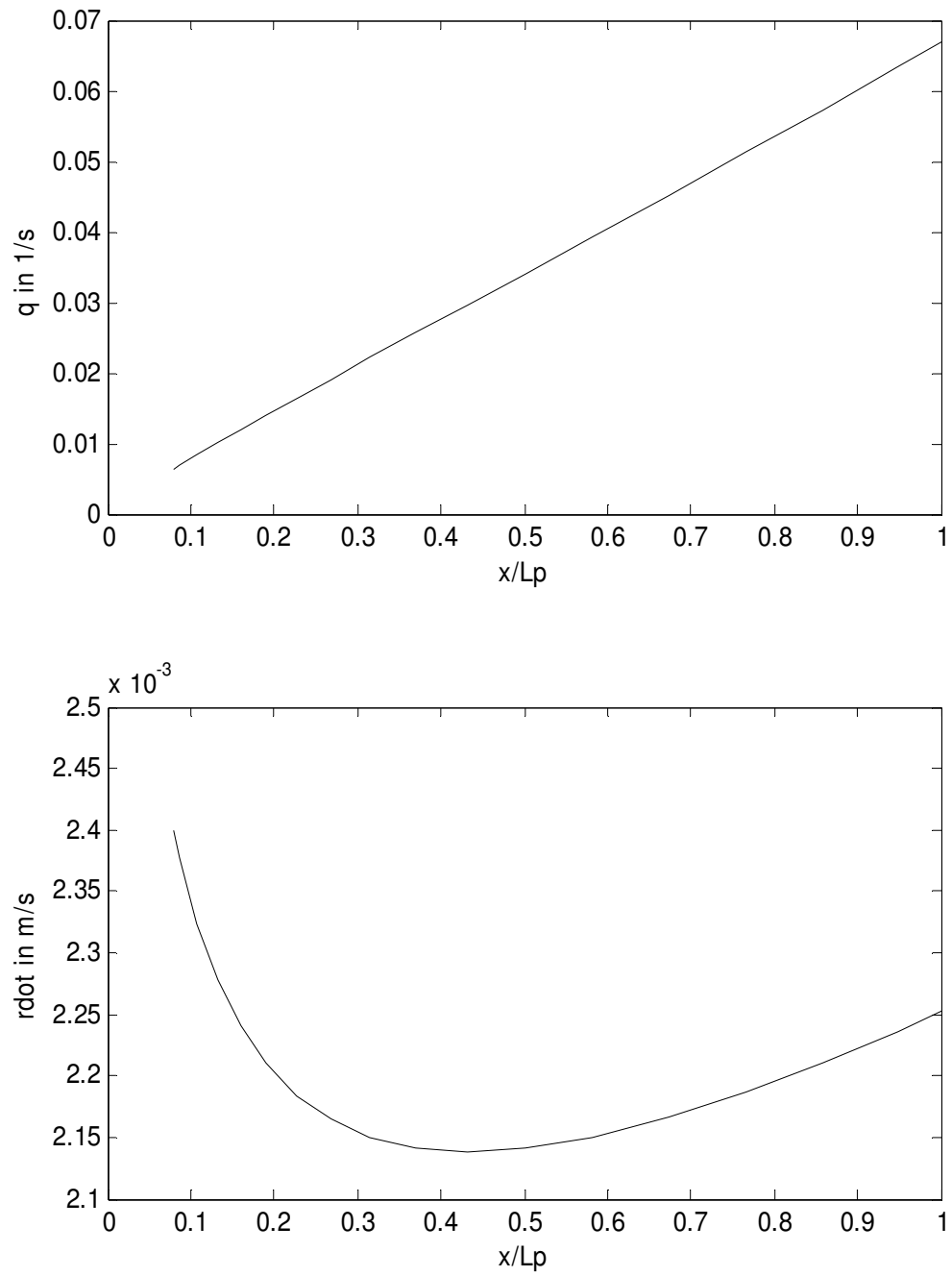


Figure. 4.2. Integration factor q and Regression rate vs distance down the port

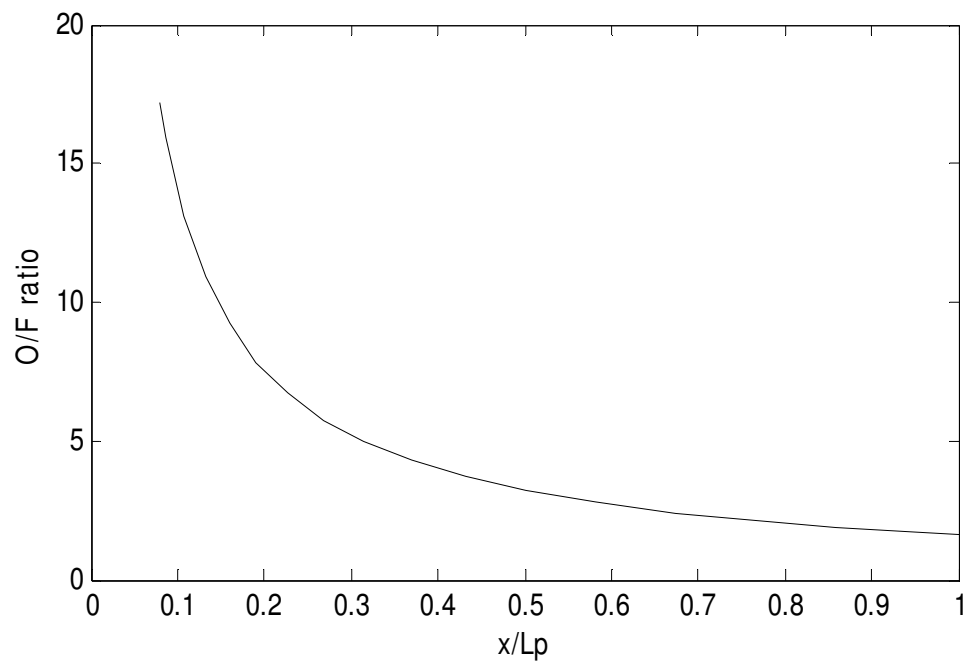
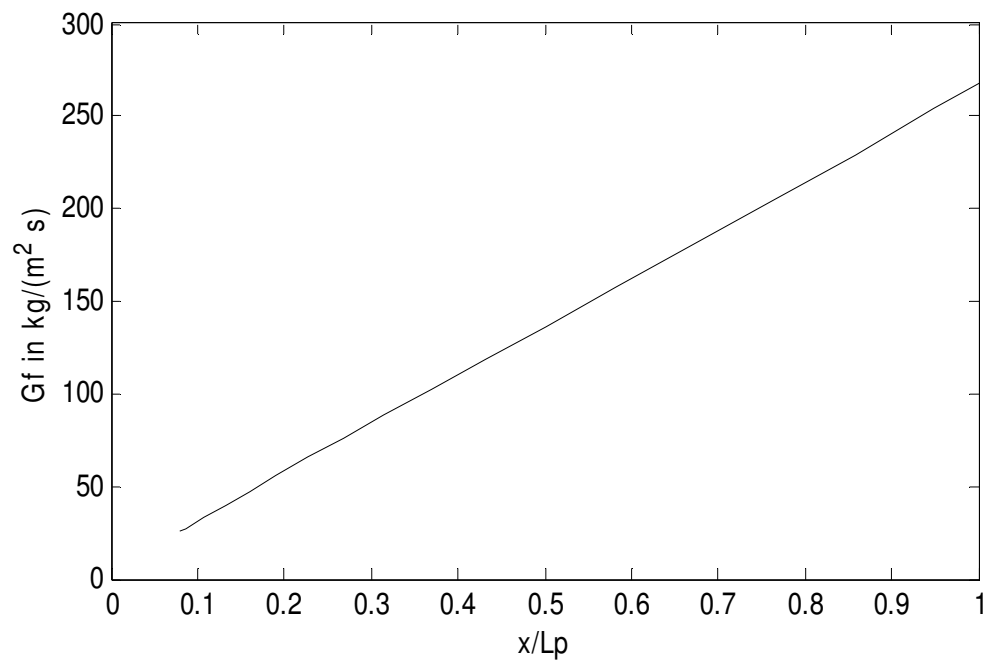


Figure. 4.3. Fuel flux and (OF) ratio vs distance down the port

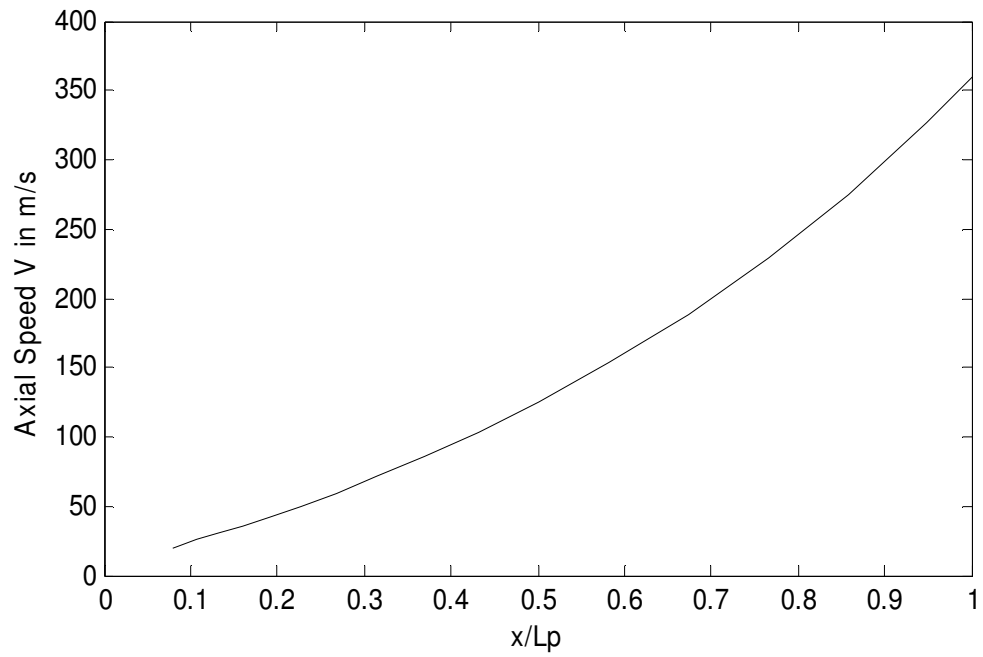
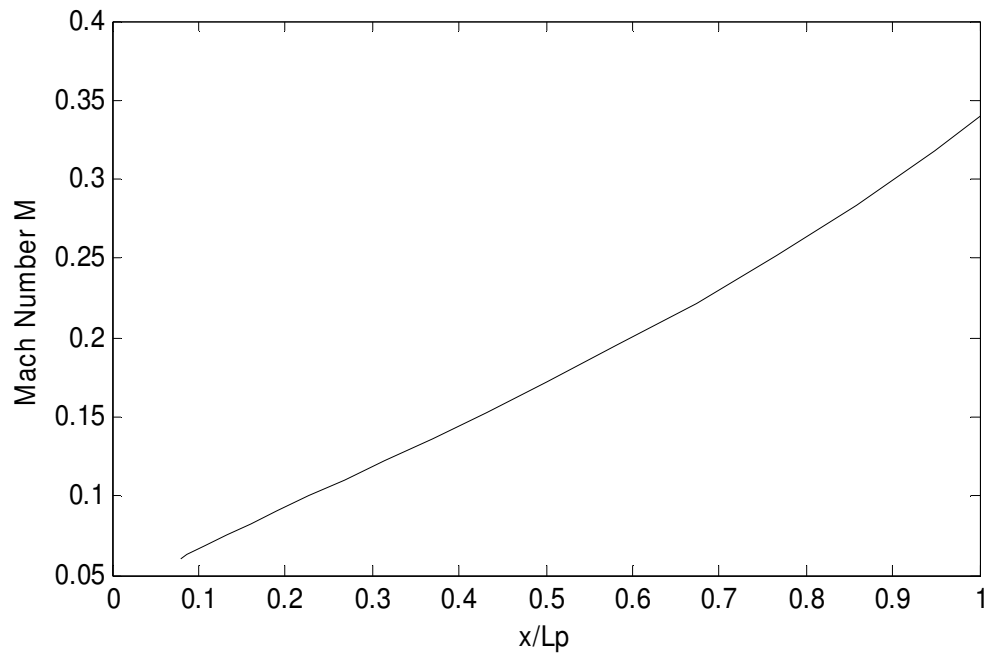


Figure. 4.4. Mach number and axial speed vs distance down the port

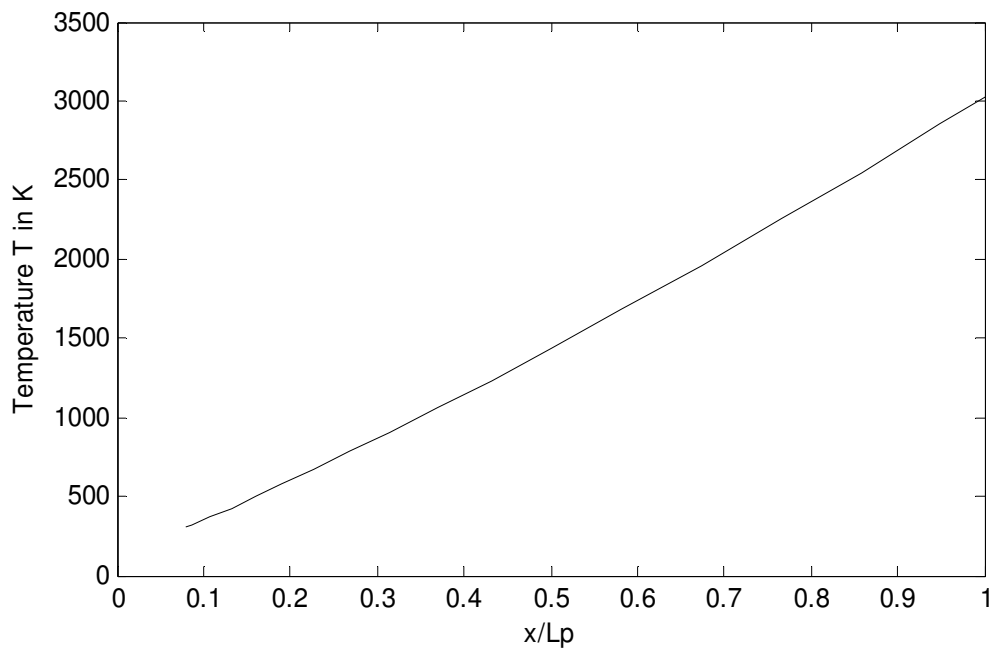
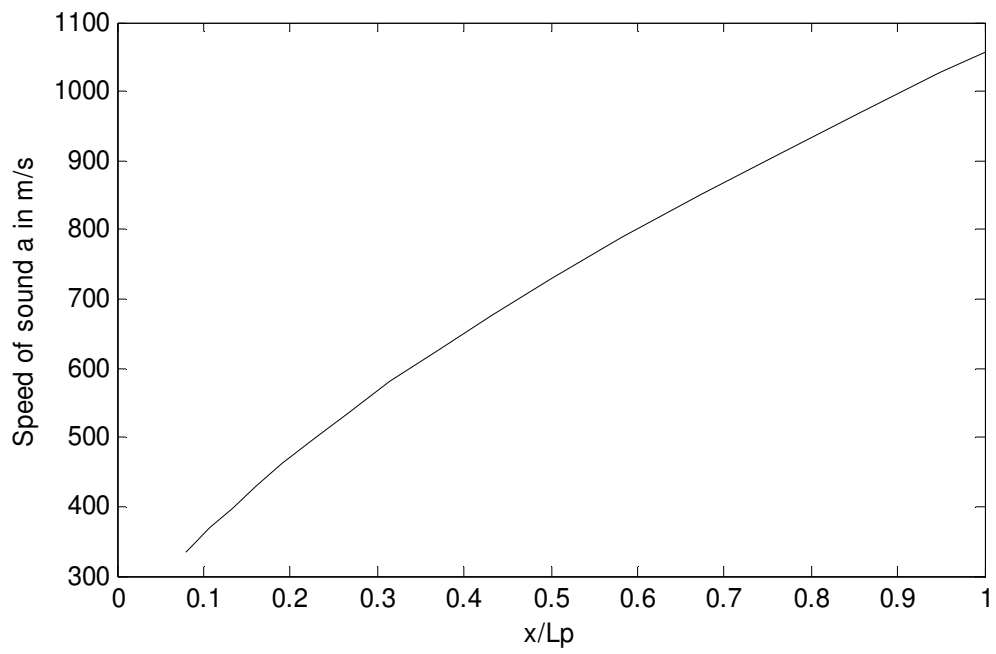


Figure. 4.5. Speed of sound and Temperature vs distance down the port

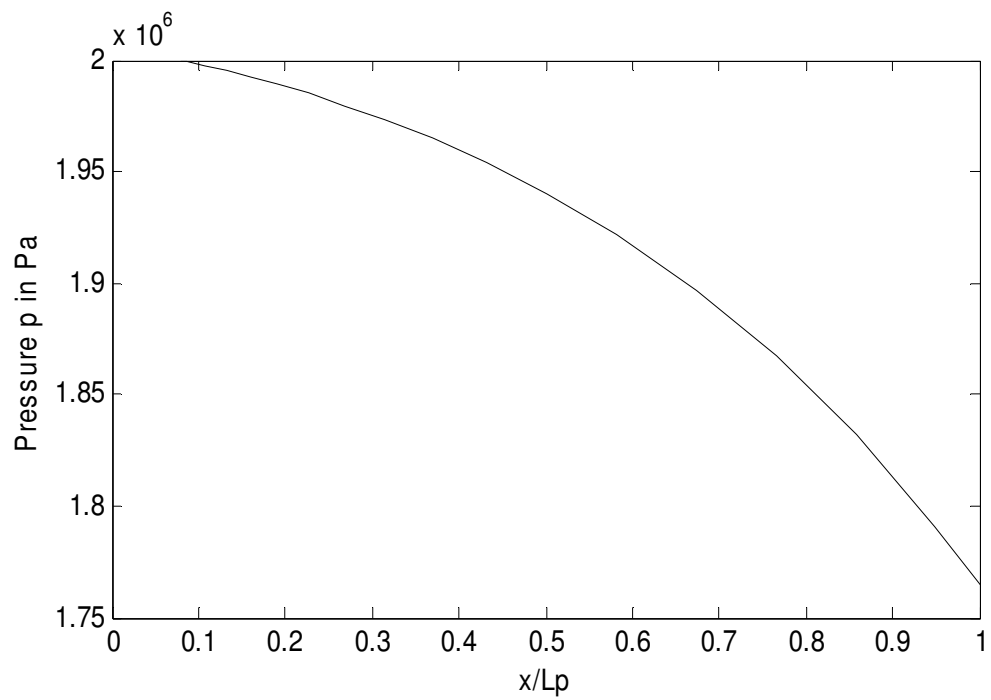
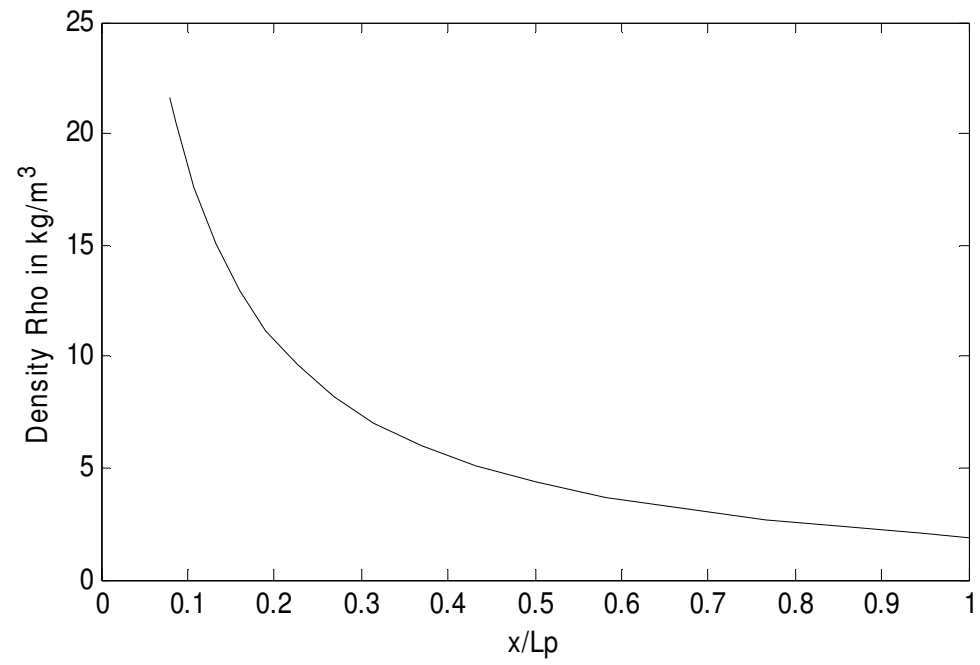


Figure. 4.6. Density and Pressure vs distance down the port

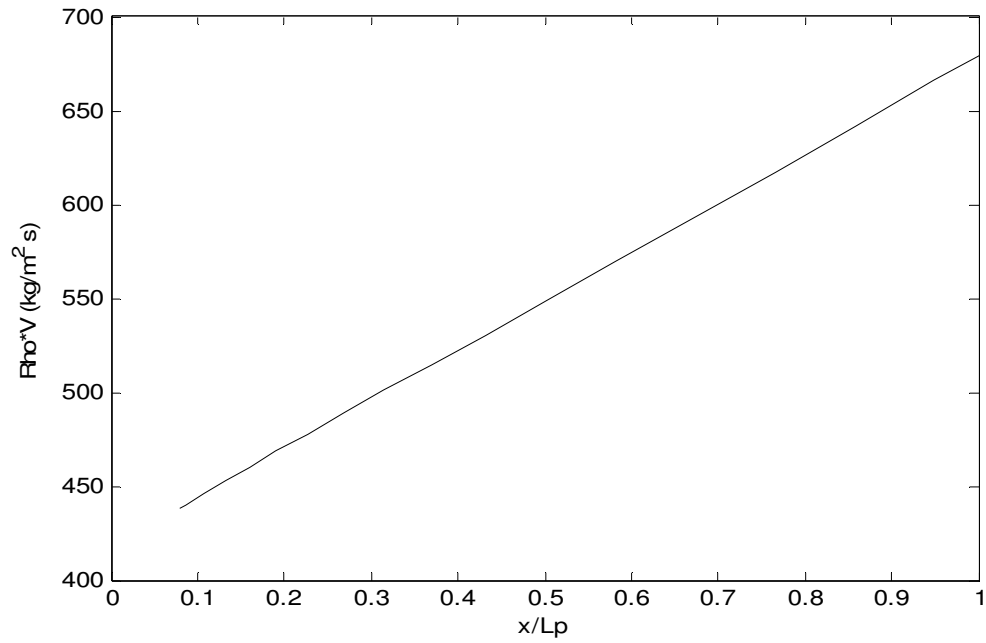


Figure. 4.7. ρV vs distance down the port

Numerical Setup for $D = 0.215$ m

The dimensions of the rocket engine we considered for this case is $D_0 = 0.215$ m,

$$\gamma = 1.2, L_p = 4.57m, \dot{m}_o = 7.95kg/s, a = 2.066e-5, m = -0.15, n = 0.75, \rho_f = 1000 \text{ kg/m}^3, T_c = 3000k, T = 300k, P = 2 \text{ MPa}, (OF)_0 = 2, MW = 27, R = 8314 \text{ J/Kg.mol.k}, f = 0, dh_{pr} = 4.5e6 \text{ J/kg}.$$

x(m)		0.381	0.762	1.143	1.524	1.905	2.286	2.667	3.048	3.429	3.81	4.191	4.572
t = 20 sec	Port Dia.(m)	0.227	0.22	0.217	0.216	0.215	0.215	0.215	0.215	0.216	0.216	0.216	0.217
	(cm/sec)	0.143	0.131	0.127	0.125	0.123	0.123	0.123	0.123	0.123	0.123	0.124	0.124
	O/F	21.34	11.4	7.983	6.139	4.974	4.177	3.594	3.115	2.771	2.495	2.263	2.073

Table 4.2. Reference Values for the results from Altman at $D = 0.215$ m

The results obtained below from Fig 4.8 to Fig 4.13 is a close match to the reference values that are defined above.

Results & Discussion for $D = 0.215$ m

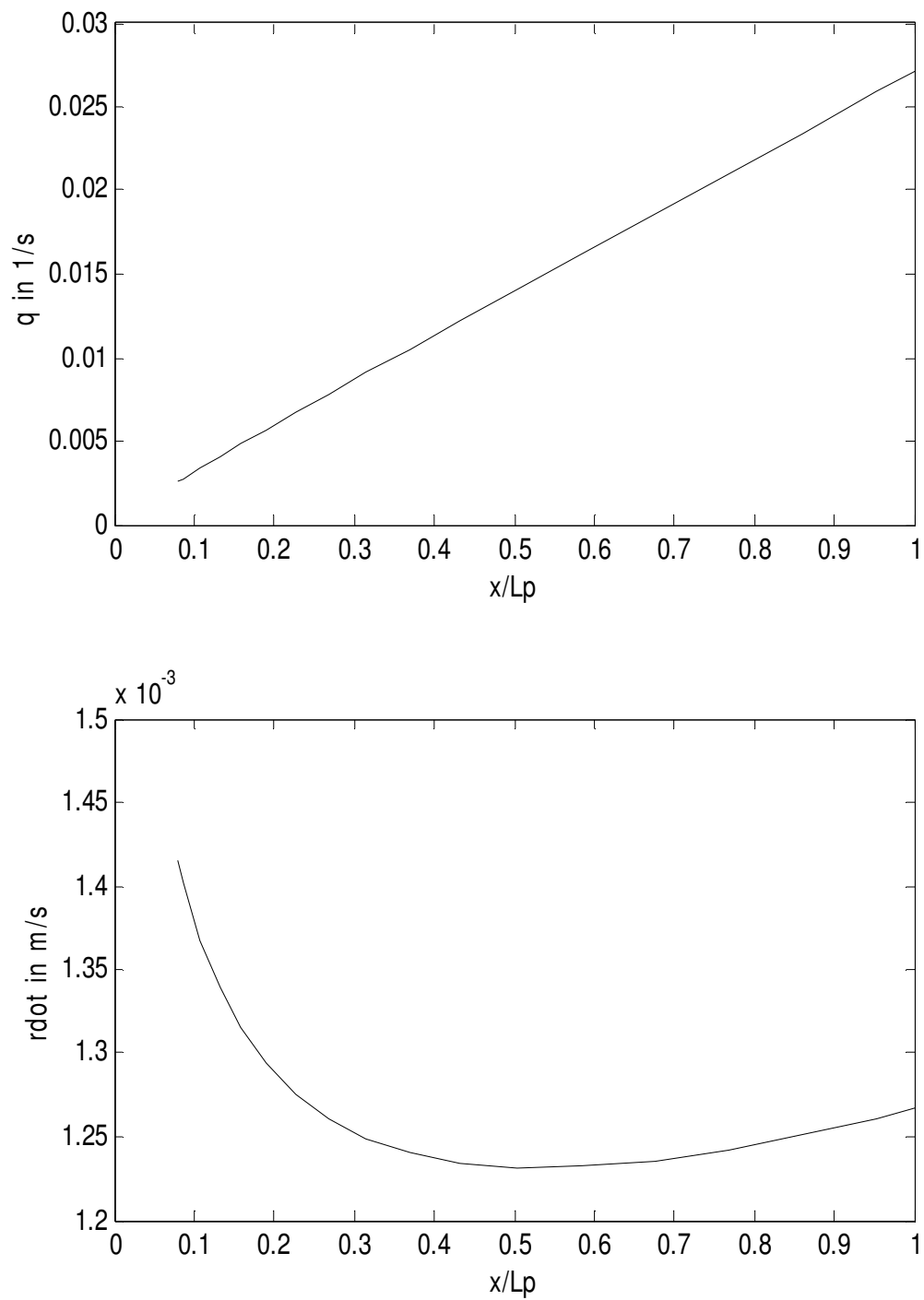


Figure. 4.8. Integration factor and regression rate vs distance down the port

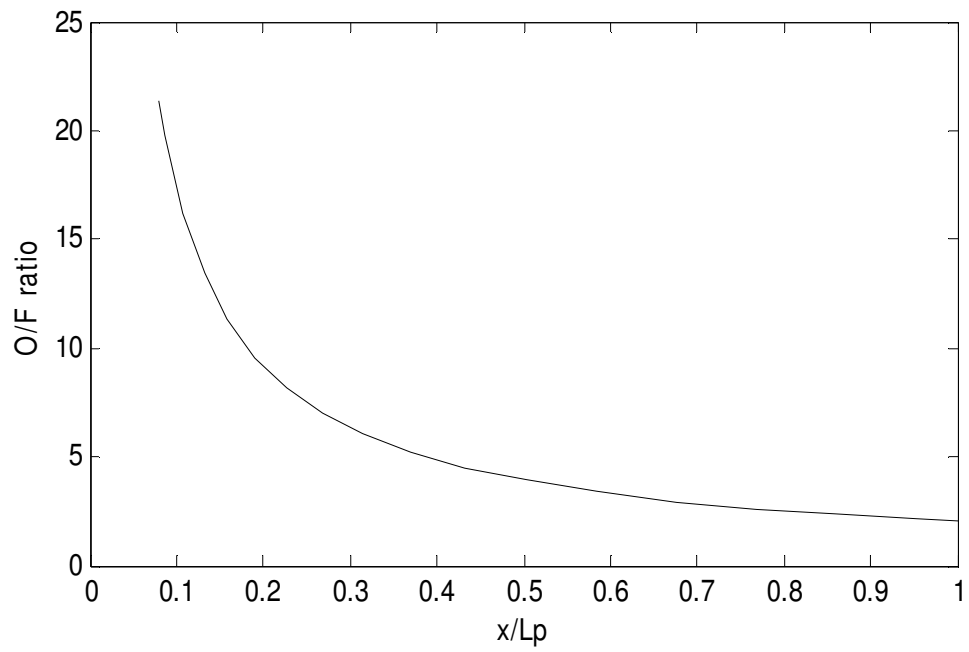
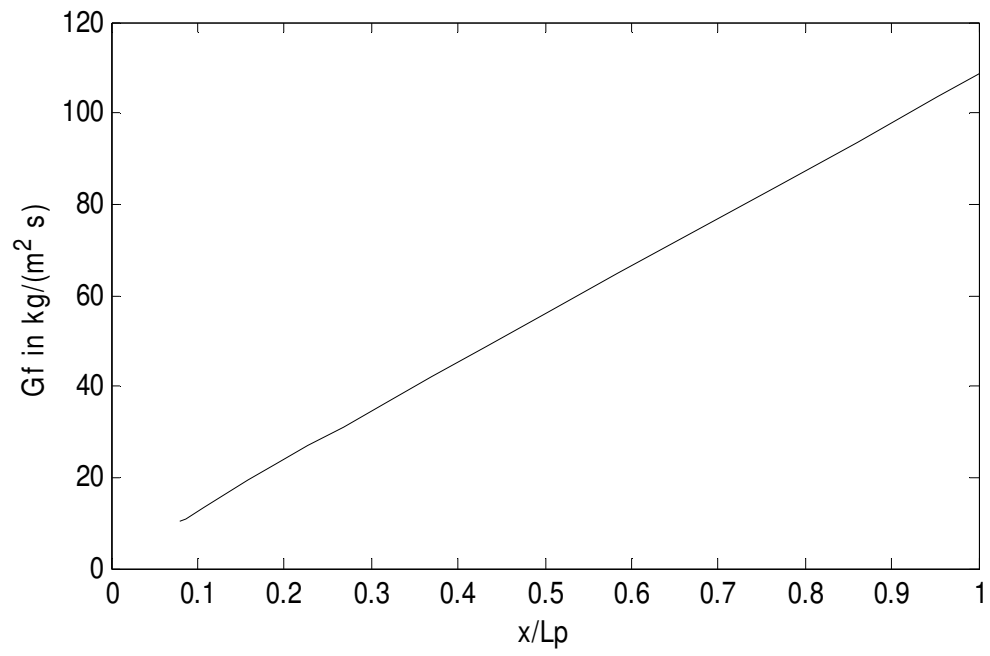


Figure. 4.9. Fuel flux and OF ratio vs distance down the port

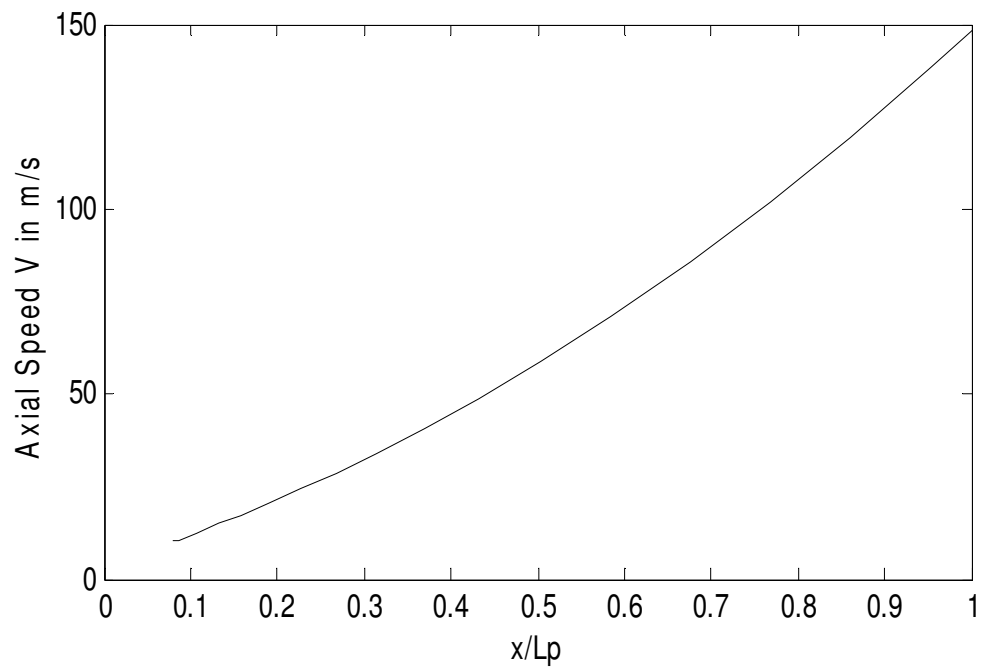
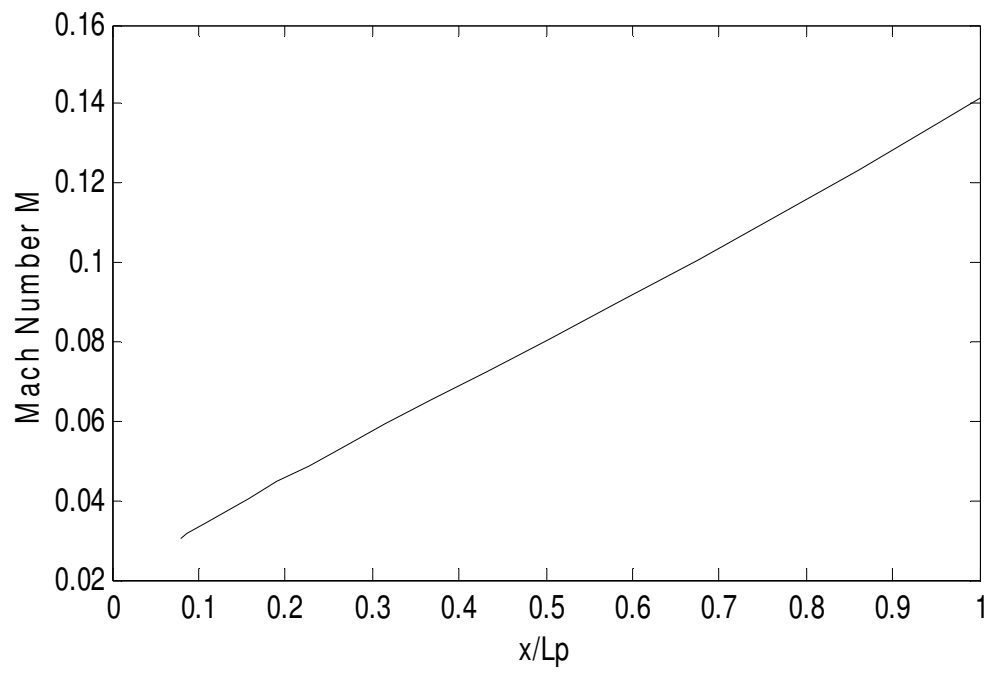


Figure. 4.10. Mach number and axial speed vs distance down the port

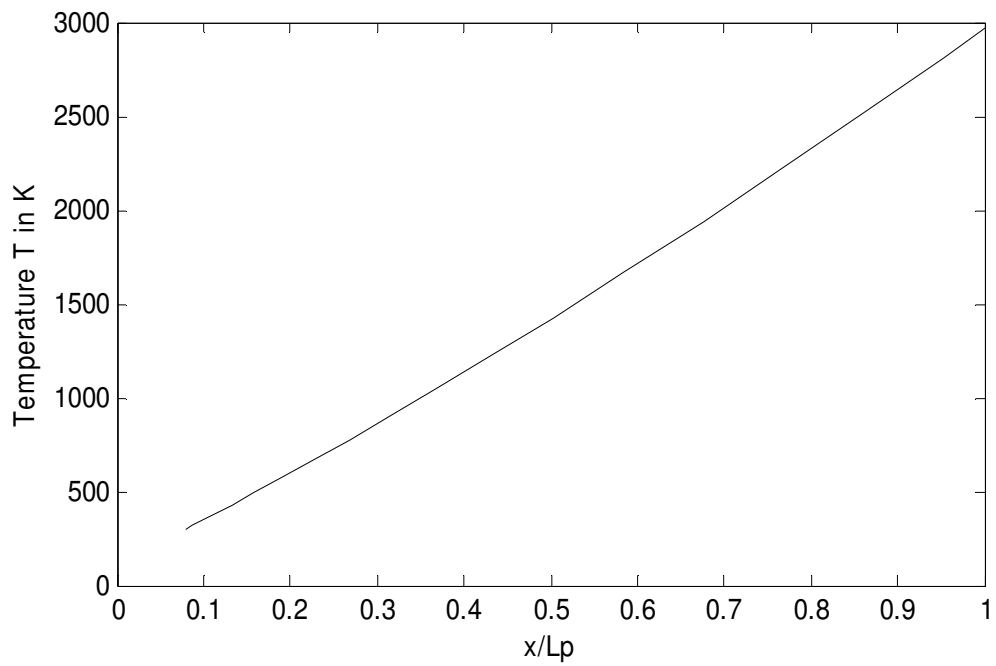
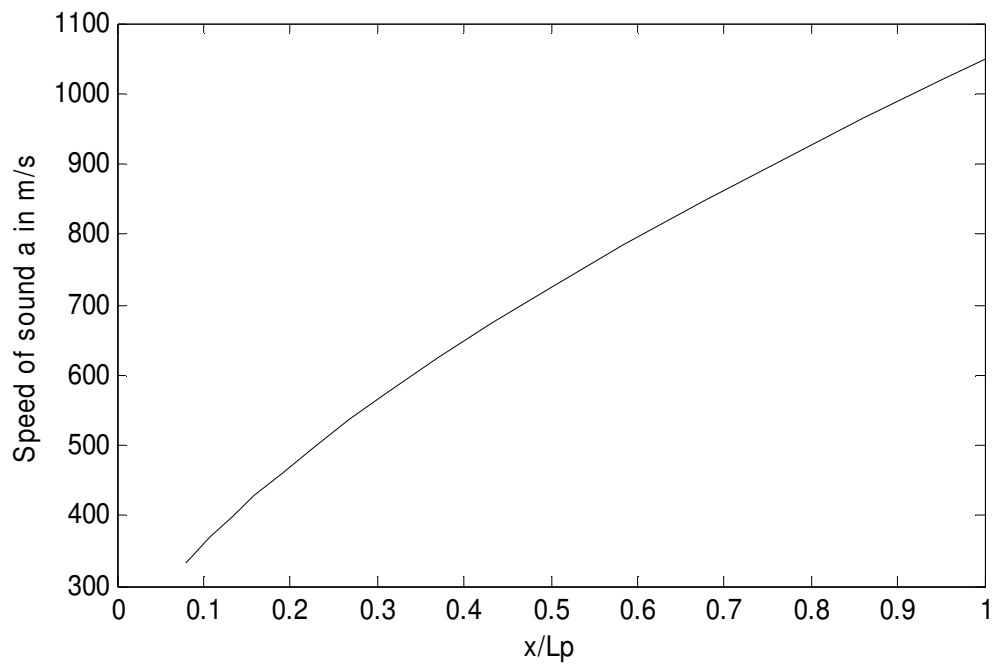


Figure. 4.11. Speed of sound and Temperature vs distance down the port

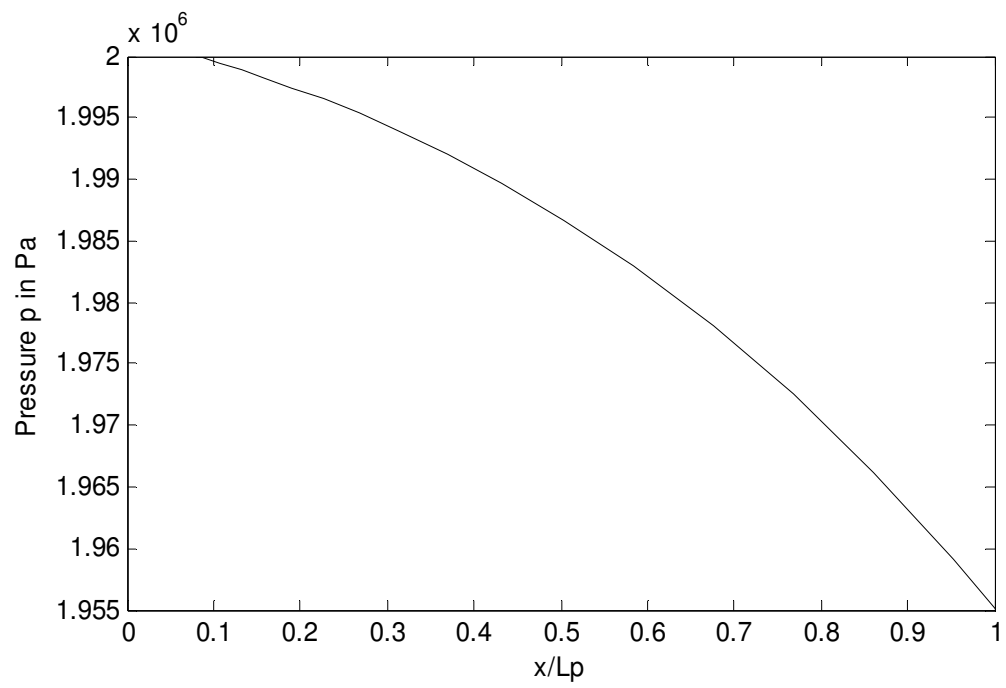
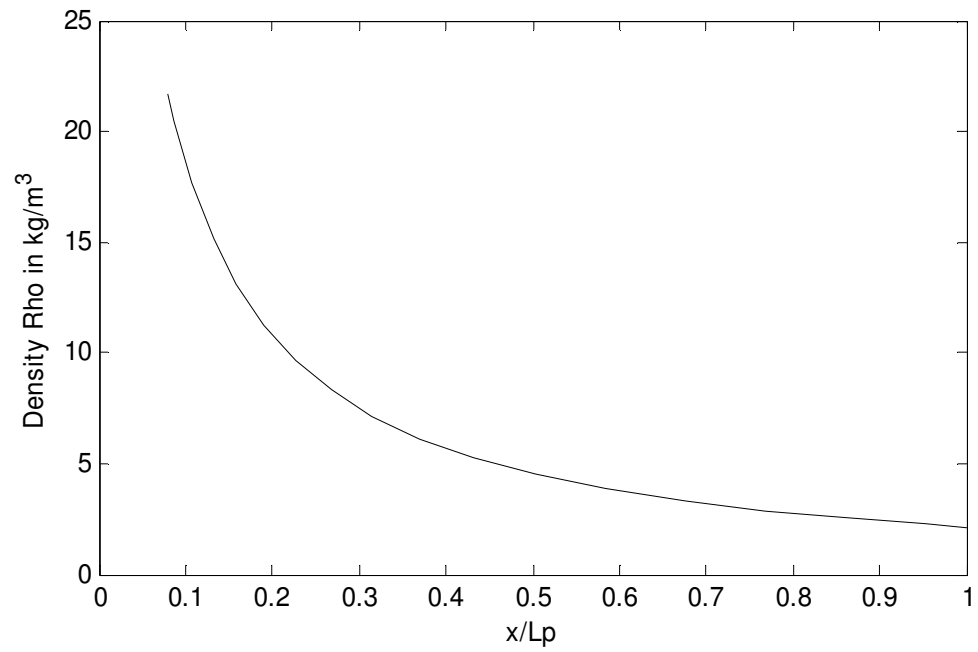


Figure. 4.12. Density and Pressure vs distance down the port

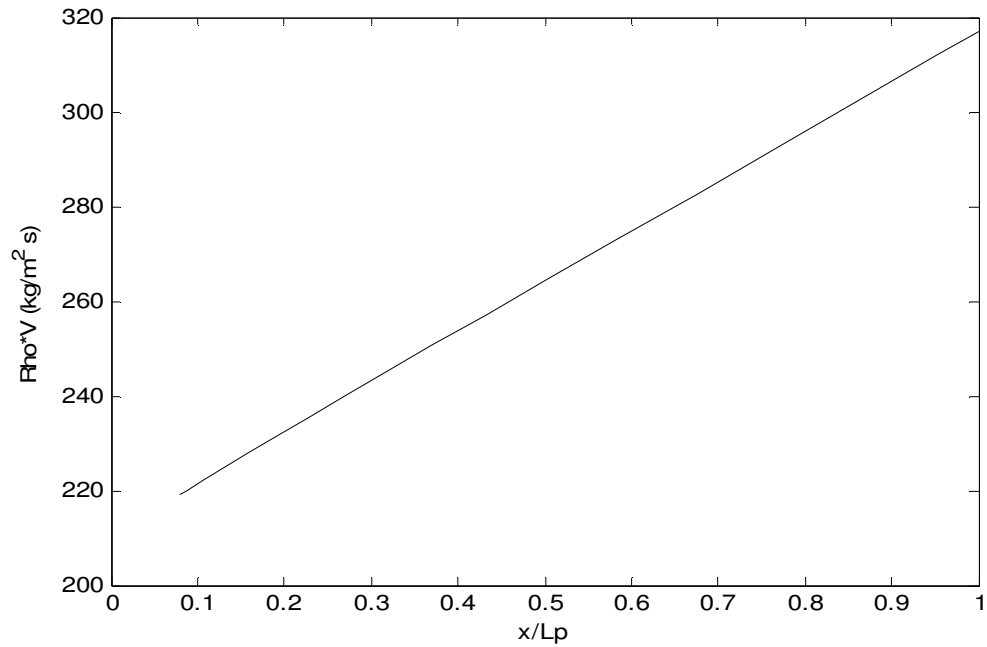


Figure. 4.13. ρV vs distance down the port

Numerical Setup for $D = 0.291$ m

The dimensions of the rocket engine we considered for this case is $D_0 = 0.291$ m,

$\gamma = 1.2$, $L_p = 4.57$ m, $\dot{m}_o = 7.95$ kg/s, $a = 2.066 \times 10^{-5}$, $m = -0.15$, $n = 0.75$, $\rho_f =$

1000 kg/m³, $T_c = 3000$ K, $T = 300$ K, $P = 2$ MPa, $(OF)_0 = 2$, $MW = 27$, $R = 8314$

J/Kg.mol.K, $f = 0$, $dh_{pr} = 4.5 \times 10^6$ J/kg.

x(m)		0.381	0.762	1.143	1.524	1.905	2.286	2.667	3.048	3.429	3.81	4.191	4.572
t = 60 sec	Port Dia.(m)	0.315	0.301	0.296	0.293	0.292	0.291	0.291	0.291	0.291	0.292	0.292	0.293
	(cm/sec)	0.087	0.081	0.078	0.077	0.076	0.076	0.076	0.075	0.075	0.075	0.075	0.076
	O/F	24.11	13.2	9.64	7.249	6.006	4.972	4.342	3.757	3.375	3.008	2.747	2.492

Table 4.3. Reference Values for the results from Altman at $D = 0.291$ m

The results obtained below from Fig 4.14 to Fig 4.19 is a close match to the reference values that are defined above.

Results & Discussion for $D = 0.291$ m

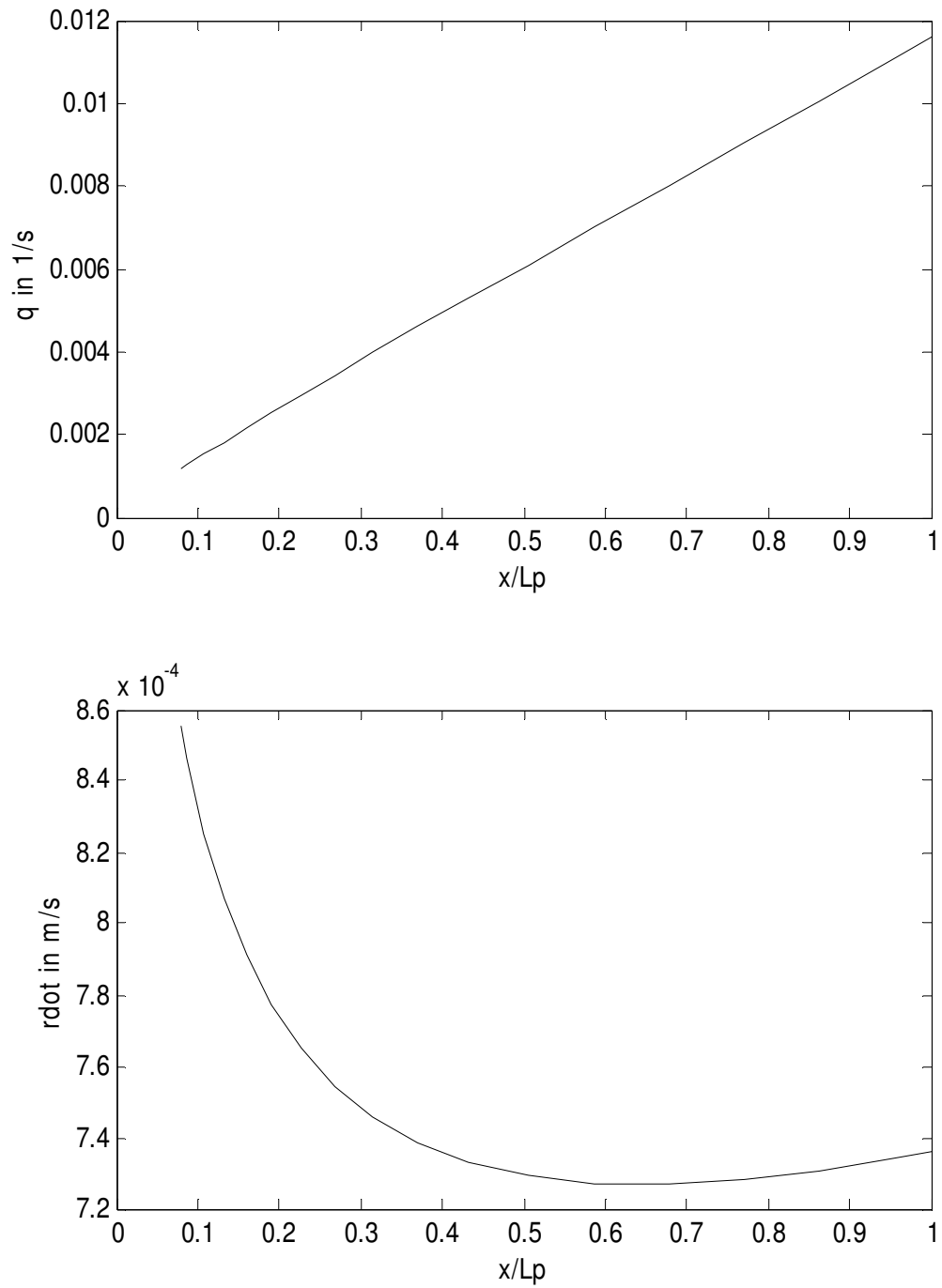


Figure. 4.14. Integration factor and regression rate vs distance down the port

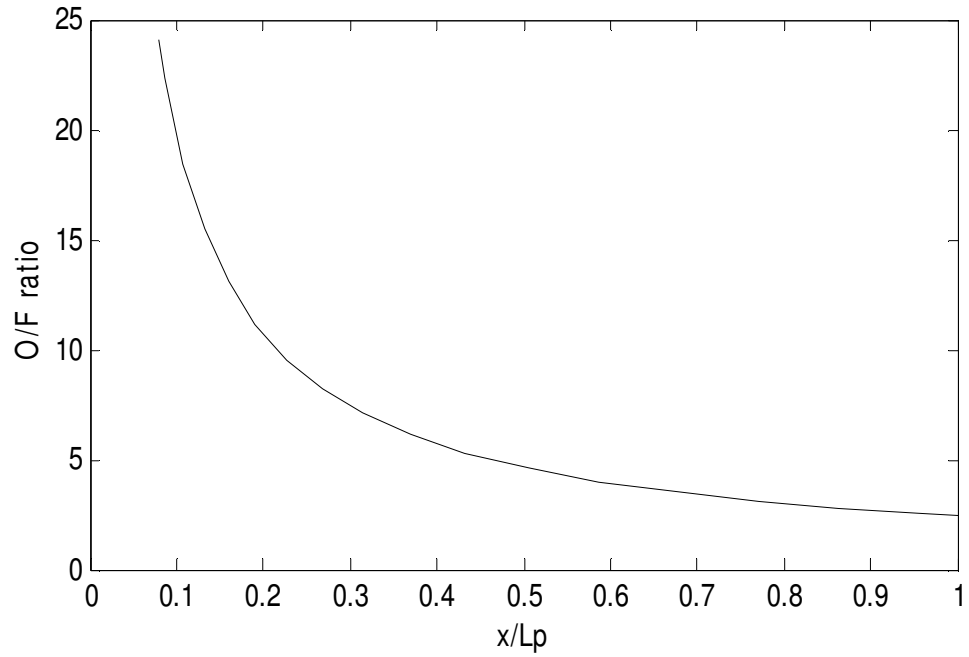
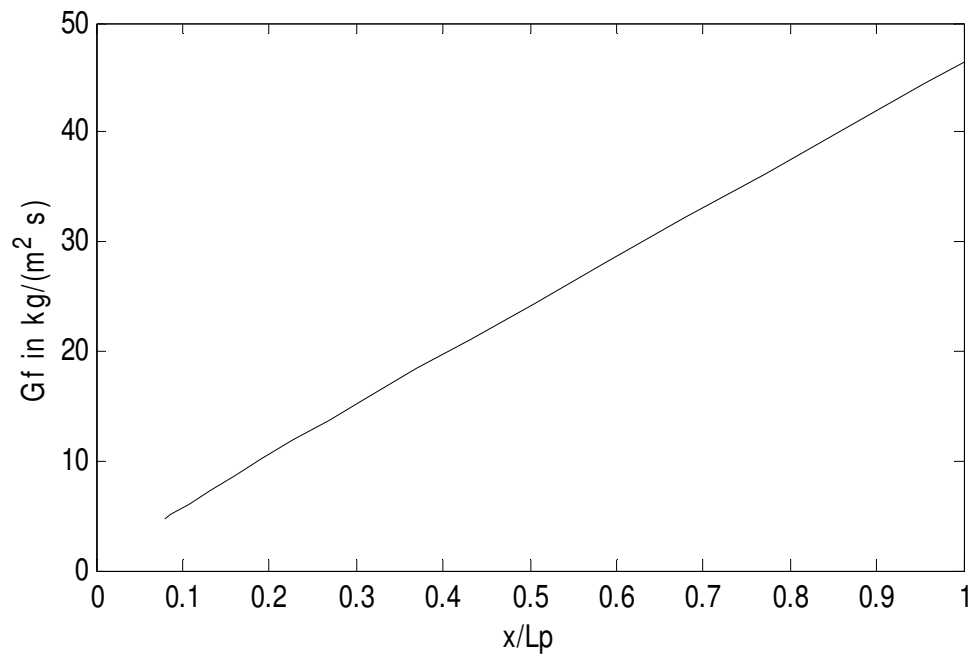


Figure. 4.15. Fuel flux and OF ratio vs distance down the port

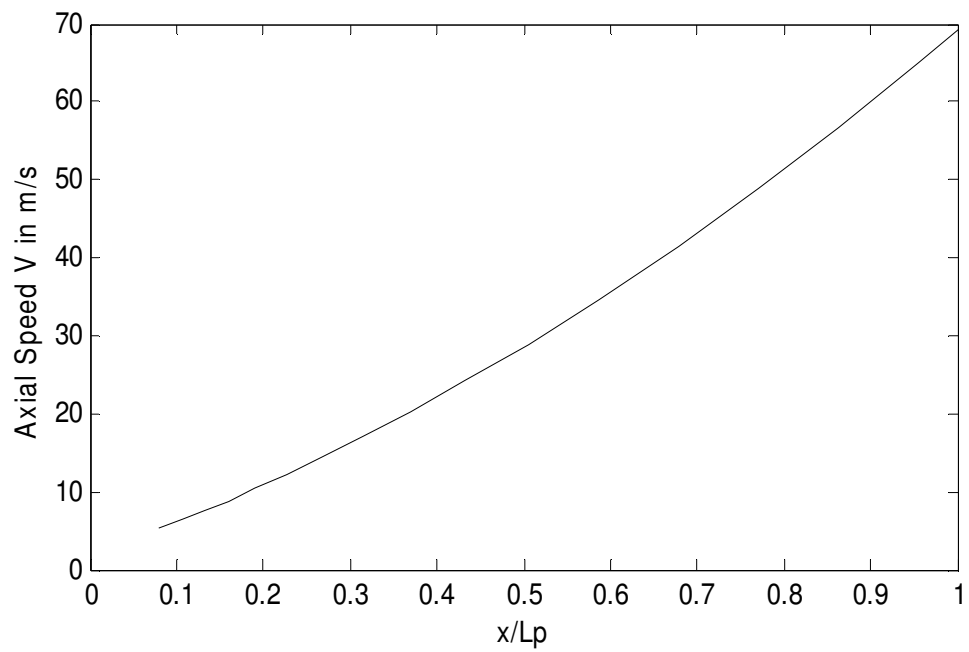
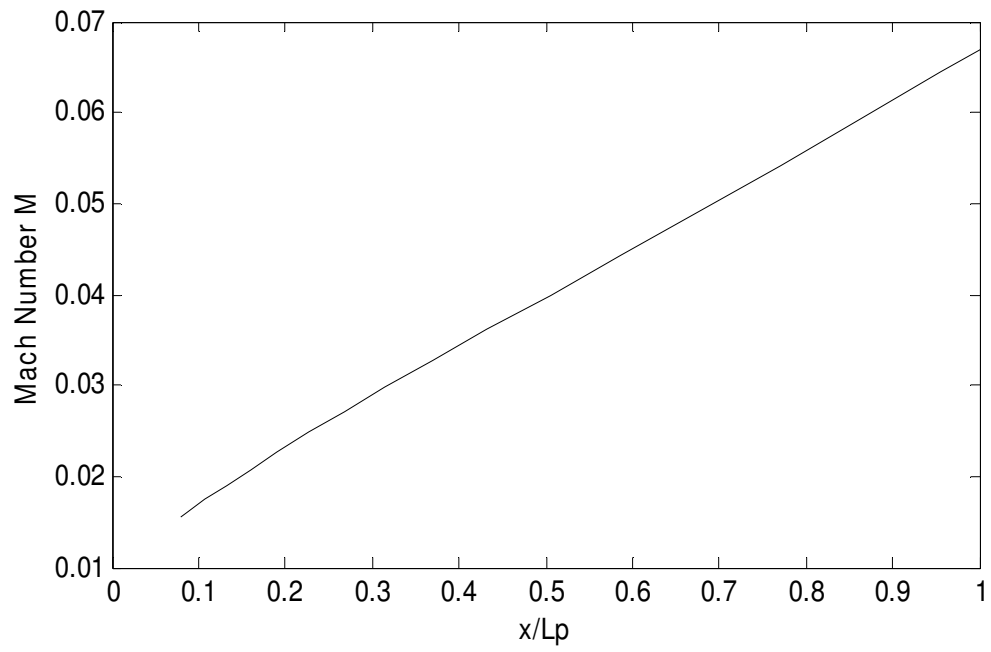


Figure. 4.16. Mach number and axial speed vs distance down the port

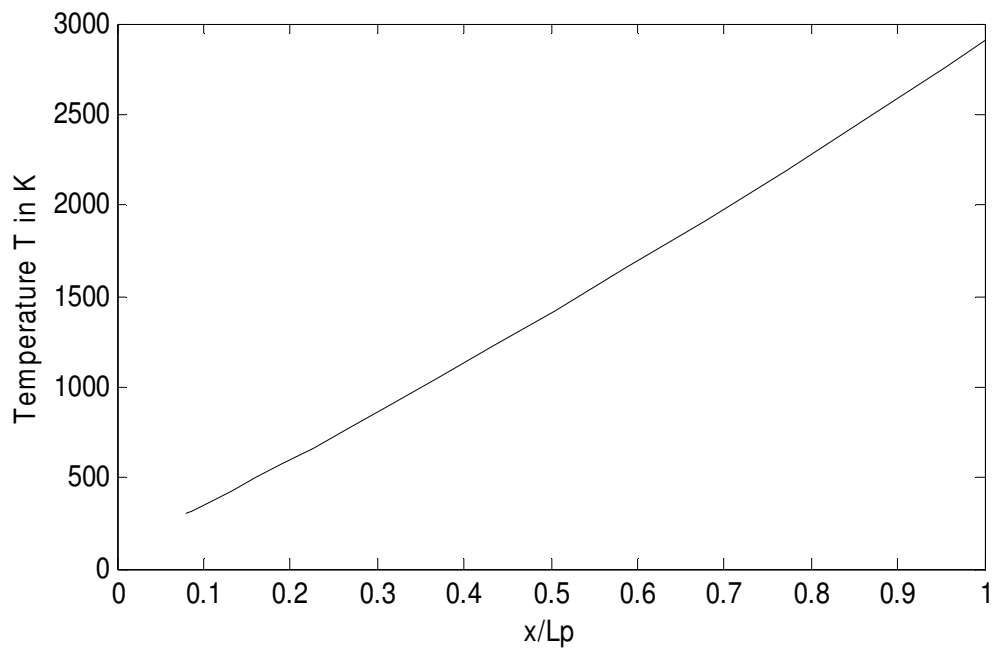
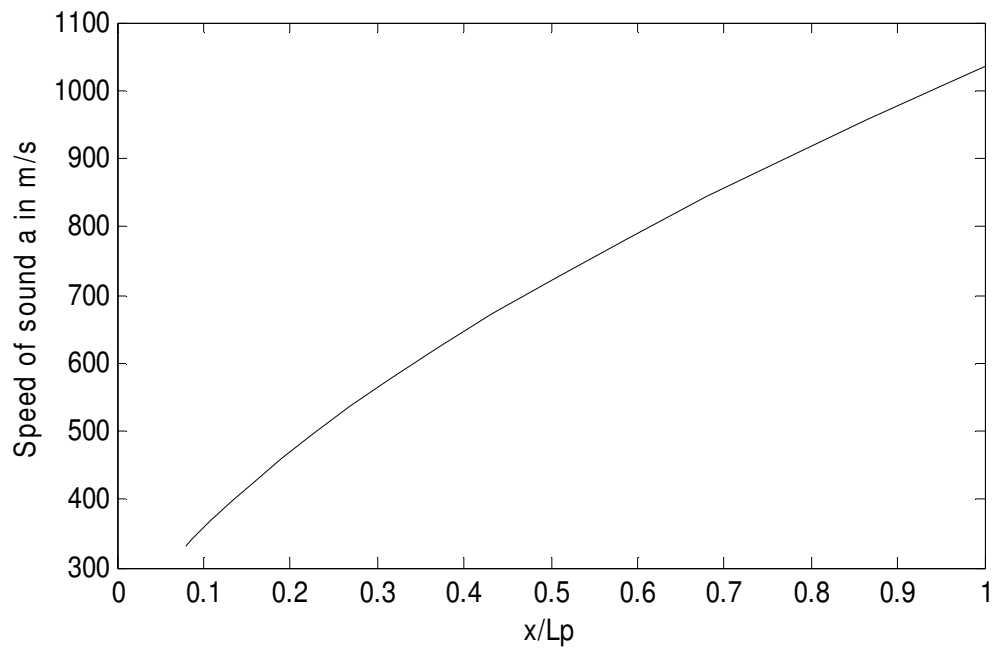


Figure. 4.17. Speed of sound and Temperature vs distance down the port

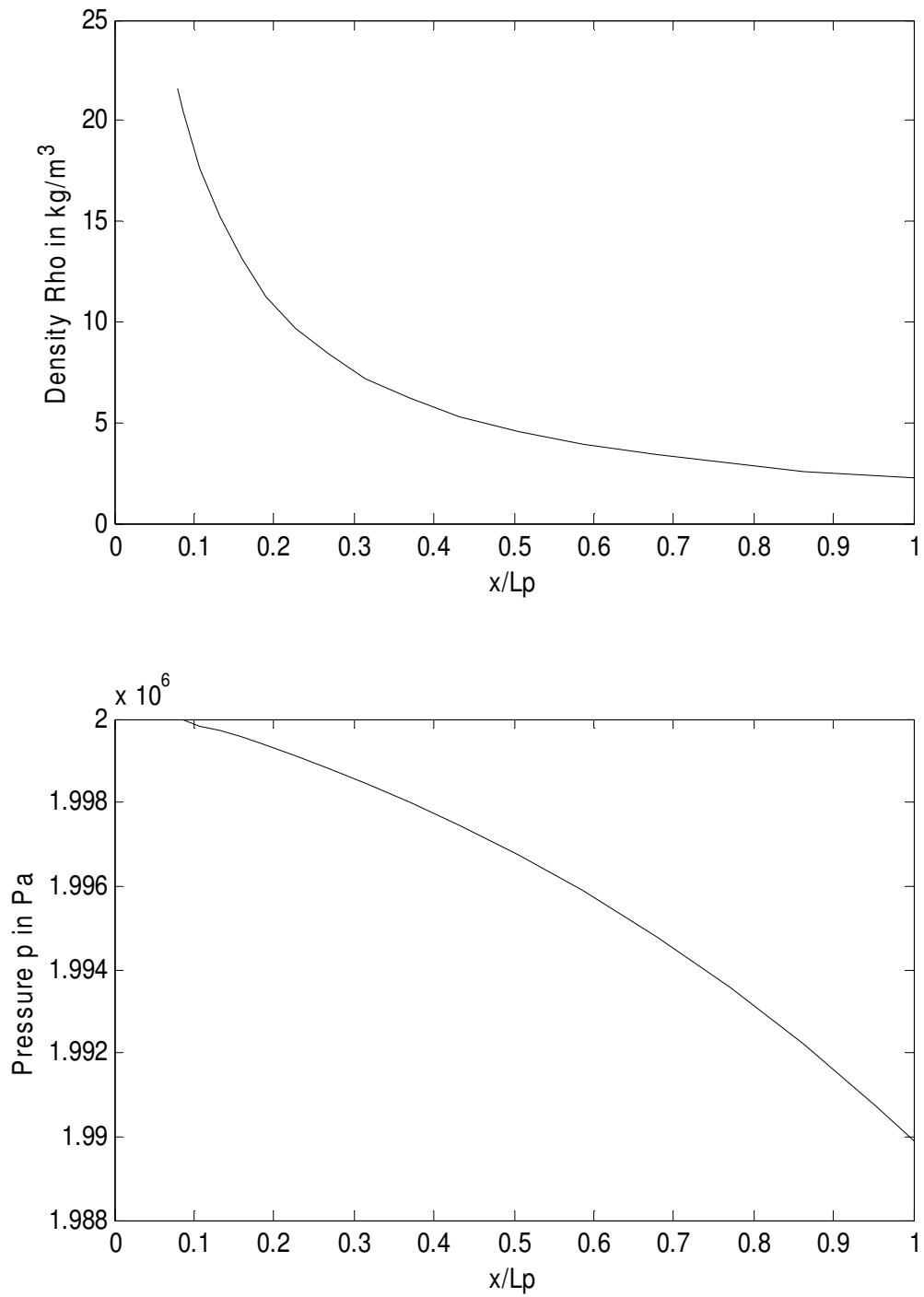


Figure. 4.18. Density and Pressure vs distance down the port

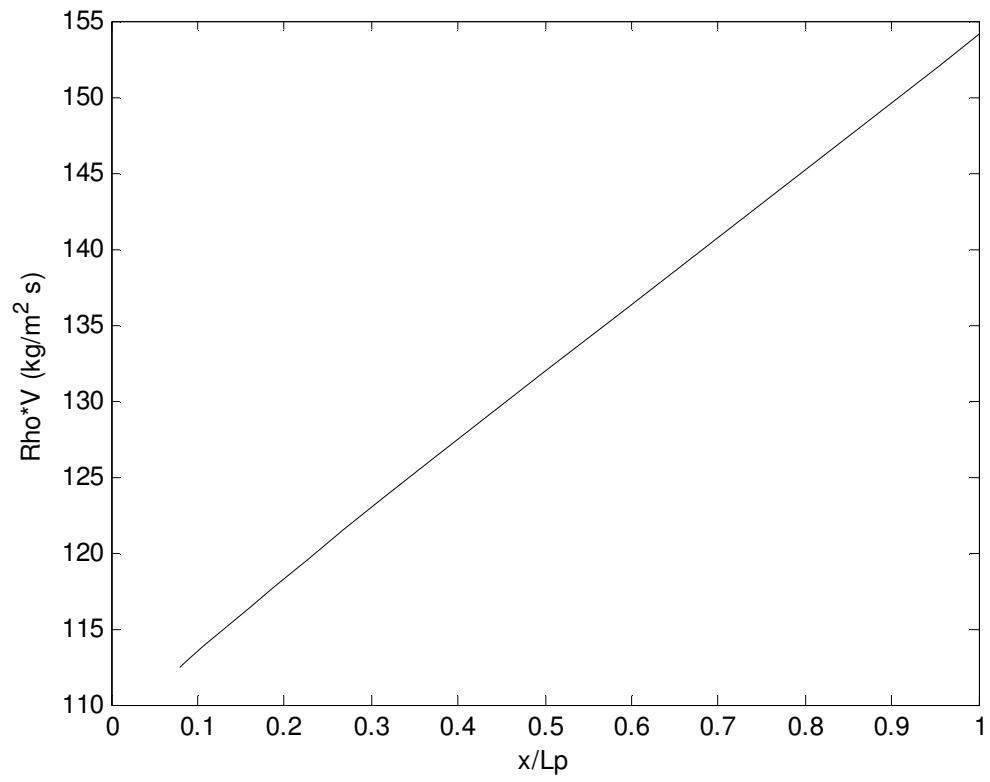


Figure. 4.19. ρV vs distance down the port

Conclusions

In the present work, the internal ballistics of a hybrid rocket are analyzed by simplifying the combustion chamber using two models. In the first model, the time variations of the fluid properties are calculated, assuming uniform properties along the axial direction. The second model calculates the thermodynamic properties of the fluid by considering the axial variations along the port in a steady state condition.

The analysis of square ports in a hybrid rocket is simple when compared to other complicated port geometries such as a wagon wheel configuration. Fuel grains with several ports in a hybrid rocket engine are analyzed by transforming the ports into equivalent square ports. As a part of the first model, a single circular port is first considered. The results obtained for a single circular port using the proposed analysis agree with previously published results. The values of the oxidizer to fuel ratio (O/F) and the regression rate coincide with the research work done by Altman. Then a four circular ports configuration is studied assuming the burn time, web thickness and the mass of the fuel to be the same as in the case of a single circular port. The four circular ports configuration shows that there is an increase in the O/F ratio and in the regression rate when compared to the single circular port configuration. However the length of the solid fuel grain is reduced from that of single port geometry. The same exit velocity and thrust can be reached in the two configurations.

A single square port, which is equivalent to a single circular port is considered assuming the burn time, web thickness and the mass of the fuel to be the same. The results show that there is a decrease in the O/F ratio, the regression rate and the web thickness as compared to a circular port. This single square port configuration has a less

O/F shift and lower propellant mass flux rates when compared to a circular port configuration. The transformed four square ports configuration gives better operating values than that of the four circular ports configuration and the propellant mass flux rates are within the operating range of 350 to 700 kg/(m² s). There is an increase in the O/F ratio and the regression rates when compared with a single port configuration. The volumetric efficiency for different number of square ports is calculated, which gives a maximum volumetric efficiency value for nine ports. The burn time, web thickness and the mass of the fuel are made constant in all the cases. The same exit velocity and thrust are obtained in all cases.

The second model deals with the axial variations along the port assuming a steady state condition. The combined effects of wall mass injection and heat addition are taken into account assuming one-dimensional compressible flow analysis. The wall mass injection is introduced into the model by assuming the evaporated gas that enters the control volume is equal to the solid fuel that is regressed from the surface. This analysis allows prediction of the Mach number and the thermodynamic properties of the combustion products along the port. By combining the above two models more accurate results can be obtained for the hybrid rocket.

Future work

- Study chemical kinetics and the diffusion flame in order to predict the heat of reaction and the temperature across the port section.
- Study a combination of spatial and temporal variations of the fluid properties.
- Complicated geometries like wagon wheel configuration can be easily analyzed by transforming them into square ports.
- Study optimization of hybrid rockets using various criteria and constraints.
- Study combustion instabilities in hybrid rockets.

References

- Arisawa H, and Brill T. B. 1996. "Flash Pyrolysis of HTPB I: Analysis and Implications of the Gaseous Products," *Combustion and Flame*, Vol. 106, Nos. 1-2. Pp 131-143. Doi: 10.1016/0010-2180(96)00253-2.
- Arisawa H, and Brill T. B. 1996. "Flash Pyrolysis of HTPB II: Implications of the Kinetics to Combustion of Organic Polymers," *Combustion and Flame*, Vol. 106, No. 1. Pp 144-154. Doi: 10.1016/0010-2180(95)00254-5.
- Ascher H. Shapiro. 1953. "The Dynamics and Thermodynamics of Compressible Flow," *The Ronald Press Company, New York* pp. 219-228.
- Altman D. 1991. "Hybrid Rocket Development History," *American Institute of Aeronautics and Astronautics paper*, 91-2515.
- Bartel H. R and Rannie W. D. 1946. "Solid Fuel Combustion as Applied to Ramjets," *Jet Propulsion Lab*, Progress Rep. 3-12, California Institute of Technology, Pasadena, CA.
- Emmons H.W. 1953. "Film Combustion of a Liquid Fuel," *Combustion Aerodynamics Lab*, Interim Technical Rep. 6, Harvard University, Cambridge, MA.
- Carmin Carmicino, and Annamaraia Russo Sorge. 2005. "Role of Injection in Hybrid Rockets Regression Rate Behavior," *Journal of Propulsion and Power*, Vol. 21, No. 4, July-August 2005.
- Dario Pastrone. 2012. "Approaches to Low Fuel Regression Rate in Hybrid Rocket Engines," *Hindawi Publishing Corporation International Journal of Aerospace Engineering*. Volume 2012, Article ID 649753, 12 pages. Doi: 10.1155/2012/649753.
- David Altman, and Ronald Humble. 1995. "Hybrid Rocket Propulsion Systems," *The McGraw-Hill Companies Publication* ch-7, pp. 365-440.
- David Altman, and Allen Holzman. 2007. "Overview and History of Hybrid Rocket Propulsion," *American Institute of Aeronautics and Astronautics, Inc., Reston, Virginia*. pp 1-36.
- F. M. Favaro, and W. A. Sirignano, M. Manzoni and L.T. Deluca. 2012. "Solid-Fuel Regression Rate Modeling for Hybrid Rockets," *Journal of Propulsion and Power*, Vol. 29, No. 1, January-February 2013, pp. 205-215. Doi: 10.2514/1.B34513.
- Gilbert. M, and Marxman G. A. 1963. "Turbulent Boundary Layer Combustion in the Hybrid Rocket," *Ninth International Symposium on Combustion*, The Combustion Inst., Pittsburgh, PA, pp. 371-383.
- Guobiao Cai, Peng Zeng, Xintian Li, Hui Tian, and Nanjia Yu. 2011. "Scale effect of fuel regression rate in hybrid rocket motor," *Journal of Aerospace Science and Technology*, Volume 24, issue 1, January-February 2013, pp 141-146.
- Joseph Majdalani. 2007. "Analytical Models for Hybrid Rockets," *American Institute of Aeronautics and Astronautics, Inc., Reston, Virginia*. pp 207-246.

- Macklin F, Grainger C, Veno M, and Benson J. 2003. "New applications for Hybrid Propulsion," *American Institute of Aeronautics and Astronautics paper, Huntsville, Alabama*. 2003-5202.
- Martin J. Chiaverini, Nadir Serin, David K. Johnson, Yeu-Cherng Lu, Kenneth K. Kuo, and Grant A. Risha. 1999. "Regression Rate Behavior of Hybrid Rocket Solid Fuels" *Journal of Propulsion and Power*, Vol. 16, No. 1, January-February 2000.
- Martin J. Chiaverini and Kenneth K. Kuo. 2007. "Fundamentals of Hybrid Rocket Combustion and Propulsion," *American Institute of Aeronautics and Astronautics, Inc., Reston, Virginia*. Pp 207-246.
- Marxman. G.A, and Wooldridge C. E. 1963. "Fundamentals of Hybrid Boundary Layer Combustion," *American Institute of Aeronautics and Astronautics paper*, 1963-5005.
- M. Lazzarin, F. Barato, A. Bettella, and D. Pavarin. 2013. "Computational Fluid Dynamics Simulation of Regression Rate in Hybrid Rockets," *Journal of Propulsion and Power*, Vol. 29, No. 6, November-December 2013, Doi: 10.2514/1.B34910.
- Ordahl D. D. 1964. "Hybrid Propulsion," *Space Aeronautics*, April 1964, 41(4), 108-13.
- Philmon George, and S. Krishnan, Lalitha Ramchandran, P.M. Varkey and M. Raveendran. 1996. *Defense Science Journal*, Vol 46, No 5, November 1996, pp.337-345
- Price C. F, and Smoot L. D. 1965. "Regression Rate Mechanisms of Nonmetalized Hybrid Fuel Systems," *Aerospace Sciences Meeting*, AIAA paper 1965-56.
- Ronald W. Humble, Gary N. Henry and Wiley J. Larson. 1995. "Space Propulsion Analysis and Design," *The McGraw-Hill Companies Publication* pp. 365-440.
- Sabnis, J. S, Gibeling, H. J, and McDonald, H. 1989. "Navier-Stokes Analysis of Solid Propellant Rocket Motor Internal Flows," *Journal of Propulsion and Power*, Vol. 5, No. 6, pp 657-664.
- S. Venugopal, K. K. Rajesh and V. Ramanujachari. 2011. "Hybrid Rocket Technology," *Defense Science Journal*, Vol. 61, No. 3, May 2011, pp. 193-200.
- Venkateswaran Sankaran. 2007. "Computational Fluid Dynamics Modeling of Hybrid Rocket Flowfields," *American Institute of Aeronautics and Astronautics*, pp 323-349.